İSTANBUL TECHNICAL UNIVERSITY ★ EURASIA INSTITUTE OF EARTH SCIENCES

ANALYSIS AND MODELLING OF EARTHQUAKE SURFACE DEFORMATION WITH SAR INTERFEROMETRY: CASE STUDIES FROM TURKEY AND THE WORLD

Ph.D. Thesis by

Ahmet M. AKOĞLU, M.Sc.

Department : **Solid Earth Sciences**

Programme: **Geodynamics**

MARCH 2008

İSTANBUL TECHNICAL UNIVERSITY ★ EURASIA INSTITUTE OF EARTH SCIENCES

ANALYSIS AND MODELLING OF EARTHQUAKE SURFACE DEFORMATION WITH SAR INTERFEROMETRY: CASE STUDIES FROM TURKEY AND THE WORLD

Ph.D. Thesis by
Ahmet M. AKOĞLU, M.Sc.
601012002

Date of submission : 27 February 2008

Date of defence examination: 26 March 2008

Supervisor: Assoc. Prof. Dr. Ziyadin ÇAKIR (İTÜ)

Members of the Examining Committee Prof. Dr. Serdar AKYÜZ (İTÜ)

Prof. Dr. Erhan ALTUNEL (ESOGÜ)

Prof. Dr. Nebiye MUSAOĞLU (İTÜ)

Doç. Dr. Semih ERGİNTAV (TÜBİTAK)

MARCH 2008

İSTANBUL TEKNİK ÜNİVERSİTESİ ★ AVRASYA YER BİLİMLERİ ENSTİTÜSÜ

DEPREM YÜZEY DEFORMASYONLARININ SAR İNTERFEROMETRİSİ İLE ANALİZİ VE MODELLENMESİ: TÜRKİYE'DEN VE DÜNYADAN ÖRNEKLER

DOKTORA TEZİ
Y. Müh. Ahmet M. AKOĞLU
601012002

Tezin Enstitüye Verildiği Tarih : 27 Şubat 2008

Tezin Savunulduğu Tarih : 26 Mart 2008

Tez Danışmanı:	**Assoc. Prof. Dr. Ziyadin ÇAKIR (İTÜ)**
Diğer Jüri Üyeleri	**Prof. Dr. Serdar AKYÜZ (İTÜ)**
	Prof. Dr. Erhan ALTUNEL (ESOGÜ)
	Prof. Dr. Nebiye MUSAOĞLU (İTÜ)
	Doç. Dr. Semih ERGİNTAV (TÜBİTAK)

MART 2008

Acknowledgments

It took longer than I thought. It was harder than I expected. Losing Prof. Aykut Barka (due to a head injury just like another legendary figure Prof. Keiti Aki) in the first semester, probably was the hardest part of them for all. Years later we still suffer from his loss just like his own family. This thesis is dedicated to Prof. Aykut Barka.

I would like to express my sincere thanks to my advisor Dr. Ziyadin Çakır for teaching me InSAR from scratch and sharing his knowledge on active tectonics and Unix since my MSc studies. Prospective students around the world: if you are ambitious and ready to start climbing this mountain be sure that you have got an advisor like him. Otherwise please do not ruin your life.

Dr. Semih Ergintav is my co-advisor. Whether or not his name is on the hard cover of this thesis does not change this fact. I would like to thank him for his never ending scientific and moral support. My gratitude also goes to Prof. Serdar Akyüz who also is a prominent figure in this thesis work and was my initial advisor after Barka.

It is impossible to name everyone to whom I am indebted to. I would like to thank: Dr. Abdullah Karaman for his reference letter which changed my mind in 1999; Professors H. Eyidoğan, A. Okay and N. Görür for giving me the privilege to study at EIES; Prof. O. Tüysüz and the staff of the Institute for their amazing tolerance; the members of the Tübitak EMSI for their incredible hospitality; fellow friends at the faculty and the Institute; past students of Prof. Barka like E. Evren and Ö. Kozacı; and finally the PCLabs crew (particularly Özkan & Murat) for their support and contributions.

I would like to thank Prof. Roland Bürgmann and Dr. Mathieu Ferry for the İsmetpaşa, Dr. Chuck Wicks for the Moroccan earthquakes, and Dr. Ömer Emre and Prof. Ali Pınar for the Orta earthquake studies for their insightful and constructive comments. I also would like to thank the Poly3D developers from Stanford University and IGEOSS for providing us the software and for their support. I am grateful to the Doris and RoiPac developers for sharing their great code with the InSAR community. Most of the figures in this thesis were plotted using the open source GMT software developed by Paul Wessel and Walter Smith. The Doris course held at the METU also increased my understanding of the whole interferometric process for which I would like to thank Dr. Bert Kampes, Dr. Ramon Hanssen and the organizer Dr. Nurettin Kaymakçı. Dr. W.Keydel's SAR lecture and the annual ATAG meetings were also fruitful experiences. I had the opportunity to be supported by the EU-FP6 TR-Access Mobility Project for a brief time frame during my thesis. I also would like to mention European Space Agency for their generosity: InSAR would not be possible without them.

Words are not enough when it comes to the family: I simply would like thank them for their patience throughout all these years.

February 2008 Ahmet M.AKOĞLU

TABLE of CONTENTS

ABBREVIATIONS

1D : One dimensional
3D : Three dimensional
ALOS : Advanced Land Observation Satellite
ASAR : Advanced Synthetic Aperture Radar
CFS : Coulomb Failure Stress
CMT : Centroid Moment Tensor
CSEM : European-Mediterranean Seismological Center
DEM : Digital Elevation Model
DORIS : Delft Object Oriented Radar Interferometric Software
E : East
EAF : East Anatolian Fault
ENVISAT : European Space Agency Environmental Satellite
ERD : Earthquake Research Department of the General Directorate of Disaster Affairs (Afet İşleri Genel Müdürlüğü)
ERI : Earthquake Research Institute, Tokyo
ERS : Earth Resource Satellite
ESA : European Space Agency
ETHZ : Eidgenössische Technische Hochschule Zürich
GFZ : GeoForchungsZentrum Postdam
GPS : Global Positioning System
GUI : Graphical User Interface
HRV : Harvard University
IAG : Instituto Andaluz de Geofisica
IGN : Instituto Geografico Nacional
InSAR : Synthetic Aperture Radar Interferometry or Interferometric Synthetic Aperture Radar
ISC : International Seismological Center
JERS : Japanese Earth Resources Satellite
JPL : Jet Propulsion Laboratory
LOS : Line Of Sight
M : Magnitude or Mainshock
Ms : Magnitude (from surface waves)
Mw : Moment magnitude
Mo : Seismic moment
N : North
NAF : North Anatolian Fault
NASA : National Aeronautic Space Administration, USA
Nm : Newton meter
NOAA : National Oceanographic and Atmospheric Administration, USA
P : Pressure
R : Reidel Shear
RGB : Red Green Blue colour model
RMS : Root Mean Square

ROI_PAC	: Repeat Orbit Interferometry PACkage
S	: South
SAR	: Synthetic Aperture Radar
SED	: Swiss Seismological Service
SLC	: Single Look Complex
SLR	: Side Looking Radar or Satellite Laser Ranging
SNR	: Signal to Noise Ratio
SRTM	: Shuttle Radar Topography Mission
SVD	: Singular Value Decomposition
T	: Tension
TÜBITAK	: Türkiye Bilimsel ve Teknolojik Araştırma Kurumu
USGS	: United States Geological Survey, USA
UTM	: Universal Transverse Mercator
USA	: United States of America
VLBI	: Very Long Baseline Interferometry
W	: West
3D	: Three Dimensional

LIST of TABLES

LIST of FIGURES

LIST of SYMBOLS

$\mathbf{a, b}$: Variables of reverse exponential function
$\mathbf{A}$: Amplitude, fault or rupture area
α : Baseline orientation angle, fault strike
$\mathbf{B}$: Baseline
$\mathbf{B_c}$: Critical baseline
$\mathbf{B_h}$: Horizontal component of baseline
$\mathbf{B_r}$: Frequency bandwidth
$\mathbf{B_v}$: Vertical component of baseline
$\mathbf{B_{II}}$: Parallel component of baseline
$\mathbf{B}_\perp$: Perpendicular component of baseline
β : Angle between equator and nadir track
$\mathbf{c}$: Speed of light
$\mathbf{D}$: Antenna width
$\delta\mathbf{d}$: Elevation change
$\delta\mathbf{R}$: Range difference
$\delta\mathbf{R_a}$: Ground azimuth resolution
$\Delta\sigma_\mathbf{f}$: Coulomb stress change
$\delta\mathbf{R_g}$: Ground range resolution
$\Delta\sigma_\mathbf{n}$: Normal stress change
$\Delta\mathbf{R}$: Scalar range change
$\Delta\tau$: Shear stress change
ϕ : Phase difference
$\mathbf{H}$: Height of radar instrument
$\mathbf{h}$: Height of target
$\mathbf{h_a}$: Altitude of ambiguity
φ : Look angle (near range)
ψ : Look angle (far range)
η : Incidence angle
λ : Wavelength
$\mathbf{I}$: In-Phase
$\mathbf{L}$: Antenna length
$\mathbf{l}$: Fault length
μ' : Shear modulus, effective coefficient of friction
$\mathbf{r}$: Rake
$\mathbf{R}$: Range
$\mathbf{R_n}$: Near range
$\mathbf{R_f}$: Far range
$\mathbf{R_m}$: Mid range
$\mathbf{s}$: Slip
$\hat{\mathbf{s}}$: Unit vector pointing to satellite
$\mathbf{S_w}$: Swath width
$\mathbf{Q}$: Quadrature
θ : Look angle (mid range), fault dip
$\tau_\mathbf{p}$: Pulse duration

$\bar{\mathbf{u}}$: Displacement vector
$\mathbf{V}_s$: Velocity of radar instrument (Satellite or aircraft)
$\mathbf{V}_x$: Velocity of target
$\mathbf{z}$: Fault depth
$\mathbf{w}$: Wave's frequency, fault width

ANALYSIS AND MODELLING OF EARTHQUAKE SURFACE DEFORMATION WITH SAR INTERFEROMETRY: CASE STUDIES FROM TURKEY AND THE WORLD

SUMMARY

Synthetic Aperture Radar Interferometry (InSAR) is a space geodetical technique which was introduced to the active tectonics research about 15 years ago when it was utilized for the first time to study the surface displacement field of the 1992 Landers (California) earthquake. In this period the technique has become popular and widely used in conjunction with conventional seismology and the Global Positioning System (GPS) to investigate several earthquakes that occurred since the launch of the ERS1 satellite by the European Space Agency (ESA) in July 1992. Tectonically active regions like California and Anatolia greatly benefited from this new tool during the operation period of ESA satellites: the 1992 Big Bear and Landers, 1994 Northridge and 1999 Hector Mine earthquakes in California, the 1995 Dinar and 1999 earthquakes of İzmit and Düzce events are investigated using InSAR with the data from these satellites. The 1995 Antofogasta (Chili), 1997 Manyi (Tibet) earthquakes as well as the volcanic activities on Earth like the one at Mount Etna are among the other well known applications of InSAR for earth sciences.

The underlying principles of the InSAR technique can be summarized with two principles: 1) A longer radar antenna which is essential to get a higher resolution is synthesized by using Doppler frequency shifts of a target on the earth surface; and 2) The difference between the phases of two radar images (e.g. one before the earthquake and one after) is calculated in order to get the distance change during the time span of the two acquisitions. The calculated phase differences between the two images are called an interferogram and can simply be described as a high density and sub-cm accurate contour map showing the change in distance between the radar instrument and the earth surface during the period between the acquisition times of the images. The contour interval of this special map depends solely on the wavelength of the radar signal used during the image acquisition which is ~28 mm for C-band radars like ERS1. Every 2π phase change between adjacent pixels in an interferogram is shown with a fringe which is generally plotted as a full RGB cycle (e.g. the region between two blue bands).

The main obstacle for an accurate measurement with this technique is the atmospheric phase delays. Removal of atmospheric artefacts from interferograms to isolate the phase changes resulting from surface deformation is not yet possible. The other limitation of the technique is that the interferograms are one dimensional surface displacement maps which means they only show the line-of-sight (LOS) change between the radar instrument and the earth surface instead of a 3D deformation information (e.g in Cartesian XYZ coordinates) usually provided by the other geodetical techniques, like GPS. After the removal of the phase changes due to topography one should try to derive the possible 3D deformation field due to a tectonic-related surface movement that is being studied from the observed LOS changes and the unit vector. One can use forward modelling techniques or more advanced inversion algorithms to accomplish this essential task.

Forecasting earthquakes is currently beyond us. The driving mechanism behind the earthquakes, the interaction between them and similar earth movements like interseismic creeping are still poorly known and heavily discussed. Therefore, studying all the medium-to-large sized events (M>6) on Earth with the available tools and techniques is the very best we can do for the moment. Analysis of every single event may reveal new clues about the physics of earthquakes, which may be a step forward in the half a millennia-old plate tectonics based scientific exploration of Earth. Moderate-to-large events caused by blind faults usually with no surface rupture on Earth have a key role in this context since they occur more often in a yearly basis than do the major events (M>7). Being able to monitor and investigate these earthquakes without the need to travel to the epicentral area is of paramount importance. With this goal in mind we have applied InSAR to study the coseismic deformations of select earthquakes that occurred between 2000 and 2005 in the Alpine-Himalayan collision belt around the Mediterranean.

The 2000-2002 (Mw 6.0, 6.4) Afyon-Akşehir (Sultandağı) earthquake sequence and the 2005 İzmir-Sığacık earthquakes (Mw 5.4, 5.8, 5.9) are presented in the form of short case studies (Chapter 1). Due to phase delays caused by the atmosphere, we can not manage to isolate the deformation signal in the Afyon case. In the İzmir case, even though the most of the deformation is offshore, we have detected up to 4 east-west trending fringes (i.e. 113 mm) on the northern coast of the Sığacık Bay which is only a small fraction of a much larger deformation field that is spread under water. Even though most of the deformation occurred offshore, our InSAR analysis supports the seismological findings and (on the contrary to some previous claims) shows that the rupture did not occur on land.

The June 6, 2000 Orta (Çankırı) earthquake (Mw 6.0) is studied with InSAR in full detail (Chapter 2). From the analysis of two separate interferograms and the subsequent elastic dislocation modelling using a non-linear minimization procedure based on simulating annealing algorithm, we inferred that the earthquake occurred on a N-S striking, eastward dipping listric fault with a left-lateral strike slip component at a high angle to the North Anatolian fault. The modelling procedure that is guided by the available field reports of the earthquake shows that the coseismic slip occurs nearly solely on the lower part of the listric fault at 4-6 km depths. Confirming the field observations, our modelled listric fault reaches to the surface along the surface trace of the Dodurga fault which, we think, is a result of a restraining bend along the North Anatolian fault. The left-lateral kinematics of this fault is also consistent with the present stress regime that favors the right-lateral North Anatolian fault.

Two North African earthquakes, the May 26, 1994 (Mw 6.0) and February 24, 2004 (Mw 6.4) events that affected the Al Hoceima region of northern Morocco are also studied with the available InSAR data collected from both the ascending and descending orbits (Chapter 3). Being the strongest earthquakes ever to be recorded instrumentally in the region, the analysis of the earthquakes has an important role in the tectonics of the region. We modelled the manually unwrapped fringes derived from the processed interferograms by using slip inversions on triangular fault patches instead of commonly used rectangular ones which enabled us to use non-planar more realistic fault models for the earthquakes. Modelling suggests that the two events occurred on blind conjugate strike slip faults: the 1994 event is associated with a N23° trending left-lateral fault and the 2004 event with a N45°W trending right-lateral fault. It is worthwhile to mention that, especially for the 2004 event, InSAR contradicts the previous findings based on seismic waveform analysis and aftershocks distribution which suggest a left-lateral fault plane instead of a right-lateral one. The study of these two moderate events reveals the fragmentation of the Rif Mountain throughout a complex network of conjugate blind faults, consistent with the transpression tectonics along the plate boundary in North Africa. Although the two earthquakes took place in the Rif thrust-and-fold belt, the late Quaternary deformation indicates E-W extension in agreement with the NW-SE and NE-SW trending conjugate strike-slip faulting.

Being able to monitor aseismic creep movements is one of the significant aspects of InSAR for active tectonics studies. Taking advantage of the spatial and temporal coverage of ERS1 and ERS2 satellites since 1992, we were able to investigate and present our findings about the interseismic creep at İsmetpaşa as our final InSAR case study (Chapter 4). The creep was first spotted by Ambraseys 30 years ago on a brick wall built on the North Anatolian Fault. InSAR results show the extent of the creep for the first time: the creeping starts at the western termination of the 1943 earthquake rupture and continue about 70 km to the west. The creep velocity reaches its maximum value of 11±3 mm/year at the middle of the creeping section. This value is about 8±3 mm/year near İsmetpaşa where the brick wall is located and is consistent with the previous measurements. A combined modelling of InSAR data with GPS suggests that the creep occurs most probably at the uppermost part (0-7km) of the seismogenic crust. The exponential decrease rate of creep in time postulates that the aseismic movement started following the 1944 Bolu-Gerede earthquake.

These three separate applications of InSAR with the addition of the short case on İzmir-Sığacık earthquake once again prove that InSAR is an extremely useful and important tool for active tectonics research. It enables the monitoring of moderate-to-large events and phenomena like the aseismic creep which is not possible without a dedicated dense seismic network nearby. Especially the Al-Hoceima study shows us that in cases where the surface morphology is not clearly defined and surface ruptures are absent, InSAR analysis from data collected from both orbits is indispensable even the aftershocks are aligned in a certain direction. However, as in the Orta-Çankırı case, InSAR alone may not be sufficient for the study of an earthquake; field observations and additional measurements and evidences should not be neglected in the modelling step.

Apart from InSAR, we have investigated the triggering of events in the Karlıova triple junction since 1866 using the Coulomb failure stress approach (Chapter 6). Out of ten earthquakes that took place in the region since the 1866, six can be explained with static stress transfer. We cannot explain the 2003 Bingöl, the first event in Varto in 1966, and the smaller seismic activity around Karlıova in 2005 with Coulomb. The effect of time dependent processes like viscoelastic relaxation may provide a plausible explanation to these events.

Another primary goal is to assess the hazard at the Yedisu Seismic Gap by calculating the total stress change that has accumulated on it since 1866, including the annual loading due to the plate motions. We calculated that the total accumulated stress change along the gap reaches its maximum values at the edges and is over 5 bars. After 141 years, the average stress along the center of the gap is near 2 bars (excluding the tectonic loading). The maximum possible event size along the gap depends on its length which may be shorter than previously thought if the 1967 Pülümür-Kiğı event broke part of the seismic gap as suggested by Ambraseys (1998). Using fault scaling laws based on statistical observations (Well and Coppersmith, 1994) we assume a minimum length of 50 km and a moment magnitude (Mw) of 7.06 for a single segment rupture along the gap. If the 1967 Pülümür event did not occurred on the Yedisu fault segment, than the length will increase to 70, and even to 80 km (Akyüz, personal communication), in which case the magnitude will climb to 7.23-7.29, creating shaking 1.5-1.7 times more greater in amplitude.

DEPREM YÜZEY DEFORMASYONLARININ SAR İNTERFEROMETRİSİ İLE ANALİZİ VE MODELLENMESİ: TÜRKİYE'DEN VE DÜNYADAN ÖRNEKLER

ÖZET

Yapay (sentetik) Açıklık Radar İnterferometrisi (InSAR) ilk defa 15 yıl önce Landers depreminin oluşturduğu yüzey deformasyonlarının incelenmesi için kullanılmaya başlanarak aktif tektonik araştırmacılarının hizmetine sunulmuş olan uzay bazlı jeodetik bir yöntemdir. Avrupa Uzay Ajansı'na ait ERS1 uydusunun fırlatıldığı Temmuz 1992'den günümüze kadar geçen süre zarfında bu teknik bir çok farklı depremin incelenmesi için sismoloji ve Küresel Konumlama Sistemi (GPS) ile birlikte kullanılarak yaygınlaşmış ve aynı zamanda da olgunlaşmıştır. Kaliforniya ve Anadolu gibi tektonik olarak aktif bölgeler bu teknikten azami ölçüde istifade etmiştir: Kaliforniya'da 1992 Big Bear ve Landers, 1994 Northridge ve 1999 Hector Mine depremleri; Anadolu'da ise 1995 Dinar, 1999 İzmit ve Düzce depremleri InSAR kullanılarak incelenmiş en önemli tektonik olaylardır. Bunların yanısıra InSAR, Antofogasta (Şili), 1997 Manyi (Tibet) gibi pek çok depremin yanısıra dünyanın farklı bölgelerinde, erişimi zor veya sık sismik ağ kurulmamış tektonik yörelerinde kullanım alanı bulmuştur. Depremler dışında InSAR buzul çalışmalarında ve Etna Dağı gibi volkanik aktivitelerde de yer bilimcilere yeni bir bakış açısı sunmuştur.

InSAR tekniği şu iki ana prensip ile özetlenebilir: 1) radar görüntüsünün çözünürlüğü anten uzunluğu ile doğru orantılı olduğu ve bu uzay gibi ortamlarda mümkün ve gerçekçi olmadığı için yeryüzündeki bir hedefin Doppler frekans ötelenmeleri kullanılarak yapay bir anten sentezlenir; 2) (aktif tektonik için biri deprem öncesinde diğeri depremden hemen sonra alınmış) iki radar görüntüsü birbirlerinden çıkarılarak faz farkları hesaplanır; bu faz farkı iki görüntü tarihi arasında radar ile yeryüzü arasındaki mesafe değişimini verecektir. Faz farklarını içeren nihai imaja interferogram denir ki buna kabaca, her pikseli iki görüntünün alındığı tarihler arasında radar platformu ile yeryüzü arasında cereyan etmiş olan mesafe değişimlerini içeren bir kontur haritası da denebilir. Bu özel haritanın kontur aralığı kullanılan radar sinyalinin dalga boyuna bağlıdır: bu değer ERS1 gibi C-bantı radar uyduları ile alınan görüntülerle üretilen interferogramlar için ~28 mm'dir. İnterferogramda komşu pikseller arasındaki her 2π'lik

faz değişimine saçak (fringe) denir ve genellikle bu değişim tam bir RGB renk döngüsü (örneğin mavi ile renklendirilmiş bir kuşaktan bir sonraki mavi renkli kuşağa) ile ifade edilerek gösterilmeye çalışılır.

InSAR tekniğinin avantajları ve sunduğu kolaylıkların yanısıra bazı dezavantajları mevcuttur. Bunlardan birincisi ve en önemlisi, henüz düzeltilmesi mümkün olmayan, radar sinyalinde meydana gelen atmosfer kaynaklı (çoğunlukla su buharı) faz gecikmeleridir. İki görüntü alımı esnasındaki atmosferik koşullardaki değişimler nedeniyle oluşan bu sinyaller deformasyon nedeniyle meydana gelen sinyallerle karıştırılabilir veya onları ortadan kaldırabilir. Bu yöntemin ikinci dezavantajı ise GPS ve diğer bazı jeodezik yöntemlerin aksine ölçümlerin tek boyutlu olmasıdır. Başka bir deyişle, interferogramlar sadece radar platformu ile yeryüzü arasında radar bakış açısındaki doğrultuda yaşanan mesafe değişimlerini içeren tek boyutlu haritalardır. Bu nedenle üç boyutlu bir deformasyon haritası elde edebilmek ve nasıl bir tektonik kaynağın buna sebep olduğunu araştırabilmek için InSAR prosesinden sonra birim vektörleri de kullanarak bir modelleme çalışması yürütmek gerekir.

Depremlerin önceden tahmini ne yazık ki günümüzde mümkün değildir. Depremlerin arkasındaki mekanizmanın detayları, depremlerin birbiri ile ilişkileri ve asismik kayma gibi yeryüzü hareketleri bugün bile tam anlaşılamamış olup bilim çevrelerinde tartışmalar devam etmektedir. Bu nedenle, elimizdeki her imkan ve teknik ile yeryüzünde cereyan eden olayları araştırmaya devam etmek yapılabileceklerin en başında gelmektedir. Her yeni doğa olayının her yeni depremin incelenmesi ortaya daha önceden bilinmeyen veya farkedilmemiş olan yeni olguların konmasını sağlamaktadır. Her yeni veri, levha tektoniği fikrinin ortaya atılması ve Atlantik tabanındaki manyetik şeritlerin farkedilmesinden bu yana geçen yarım yüzyıllık süre içinde insanoğlunun gezegenimiz hakkında biriktirdiği bilgi havuzuna yeni bir katkıdır. Bu minvalde büyüklüğü altı ve altıdan büyük, yüzeye ulaşmayan ve yüzeyde kırık oluşturmayan kör faylarda meydana gelen depremler, yedi ve üzeri büyüklükteki depremlere gore çok daha sık şekilde cereyan ettiklerinden büyük önem taşımaktadırlar. Deprem bölgesine gitmeye gerek dahi kalmadan bu depremlerin InSAR ile incelenebilmesinin kıymeti bu nedenle oldukça yüksektir.

Bu tezde, açıklanan bu nedenlerin ışığında, 2000-2005 yılları arasında Türkiye ve onu çevreleyen Avrasya ve Afrika plakalarında meydana gelmiş bazı depremler seçilmiş ve bunların yeryüzünde meydana getirdiği kosismik deformasyonlar InSAR ile incelenmiştir. Bu depremlerin ortak özellikleri ise hiç birinin yüzey kırığı oluşturmamış olması ve bu nedenle mekanizmaları ve yerleri hakkında kesin ve detay bilgilerin mevcut olmamasıdır.

Özet şeklinde sunulan 2000-2002 (Mw 6.0 ve 6.4) Afyon-Akşehir (Sultandağı) depremleri için 6 adet interferogram hesaplanmış olup, bunlardan atmosferden kaynaklanan faz gecikmelerinin temizlenememesi ve ERS2 uydusunda yaşanan jiroskop arızaları nedeni ile InSAR kullanılarak faydalı herhangi bir sonuç elde edilememiştir (Bölüm 1). Kısa bir şekilde sunulan İzmir-Sığacık depremleri (Mw 5.4, 5.8 ve 5.9) için ise 2 adet interferogram hesaplanmış olup, deprem aktivitesi Sığacık Körfezi içinde denizde cereyan etmiş olmasına rağmen körfezin kuzey kıyısında dört frinçlik (saçak) yüzey deformasyonu gözlenmiştir. Her ne kadar interferogramları modelleme için kullanmak mümkün olmasa ve deformasyonun çoğu denizel ortamda gerçekleştiğinden kaydedilememiş olsa da verinin sismolojiden elde edilen verileri desteklediği, ana aktivitenin körfezdeki KD-GB uzanımlı kolda yaşandığı ve depremi müteakiben bilim adamlarınca hararetle tartışılan karada kırılmanın gerçekleşmediğini göstermektedir.

6 Haziran 2000, Orta (Çankırı) depreminin (Mw 6.0) InSAR ile analizi ve bunu takip eden modelleme çalışması sonucunda depremin doğuya eğimli, kuzey-güney uzanımlı, sol yanal bileşene sahip (oblik) kör bir listrik fayda meydana geldiği anlaşılmıştır (Bölüm 2). Yapılan arazi gözlemlerini kaale alarak yürütülen modelleme çalışması kosismik kaymanın tamamına yakın kısmının listrik fayın 4 ila 6 km'leri arasında yaşandığını göstermektedir. Deprem sonrası araştırmacılar tarafından tamamlanan arazi gözlem raporlarında Dodurga fayı depremi üreten fay olarak tanımlanmış olup nihai listrik modelimiz de bu fay hizasında yüzeye erişmektedir. Fayın sahip olduğu sol yanal bileşen, sağ yanal Kuzey Anadolu fayını destekleyen günümüz stres rejimiyle uyum içindedir.

Fas'ın El Hüseyma şehrinde meydana gelen 26 Mayıs 1994 (Mw 6.0) ve 24 Şubat 2004 (Mw 6.4) Kuzey Afrika depremleri de InSAR kullanılarak çalışılmıştır (Bölüm 3). Her iki uydu yörüngesinden de veri temin edilebilen bu çalışma, her iki deprem aletsel dönemde bölgede kaydedilen en büyük olaylar olduğu için bölge tektoniği için önem taşımaktadır. El ile sayısallaştırılan deprem frinçlerinin kullanıldığı modelleme aşamasında, dikdörtgen dislokasyonlar tanımlandığında özellikle kıvrımlı ve segmentli fay modelleri kullanımında karşılaşılabilecek boşlukların ve üst üste binmelerin önüne geçilmesini ve daha gerçekçi fay modelleri üretilebilmesini sağlayan üçgensel elemanlar kullanılmıştır. Çalışmanın sonucunda elde ettiğimiz nihai modeller bize iki depremin eşlenik iki fay üzerinde meydana geldiğini göstermektedir: 1994 depremi K23°D doğrultulu sol yanal, 2004 depremi ise K45°B doğrultulu bir sağ yanal fay üzerinde oluşmuştur. Çalışmada vurgulanması gereken en önemli detay 2004 depremi için InSAR'dan elde edilen sonucun bu deprem için sol yanal bir fay öngören sismik dalga formu analizi, artçı şok dağılımları gibi sismolojik kaynaklı çalışmaların aksine fayın sağ yanal karakterli olduğunu ortaya koymuş olmasıdır. Bu iki depremin InSAR analizi ve son zamanlarda oluşan doğrultu atımlı faylarla ilişkili deprem aktivitesi göstermektedir ki Kuzey Afrika-Avrasya levha sınırındaki Rif bölgesi, doğusunda ve batısında bindirme faylarla ilişkili depremlerin etkisi altındaki kuzey Cezayir ve Kadiz bölgelerinden sismotektonik açıdan farklılık göstermektedir. El Hüseyma ve civarında topoğrafyadaki hakim morfotektonik yapıların halen sıkışma rejimi ürünleri olması bu bölgedeki doğrultu atımlı tektonik rejimin yakın zamanda başladığı fikrini desteklemektedir.

Asismik kayma-krip hareketlerini gözlemleme olanağı tanıması InSAR'ın en önemli avantajlarından birisidir. ERS1 ve ERS2 uydularının 1992'den beri meydana getirmiş olduğu geniş arşivden istifade edilerek KAF üzerinde İsmetpaşa'da gözlenen intersismik krip araştırılmıştır (Bölüm 4). İlk olarak 30 sene once Ambraseys tarafından KAF üzerindeki bir duvarda gözlemlenen kaymanın alansal olarak kapsamı ilk defa InSAR tarafından tanımlanabilmiştir: krip 1943 depremi kırığının batı sınırından başlamakta ve batıya 70 kilometre ilerleyerek 1944 kırığının doğu ucuyla örtüşmektedir. Kayma hızı segmentin yaklaşık orta kesimlerinde maksimum değeri olan 11±3 mm/yıl'a ulaşmaktadır. Bu değer İsmetpaşa yakınlarında duvarın bulunduğu bölgede 8±3 mm/yıl'dır, ki bu daha önceki ölçümlerle uyumludur. InSAR verilerinin GPS ile birlikte modellenmesi sonucu kripin kabuğun üst kısmında (0-7 km) yaşandığı izlenimi oluşmaktadır. Kripin zaman içindeki üstel azalımına bakılarak asismik hareketin 1944 Bolu-Gerede depremi ile başladığı söylenebilir.

Tezin son bölümünde InSAR'a ek olarak, aktif tektonik çalışmalarında kullanılan bir diğer teknik olan Coulomb Gerilme Modellemelerine yer verilmiştir (Bölüm 5). 1866'dan beri Karlıova üçlü birleşimi ve çevresinde meydana gelen 10 olaydan 6'sı Coulomb gerilme değişimleri yaklaşımı ile açıklanabilmektedir. 2003 Bingöl depremi, 1966'daki ilk Varto depremi ve 2005'de Karlıova 1949 kırığı civarında meydana gelen sismik aktivite Coulomb ile açıklanamamaktadır. Viskoelastik etkiler gibi zamana bağlı proseslerin hesaplarda kaale alınması bu depremleri de açıklayabilmemizi sağlayabilir. Coulomb çalışmamızdaki bir diğer öncelikli hedefimiz Yedisu sismik boşluğundaki riski üzerinde biriken gerilme değişimini hesaplayarak değerlendirmektir. Tanyeri ile Elmalı arasında uzanan Yedisu sismik boşluğu boyunca, 1866'dan beri meydana gelen depremlerce biriken toplam gerilme değişimi boşluğun uç kısımlarında 5 bar'ın üzerinde değerlere erişmektedir. Boşluğu temsil eden model gridimizin orta kesimleri boyunca, 141 yıl sonunda (tektonik yükleme hariç) biriken ortalama gerilme yaklaşık 2 bar'dır. Yedisu'da meydana gelebilecek depremin büyüklüğü boşluk boyunca KAF'ın 1784'den beri kırılmamış olduğu düşünülen segmentlerinin uzunluğu ile ilişkilidir: 1967 Pülümür-Kiğı depremi Yedisu'daki segment üzerinde meydana geldi ise (Ambraseys, 1988) sismik boşluk daha kısa olabilir. Bu olasılık göz önüne alınarak, istatistiksel gözlemlerden türetilmiş fay formülleri kullanılarak (Wells and Coppersmith, 1994) tekil bir kırılma için 50 km minimum uzunluk ve buna mükabil (Mw) 7.06 büyüklüğünde bir deprem beklenebileceği varsayılmıştır. Şayet 1967 Pülümür depremi Yedisu sismik boşluğu üzerinde meydana gelmedi ise ise bu uzunluk 70 kilometreye ve hatta 80 km'ye (Akyüz, kişisel görüşme) ve beklenebilecek depremin büyüklüğü ise (Mw) 7.23'e veya 7.29'a çıkabilir ki bu 1.5 veya 1.7 kat daha fazla yer sarsıntısına neden olacaktır.

Chapter 1

Introduction

1.1 Outline of the Thesis

Development and deployment of space geodetical techniques coupled with the achievements in computing and technology in the last decades paved the way for tremendous contributions towards the understanding of the Earth. 80 years after Reid applied the very first geodetical methods to observe displacements on earth due to the 1906 California earthquake, space-based techniques like Very Long Baseline Interferometry (VLBI), Satellite Laser Ranging (SLR), Global Positioning System (GPS) and finally Synthetic Aperture Radar Interferometry (INSAR) have started providing numerous clues on several topics within the framework provided by the plate tectonics theory such as the nature of crustal strain accumulation, behaviour of the faults, how earthquakes release the strain as well as the processes like the aseismic creep which otherwise cannot be measured with conventional seismology. Among those techniques mentioned, just like GPS, InSAR became instantly popular due to its obvious advantages like lower operation costs, high spatial coverage, competitive precision and a useful observation cadence.

Forecasting earthquakes is currently beyond us (Zebker, 2000). The driving mechanism behind the earthquakes, the interaction between them and similar earth movements like interseismic creeping are still poorly known and heavily discussed. The very best we can do at the moment is to study every possible event on earth which will eventually increase our knowledge and let us pursue the goal of knowing our planet and its dynamics better.

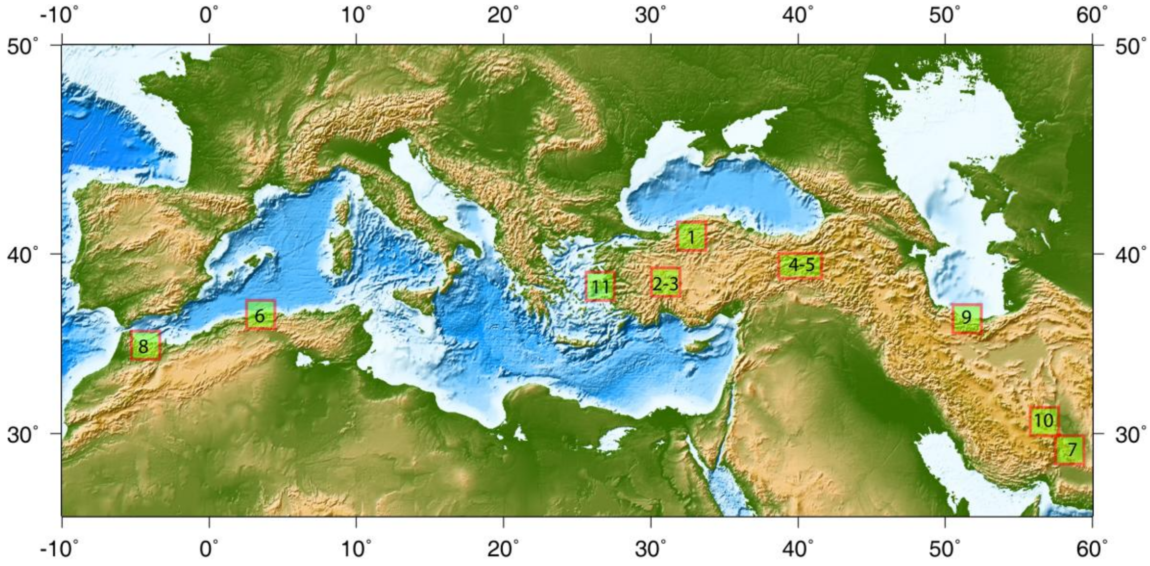

Figure 1.1: Medium-to-large (M>6) earthquakes in the Alpine-Himalayan collision belt between 2000 and 2005 that we obtained InSAR data for. Numbers denote the order used in Table 1.1

Medium-to-large sized earthquakes (M>6) that occur along blind faults which do not produce a visible rupture on earth surface are indeed important for the tectonics of a region since they occur more frequently. The Table 1.1 lists some of the earthquakes that occurred between 2000 and 2005 in Turkey and the surrounding tectonic regions without rupturing the surface. Studying these events will indeed improve our knowledge of local and global tectonics. The discussions on the dynamics of intraplate blocks in Anatolia, the boundary of Eurasia with the African plate in the Mediterranean will indeed greatly benefit from the analysis of medium-to-large events. One of the greatest advantages of InSAR is its capability to provide information to study the locations and the mechanisms of earthquakes that occur along blind faults without rupturing the earth surface. The application of InSAR is of paramount importance especially in places where the local seismic network is not dense enough.

Due to aforementioned reasons throughout this thesis work the InSAR technique is applied to select earthquakes in Anatolia as well as in Eurasia and Africa that occurred between 2000 and 2005 after the well known İzmit and Düzce earthquakes of 1999.

Table 1.1: Events for which we obtained and processed InSAR data. Only the event with bold typefaces are studied and presented in this thesis. The locations of these events are given in Figure 1.1.

	Date	*Event*	*Magnitude*	*Is InSAR successful?*
1	06/06/2000	**Orta – Çankırı**	6.0	✓
2	15/12/2000	**Akşehir (Sultandağı)-Afyon**	6.0	✗
3	03/02/2002	**Akşehir (Sultandağı)-Afyon**	6.4	✗
4	03/02/2003	Pülümür-Tunceli	6.1	✗
5	01/05/2003	Sudüğünü-Bingöl	6.4	✗
6	21/05/2003	Zemmouri-Algeria	6.8	✓
7	26/12/2003	Bam-Iran	6.6	✓
8	24/02/2004	**Al Hoceima-Morocco**	6.5	✓
9	28/05/2004	Firüzabad (Baladeh)-Iran	6.2	✗
10	22/02/2005	Zarand-Iran	6.4	✓
11	17/10/2005	**Sığacık-İzmir**	5.4/5.8/5.9	✓ (partly)

Among these events listed Orta earthquake will be presented in Chapter 2, Al Hoceima earthquake in Chapter 3. Sultandağı and Sığacık events will be discussed in this chapter as short case studies. In addition to these coseismic events, the interseismic creeping phenomenon along the İsmetpaşa section of the North Anatolian Fault (NAF) is investigated with InSAR and is presented in Chapter 4.

None of the earthquakes listed in Table 1.1 produced surface ruptures and most of them occurred along regions where the local seismic network is rather sparse. Even though temporary seismic stations were setup immediately after the main shock, the aftershock sequences may not provide a clue about the causative fault plane as observed in the Al Hoceima case.

In addition to applying InSAR to these select earthquakes in Turkey and Eurasia, we focussed on the Yedisu Seismic Gap near Karlıova Triple Junction. It is one of the two seismic gaps along the NAF that did not rupture in the past century, the other being the one under the Sea of Marmara that is expected to be ruptured in the near feature (Barka, 1999; Parsons *et al.*, 2000; Hubert-Ferrari *et al.*, 2000). Coulomb technique is used in Chapter 5 to assess the stress changes along the Yedisu area since the 1866 earthquake of Bingöl and the possibility of an earthquake along this gap is investigated. We tried to complement the Coulomb study with the InSAR analysis of Pülümür and Bingöl earthquakes of 2003, however due to the ERS2's gyroscope related problems we could not achieve this goal.

1.2 Materials and Methods

We used InSAR and Coulomb stress modelling techniques in this study. Because they are now well known and the technical details about them are thoroughly outlined and discussed in previous studies in the last 20 years (e.g. example literature for InSAR: Massonnet and Feigl, 1998; Bürgmann *et al.*, 2000; Rosen *et al.*, 2000; Hanssen, 2001; Akoğlu, 2001; Çakır, 2003), in this chapter only a brief summary of background information about these techniques with some of the key aspects of InSAR encountered during our processing is presented.

1.2.1 InSAR Background

The radar sensors are being used to image the Earth surface since the Second World War. The advancements in the radar imaging technique possibly changed the course of the war with enabling the bombing of German cities at night where it was hard for the pilots to locate the cities during blackouts.

The natural resolution of a side-looking radar on a moving platform is related directly with the antenna size; the longer the antenna the better the resolution. For example for a C-band (λ = 5.7 cm) radar platform flying ~850 km above the ground with its 10-m long antenna, the typical value of the azimuth resolution that can be achieved is about 4.8 km. This resolution is rather low to monitor earth surface changes and thus must be improved. Building a very long antenna on a spaceborne radar platform is of course not practical, if not, impossible. For example, the antenna length required to achieve about 5-m resolution is over 10 km.

The idea of overcoming the limitation of radar antenna size by synthesising a larger antenna using Doppler frequency shifts returning from points on the ground is attributed to Carl Wiley[1] who developed the first SAR design in 1951 and managed to build an operational SAR a year later (Wiley, 1985). Using these frequency variations objects separated with a distance more than the half-length of the physical antenna can be resolved on the ground; e.g. a resolution of 5 meters in azimuth can be achieved using a 10 meter SAR antenna (Bamler, 2000). This technique does not improve the range resolution which still depends on the radar pulse duration.

Interferometric synthetic aperture radar (InSAR) dates back to 1960s where the interferometry principle, long used in radio astronomy, is first applied over places like the Darien province of Panama (MacDonald, 1969). Then it was used for the exploration of Venus where radar mapping is essential due to the dense cloud cover in the planet's atmosphere. Afterwards it was applied to the moon by Zisk (1972). Graham (1974) was the first to use it for Earth-based topographic mapping. The first application of InSAR to measure surface deformation was by Gabriel *et al.* (1989). Following the launch of ERS-1 satellite in July 1991 the Landers earthquake became the first event to be analyzed with synthetic aperture radar interferometry (Massonnet *et al.*, 1993). Since then the technique has matured completely and has been applied to various earthquakes around the world when suitable data pairs were available. It is now an essential tool for studying crustal deformation and used in conjunction with GPS.

---

[1] At the time Carl Wiley (1918-1985) was an aeronautical engineer working for the Goodyear Aircraft Company (now part of Lockheed Martin). It is interesting to note that in 1951 he also published an article about sailing in space using solar radiation pressure in a science-fiction magazine under a pseudo name of *Russell Saunders* (Love, 1985).

SAR Interferometry can simply be defined as the comparison of time delays (phases) of radar echoes between two SAR images taken on different times (e.g. one before the earthquake and one after). A difference in phase means that the distance between the satellite and the imaged area (earth surface) has changed during the time period between the two image acquisitions. This difference is then displayed as an interferogram which can simply be described as a contour map showing the change in distance between the radar instrument and the Earth surface. The contour interval of this special map depends on the wavelength of the radar signal used during the acquisition. For example, it is ~28 mm for C-band radars (e.g. ERS, Envisat) and ~117 mm for L-band radars (e.g. JERS, ALOS). Every 2π phase change between adjacent pixels in an interferogram is shown with a *fringe* which is generally plotted as a full RGB cycle. However, in order to recover the correct distance change this wrapped phase values of an initial interferogram must be “unwrapped” by adding multiples of 2π. This process is a major part of the InSAR process and is especially important in the modelling step that follows.

Although interferograms are of unrivalled high density and sub-cm accuracy, they are in fact only one dimensional surface displacement maps. Besides, due to the polar orbiting InSAR satellites the studied region on Earth can be imaged from two different look angles which lead to differences in the observed interferograms. This is explained in Figure 1.2 below.

A generalized flowchart showing the steps of an InSAR process is given in Figure 1.3. We used Roi_Pac and Doris[2] software packages to process the radar pairs throughout the thesis. Both of the software packages are freely available and their source codes are open. Although their learning curves are steeper than GUI based commercial InSAR processors, it is important to note that they outpace them in configurability and extendibility.

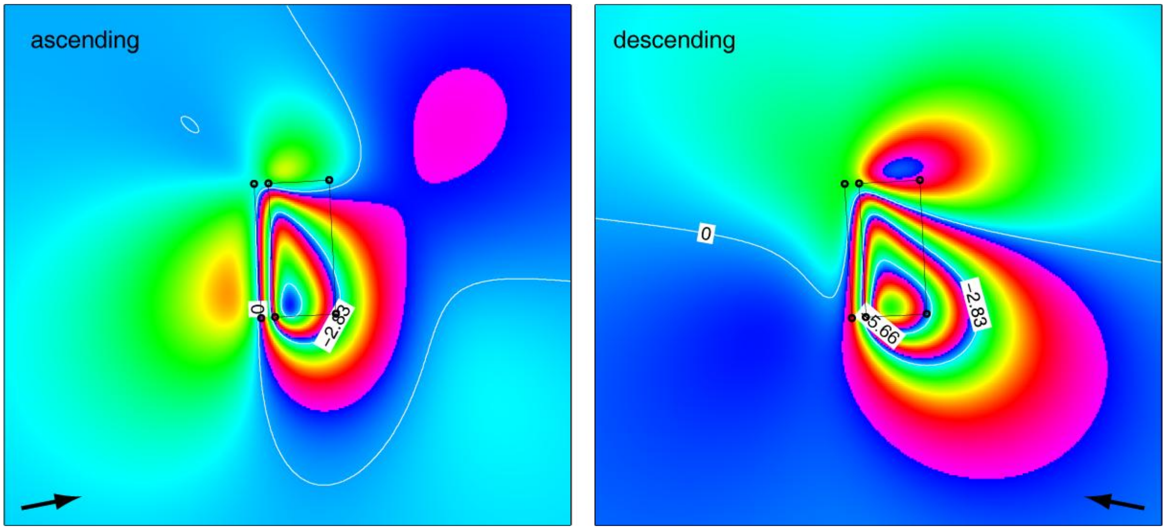

Figure 1.2: Since InSAR measures surface changes in 1-D (i.e. between surface and the radar) the surface deformation due to a normal fault on the ground will be recorded differently from ascending and descending orbits. The black arrows show the corresponding look-angles of the two polar orbits. The model fault used in the figure trends approximately N-S and has a dip of 55° to the East. The observed deformation is Mw 6.3.

---

[2] Doris can only process Single-Look Complex (SLC) data.

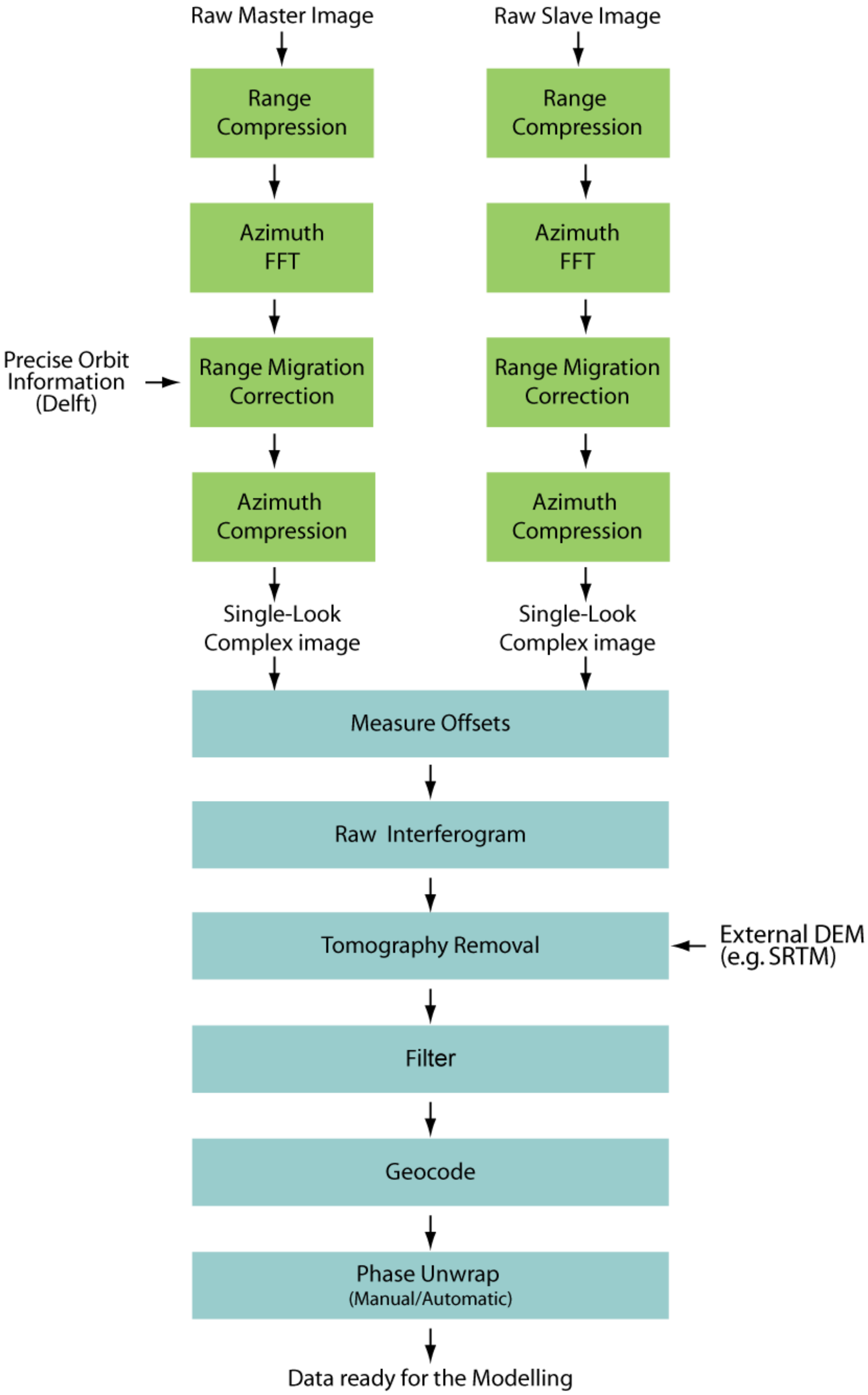

Figure 1.3: InSAR processing flowchart

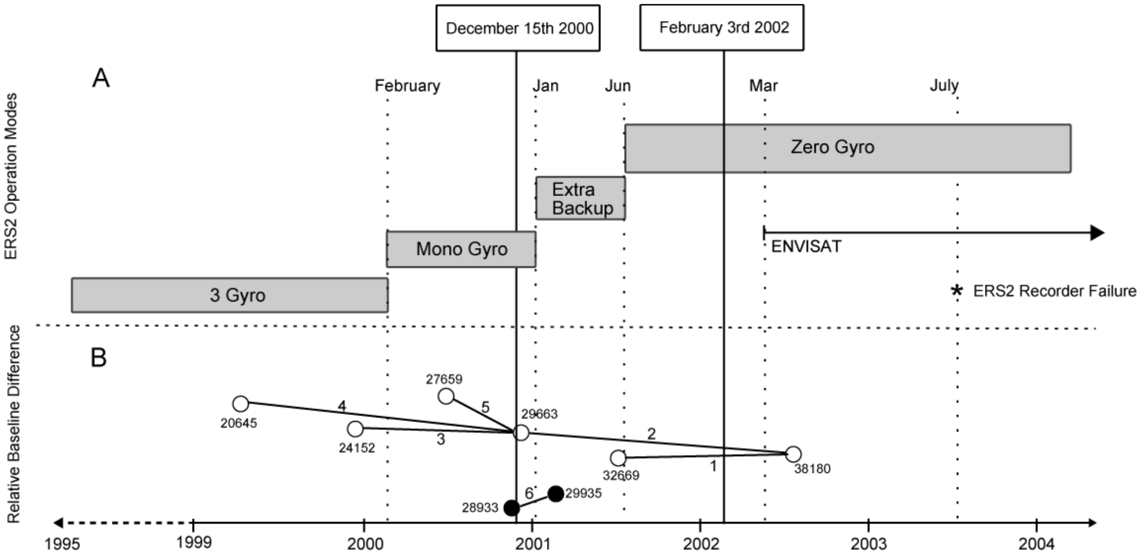

Figure 1.4: (A) The operation modes of ERS2 satellite since its launch. (B) The SAR data ordered for the 2000-2002 Afyon-Akşehir (Sultandağı) earthquakes. The empty circles represent the orbits from Track 250 and the black coloured circles represent images from Track 21. The numbers above the lines between the circles represent the calculated interferograms given in Table 1.2.

Data selection is a critical step for InSAR. Even though current SAR satellites provide global coverage, often it's not possible to study an earthquake due to the lack of available data covering the region before and after the event date. Another important criterion (which is especially important when ordering and processing ERS2 SAR data) is the Doppler centroid ambiguity. Due to the gyroscope failure onboard the satellite after February 2000, one should take care when ordering data. It is suggested to check the Doppler centroid ambiguity value from the available catalogues before ordering. Sometimes user feedback will be necessary during the data process. The operation modes of the ERS2 satellite are summarized in Figure 1.4. A possible impact of a bad Doppler centroid choice is shown in Figure 1.5.

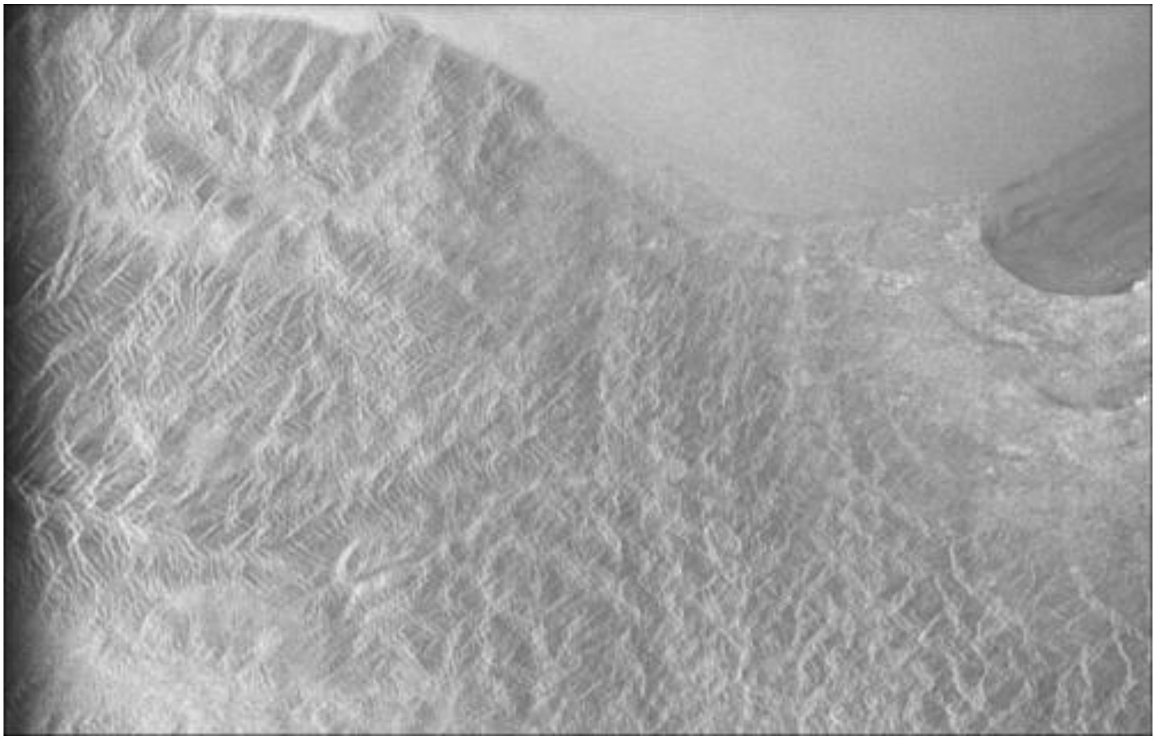

Figure 1.5: Impact of a bad Doppler centroid choice: a second “ghost” coast line appears in this SAR image from northern Algeria.

Phase difference observed in an interferogram can be due to several different phenomena. Apart from earthquake related phase difference, topography, atmospheric events, orbital errors, inconsistencies in the geodetic model of Earth, and data processing based problems (e.g. errors in the leader file) can cause signal delay. Thanks to the freely available Shuttle Radar Topography Mission (SRTM) data it is now much easier to remove the effect of topography from an interferogram (if the data is carefully selected with an height ambiguity value lower than the resolution of the input DEM). Orbital errors can also be minimised using precise orbits. However, the contribution of atmosphere and decorrelation due to agriculture is still not easy to handle in conventional InSAR. For example temporal and spatial fluctuations of water vapour in the atmosphere can obscure and delay signals since its refractive index at radio frequencies is 20 times greater than at optical wavelengths (Onn, 2006).

1.2.2 Coulomb Stress Modelling

When an earthquake happens on a fault it changes the state of stress on the neighbouring faults; it can trigger a nearby fault to rupture early or can postpone a possible rupture by decreasing the overall stress over the candidate fault(s). Coulomb failure criterion is used as a basis to define the interaction between earthquake triggering and stress perturbations since the beginning of the 1980s (Das and Scholz, 1981; Stein and Lisowski, 1983; King *et al.*, 1994; Nalbant, 1996). Excellent review of the studies till today can be found in Harris (1998) and Steacy *et al.* (2005).

Elastic dislocations on rectangular planes in a homogeneous and isotropic half-space, (Okada, 1985) are used to calculate the stress changes due to an earthquake on the nearby faults. When the fault parameters (strike, dip, rake and slip) and the elastic properties of the regional crustal structure are known, the spatial distribution of the stress tensor can be retrieved. Resolving this tensor on to a given plane at a given depth it is then possible to calculate the Coulomb stress distribution. Stress tensors are either resolved onto optimally oriented planes or previously known faults (if the active faults in the region are known in detail).

The change in Coulomb stress is defined by equation 1.1:

$$\Delta CFS = \Delta \tau + \mu' \Delta \sigma_n \tag{1.1}$$

$\Delta\tau$ is the change in shear stress (positive in the direction of the fault slip), $\Delta\sigma$ is the change of normal stress (positive in unclamping-extension of the fault), and the μ' is the apparent coefficient of friction on the fault. A positive Coulomb stress change is expected to promote failure on the receiver faults. Pore pressure also plays a significant role in the determination of the Coulomb failure stress. It is assumed to be represented by the apparent coefficient of friction (μ') term in the above equation (Simpson and Reasenberg, 1994) and is assumed to be constant in most of the studies to minimize the uncertainty (King *et al.*, 1994).

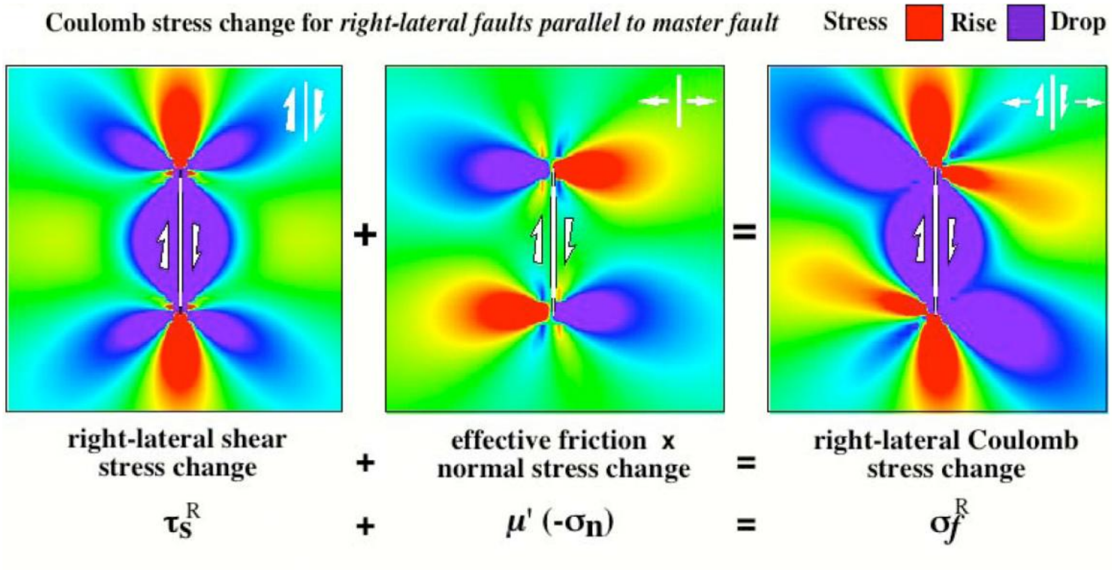

Figure 1.6: Illustration of the Coulomb stress change resolved on a right lateral fault (from King et al, 1994)

1.3 Short InSAR Case Studies from Anatolia

The following short case studies will give a better perspective about the difficulties and shortcomings of InSAR. Even in cases where the data are abundant, InSAR may fail to produce the expected results.

1.3.1 Case Study I: Afyon-Akşehir (Sultandağı) Earthquakes

The Akşehir fault is a 90 km long NW-SE trending fault located in western Anatolia between the towns of Çay (Afyon) and Doğanhisar (Konya). Tectonically, it represents the northern boundary of the Antalya Block with the Isparta Angle (Barka *et al.*, 1995). It is known to be an active fault both from the historical and instrumental records. Recent paleoseismological studies provide evidence for historical activity on the fault with similar magnitudes (Akyüz *et al.*, 2006). Akşehir-Afyon graben and the 2519 m high (~1000 m relative to the surrounding plains) Sultandağ mountain range are the prominent tectonic features in the surrounding area. The graben is filled with two major sequences: (1) a deformed fluvio-lacustrine sequence of Early-early Late Miocene age, which is over 300 m thick; and (2) an undeformed fluvio-lacustrine sequence of Plio-Quaternary age, which is 670 m thick (Koçyiğit and Özacar, 2003).

Two earthquakes occurred along the Sultandağı mountain range near the town of Çay in December 15th 2000 and February 3rd 2002 with magnitudes 6.0 and 6.4 respectively. The focal mechanism solutions of the earthquakes describe normal faulting which shows that the Akşehir fault is the causative fault. Therefore, the Sultandağı thrust fault that was previously mapped as an active fault (Şaroglu *et al.*, 1987; Boray *et al.*, 1985; Barka *et al.*, 1995) is now regarded as an inactive fault (Koçyiğit and Özacar, 2003).

Table 1.2: Radar images from the descending orbit of the ERS2 satellite that are used to form the six interferograms. $B_\perp$ perpendicular baseline (m), H_a altitude of ambiguity (i.e. elevation change required to create one fringe due to topography).

	Master		**Slave**		**B⊥ (m)**	**H_a (m)**	**Frame**	**Track**	**ΔDate**
#	**Orbit1**	**Date1**	**Orbit2**	**Date2**					
1*	32669	20/07/2001	38180	09/08/2002	27	372.3	2832	250	385
2	29663	22/12/2000	38180	09/08/2002	-110	91.3	2832	250	595
3	24152	03/12/1999	29663	22/12/2000	-15	670.1	2832	250	385
4	20645	02/04/1999	29663	22/12/2000	-99	101.5	2832	250	630
5	27659	04/08/2000	29663	22/12/2000	-122	82.4	2832	250	140
6	28933	01/11/2000	29935	10/01/2001	128	78.5	2832	21	70

*the interferogram shown in Figure 1.8

The main objective of using InSAR in this case is (1) to pinpoint the location of the two earthquakes which only the last one produced discontinuous surface ruptures of up to 30 centimeters in vertical; (2) to observe the extend of the faulting; (3) to deduce the mechanism of the events. All the interferometrically possible pairs of ERS2 radar data are obtained and 6 different interferograms (2 of them for the first event) are calculated in order to analyze both of the events (Table 1.2).

Unfortunately, none of the interferograms are good enough to analyze the events. Most of them contain dominant atmospheric effects or do not reveal any clear evidence of surface deformation. Although there are closely spaced fringes that exist between the Eber and Akşehir lakes in the interferogram shown in Figure 1.8, it is difficult to attribute them to earthquake related surface changes. They most probably represent the landslides observed in that particular area which were triggered by the second earthquake.

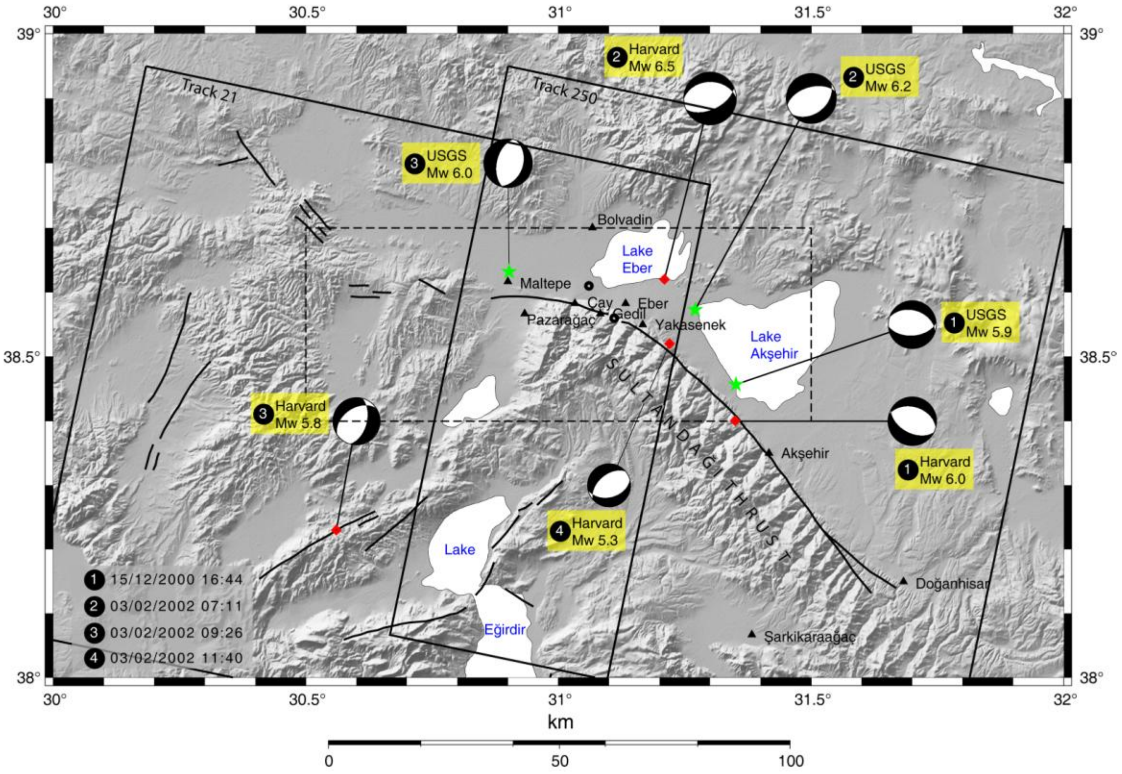

Figure 1.7: Epicenters and the focal mechanism solutions of the Afyon-Akşehir (Sultandağı) earthquakes of 2000 and 2002. The black rectangles represent the area covered by the InSAR frames; the dashed rectangle inside shows the area of Figure 1.8b.

Discontinuous surface seen in the field near Maltepe and Çay (Emre *et al.*, 2003) cannot be seen as a phase change in the interferograms. Even though the contribution from topography is removed with the usage of 3-arc second SRTM digital elevation model (and also with a better DEM produced from ASTER images) the atmospherical fringes that surround the higher elevations of the Sultandağı mountain range still remain. Since

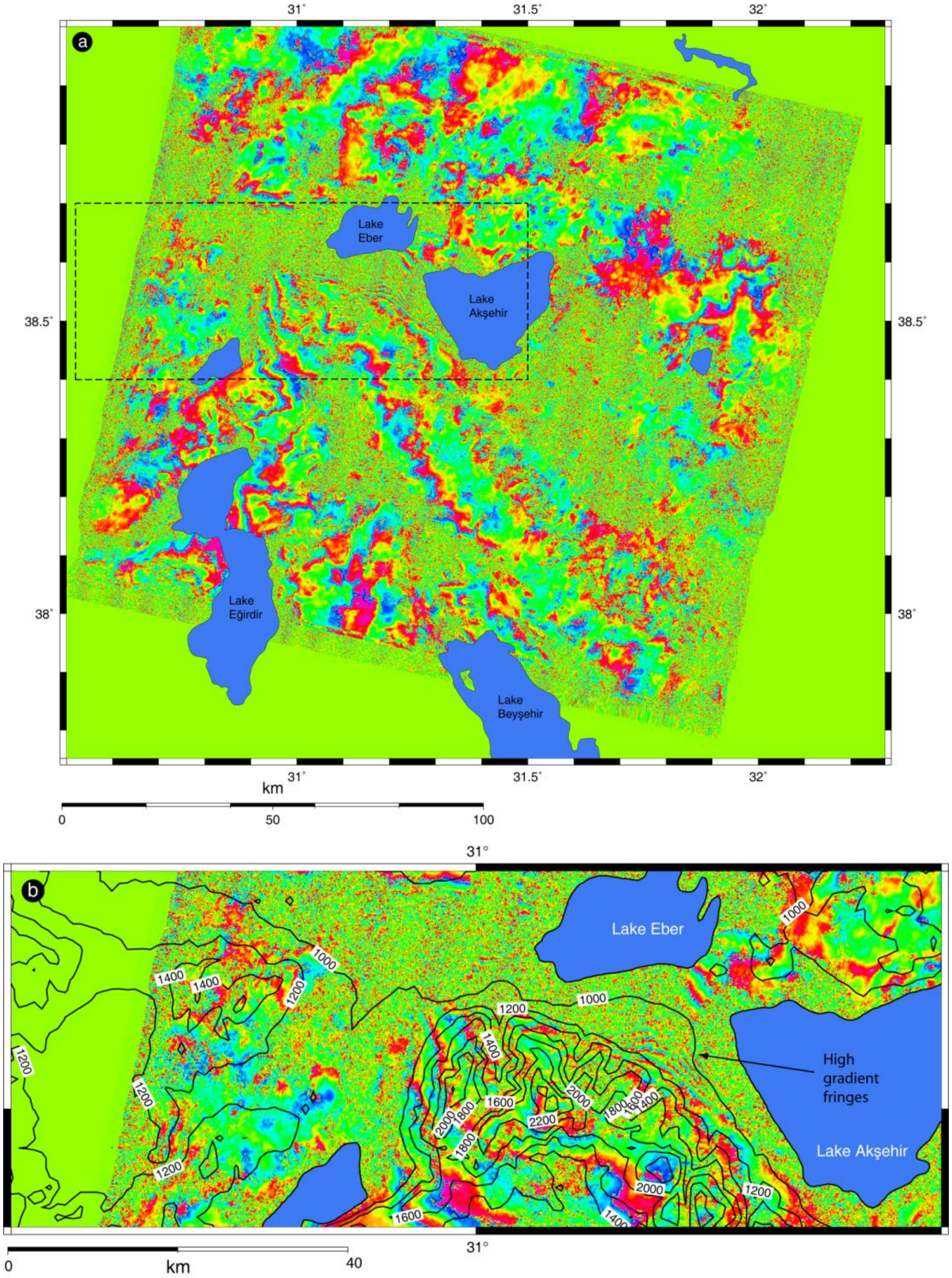

Figure 1.8: **a.** Interferogram. **b.** The area shown in Figure 1.7 and 1.8a with the dashed rectangle. The atmospheric fringes clearly surround the Sultandağı Mountain. The high gradient fringes between 1000 and 1200 meters are most probably associated with earthquake triggered landslides.

they “hug” the topography they must be phase differences caused by the trophospheric delay anomaly (Delacourt *et al.*, 1998; Beauducel *et al.*, 2000). In addition to these artifacts, the remaining parallel fringes throughout the image suggest that the orbital errors cannot be eliminated fully. The Doppler problem mentioned in the previous sections is also encountered during the process of these images. For example the data from orbit 38180 is taken during the zero-gyro mode of the ERS2 satellite.

In summary, although we have ordered all the available data, InSAR cannot provide useful information for the analysis of the two earthquakes in the region due to the aforementioned disadvantages and technical difficulties that arise from the observing platform during the studied era.

1.3.2 Case Study II: İzmir-Sığacık Earthquake

The earthquake activity in the Sığacık Bay of İzmir is one of the most disputed and discussed events of 2005 in Turkey. The seismic sequence is composed of 3 mainshocks which are given in Table 1.3.

Table 1.3: Mainshocks of the Sığacık Bay seismic activity (Aktar et al., 2007)

Mainshock	Date	Time (UTC)	Magnitude (Mw)	Latitude	Longitude	Depth	Strike	Dip	Rake
M1	17/10/2005	05:45	5.4	38.166	26.637	11	246	82	-172
M2	17/10/2005	09:46	5.8	38.174	26.676	11	238	85	177
M3	20/10/2005	21:40	5.9	38.191	26.696	10	50	84	-172

The Sığacık Bay activity is explained by a conjugate fault system of strike slip character that ruptured during the same sequence since aftershocks are distributed along two distinct lineations trending NE-SW and NW-SE (Fig. 1.9) (Aktar *et al.*, 2007). Seismic studies suggest that the three main events occurred on the NE-SW trending offshore fault (Benetatos *et al.*, 2006; Aktar *et al.*, 2007). Activity along the NW-SE trending deformation zone is therefore most probably triggered by the large shocks.

We have processed 2 pairs of InSAR data for the Sığacık bay activity (Table 1.4). Our best interferogram is given in Figure 1.9. It is clear that earthquake did not break the earth surface on the NW-SE trending fault on land since there are no fringes in that region. The interferograms supports the seismic observations in that the earthquake took place on the NE-SW trending offshore fault. Three fringes running parallel to the shore line north of the Sığacık bay demonstrate that part of the earthquake deformation occurs onshore.

Table 1.4: InSAR data for the Sığacık earthquakes of 2005 (Track 150). The second interferogram is shown in Figure 1.8. H_a is the altitude of ambiguity.

	Master			**Slave**			**Baseline (m)**	**H_a (m)**	**ΔDate**
#	**Orbit1**	**Satellite**	**Date1**	**Orbit2**	**Satellite**	**Date2**			
1	17739	Envisat	22/07/2005	19242	Envisat	04/11/2005	8.22	1223	105
2	18240	Envisat	26/08/2005	19242	Envisat	04/11/2005	22.02	456.5	70

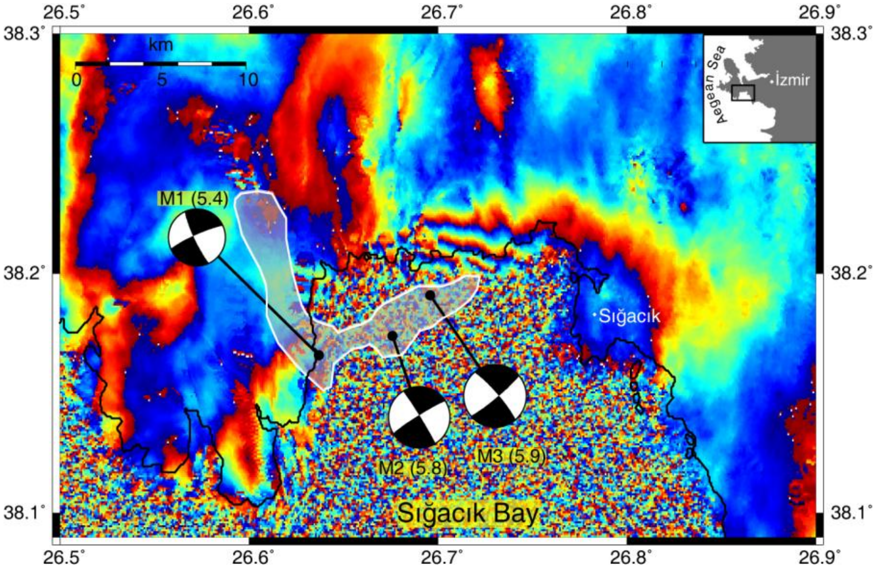

Figure 1.9: The interferogram of the Sığacık Bay activity in 2005. The area shown with a white transparent polygon is the place where majority of seismic activity occurred (from Aktar et al., 2007). The focal mechanism solutions belong to the three mainshocks M1, M2, M3 given in Table 1.3. Three fringes northwest of Sığacık indicate that the earthquake took place on the NE-SW trending zone. No surface deformation is present along the NW-SE trending zone.

Chapter 2

InSAR Observations of the Mw 6.0, Orta Earthquake of June 6, 2000 (NW Turkey): Reactivation of a Listric Fault

2.1 Introduction

On June 6, 2000, less than a year after the devastating 1999 İzmit (Mw 7.4) and Düzce (Mw 7.2) shocks, a moderate sized (Mw 6.0) earthquake struck the town of Orta located ~130 km east of the eastern termination of the Düzce rupture near Bolu (Fig. 2.1; Çakır et al., 2003a,b). Felt from the capital, Ankara (~70 km to the south), the earthquake caused minor property damage in the town of Orta and some villages to the west and gave rise to 3 human casualties with more than 200 injuries. The earthquake was somewhat surprising firstly because its epicenter is located in a region considerably far (30-35 km southward) from the plate boundary, North Anatolian Fault (NAF), where no active faults were previously reported to exist. In other words, the earthquake took place on an unknown intercontinental fault (Utkucu *et al.*, 2003). Secondly, the fault plane solutions show that the event is associated with an oblique-normal-slip fault trending at an unexpectedly high angle to the strike-slip NAF (Fig. 2.2). Most of the focal mechanism solutions from various different sources are in good agreement and indicate an oblique normal displacement either on an eastward dipping (24°-54°) and north-south

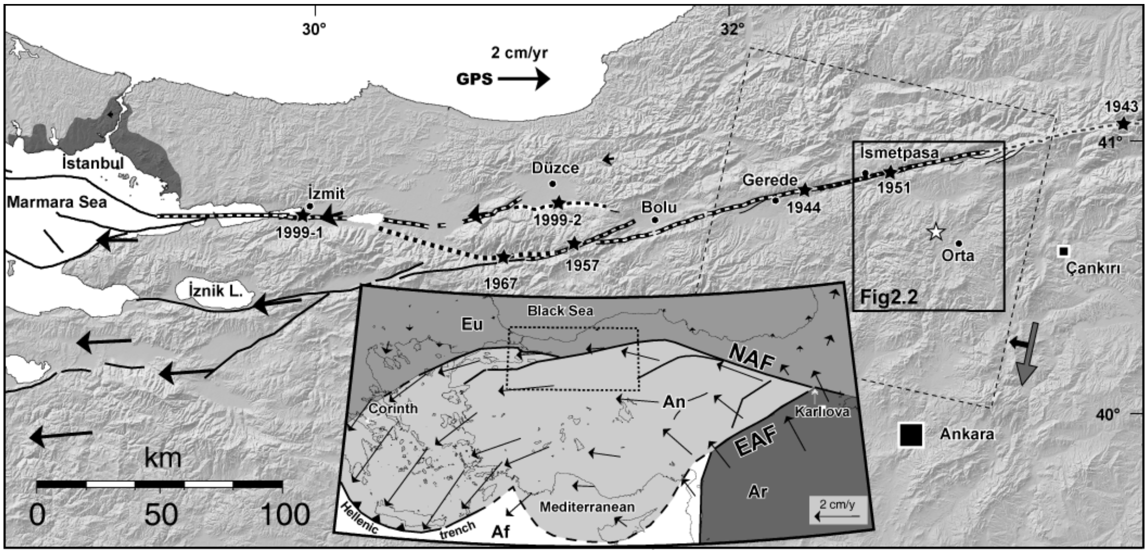

Figure 2.1: Tectonic map of the northwestern Turkey showing the active faults (solid black lines; Şaroğlu et al., 1992; Armijo et al., 2002), 20th century earthquake fault ruptures (two-color thick dashed lines with dates and black stars) along the North Anatolian Fault, and the location of the study area (box with solid lines) over shaded relief image produced from the Shuttle Radar Topography Mission (SRTM) 90-m-posting elevation data. Dashed box is the ERS SAR data frame (frame 2781 of track 479). The gray and black arrows attached together show the satellite flight direction (descending) and the line of sight direction (right looking), respectively. Epicenter of the earthquake of June 6, 2000 is shown with a white star. Inset map depicts the configuration of tectonic plates (Eu: Eurasia, Af: Africa, Ar: Arabia, An: Anatolia) in the Eastern Mediterranean region with GPS vectors (from McClusky et al., 2000) showing westward motion of the Anatolian block relative to the Eurasian plate via the right-lateral North Anatolian (NAF) and the left-lateral East Anatolian (EAF) faults.

trending left-lateral strike-slip fault or on a westward dipping (59°-80°) and northwest-southeast trending right-lateral strike-slip fault (Table 2.1). However, field investigations following the earthquake did not reveal a clear fault rupture at the Earth's surface. Instead, some cracks, fissures and minor landslides were observed to have been caused by the earthquake (Emre *et al.*, 2000; Koçyiğit *et al.*, 2001). Running through the village of Dodurga, most of these fractures apparently fall in a narrow zone that is

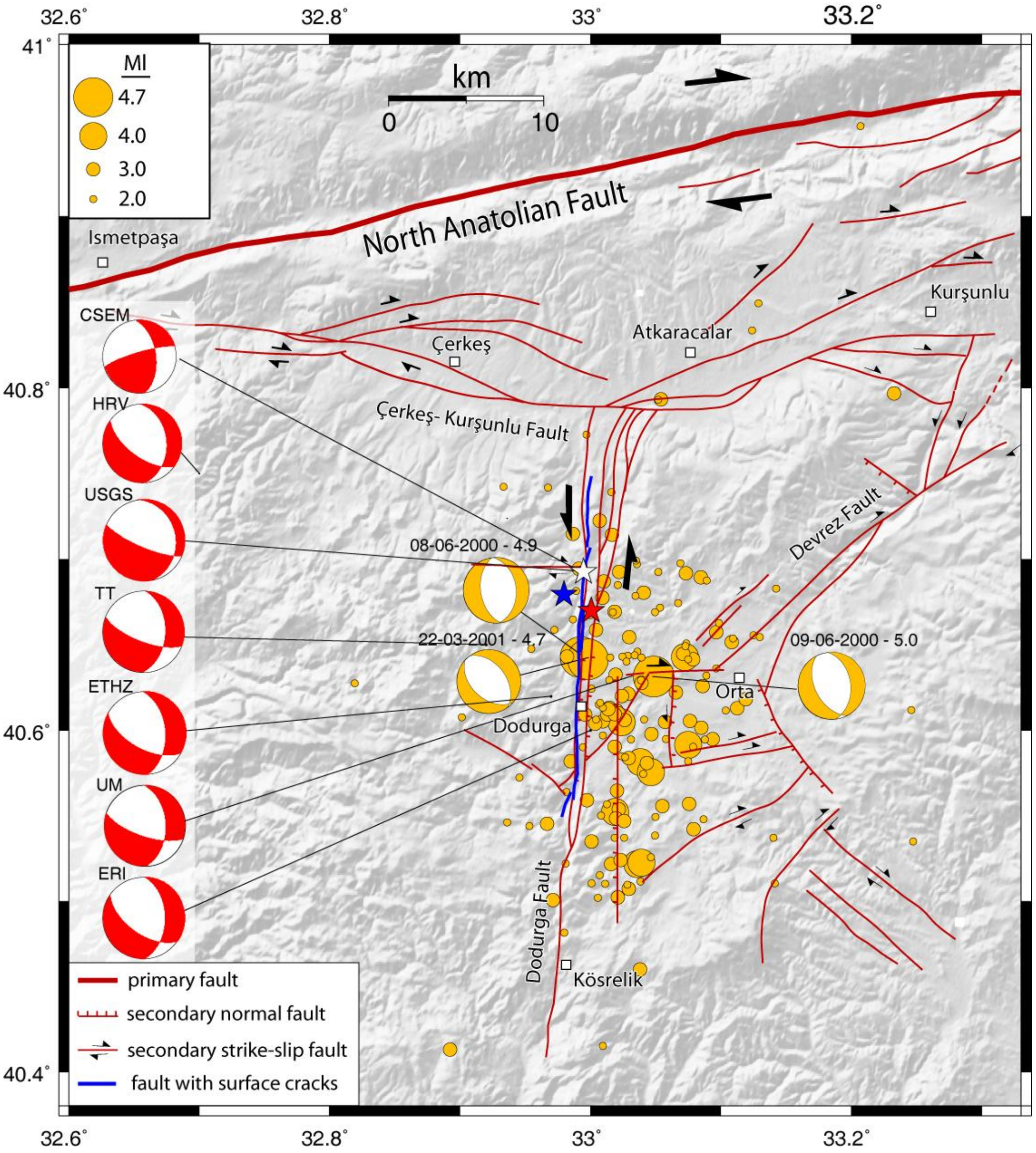

Figure 2.2: Active fault map of the Orta region from Koçyiğit et al. (2001), Emre et al. (2000) and Şaroğlu et al. (1992). Blue line is the Dodurga fault along which some cracks and fissures were observed and claimed by Emre et al. (2000) to be the fault that is responsible for the Orta earthquake. Red beach balls are focal mechanism solutions of the main shock from various sources. Red, blue and white stars mark the epicenter of the earthquake of June 6, 2000 estimated by the Earthquake Research Department of the General Directorate of Disaster Affairs (ERD), Kandilli Observatory and USGS, respectively. Yellow circles are the aftershocks recorded by ERD during the first six months following the main shock with focal mechanisms (yellow beach balls) from ETHZ. North-south elongation of aftershocks suggests that the nodal plane dipping to the east is most likely the one that represent the fault rupture, an inference being also supported by their concentration on the eastern side of the Dodurga fault.

approximately 10-km-long and trends roughly in the north-south direction (Fig. 2.2) (Emre *et al.*, 2000). In addition, some of the fractures with a north-south strike appear to display left-lateral sense of slip, in agreement with the focal mechanism solutions. Taking into account these observations and the subsequent fault mapping based on aerial photography and field observations, Emre *et al.* (2000) concluded that the earthquake must have taken place on a north-south trending left-lateral fault that they later named as the Dodurga fault. Considering the distribution of the surface cracks and the fore- and after-shocks, and their new fault map shown in Figure 2.2, Koçyiğit *et al.* (2001) supported the inference of Emre *et al.* (2000) that the event is most probably due to the reactivation of the Dodurga fault. Teleseismic waveform inversions by Utkucu *et al.* (2003) and Taymaz *et al.* (2007) indicate up to 2.3 m oblique slip centered around 5-6 km of depth on a moderately dipping fault (46-47°).

Table 2.1: Fault plane solutions of the Orta earthquake of June 6, 2000, estimated by various institutions and researchers (USGS: United State Geological Survey; CSEM: European-Mediterranean Seismological Centre; HRV: Harvard; ETHZ: Eidgenössische Technische Hochschule Zürich; ERI: Earthquake Research Institute, Tokyo; TT: Taymaz et al., 2007; UM: Utkucu et al., 2003; InSAR: this study). Errors are standard deviations.

Lon. (°E)	Lat. (°N)	Depth (km)	Nodal plane 1			Nodal plane 2			Mo (10^{18} Nm)	Slip (cm)	Source
			Strike (°)	Dip (°)	Rake (°)	Strike (°)	Dip (°)	Rake (°)			
32.992	40.693	3.00	349	24	-37	113	76	-110	1.3	--	USGS
--------	--------	10.00	352	54	13	254	80	143	0.8	--	CSEM
32.700	40.750	15.00	356	39	-47	126	62	-119	1.1	--	HRV
32.970	40.620	15.00	356	49	-44	119	59	-129	1.4	--	ETHZ
33.000	40.600	33.00	360	48	-47	125	58	-126	1.3	--	ERI
32.980	40.700	08.00	002	46	-29	113	70	-132	1.4	100 *	TT
33.030	40.630	05.00	358	47	-30	109	69	-133	1.0	42	UM
32.944	40.631	4.8	360*	41	-31	114	70	-127	1.16	118	InSAR single
±0.17	±0.05	±0.1	--	±0.1	±3	--	--	--	--	±12	fault model
32.929	40.634	5.2	360*	37	-31	116	72	-123	1.23	101	InSAR two-
±0. 24	±0.06	±0.1	--	±0.1	±3	--	--	--	--	±12	fault model

* Parameter is fixed

Previous earthquakes have shown that such surface cracks and fissures observed in the field should be interpreted with caution since they may not necessarily indicate the location of the causative fault of the earthquake (e.g. Talebian *et al.*, 2004; Çakır et al., 2006, Akoğlu *et al.*, 2006). Therefore, the kinematics, location and geometry of the ruptured fault are still open to questions owing to the absence of a clear surface rupture and a precise determination of aftershock locations. The objective of this study is thus to provide better constraints on the kinematics, fault geometry and the rupture parameters of the 6 June 2000 Orta earthquake using InSAR data. We map the coseismic surface deformation field of the earthquake using InSAR with the European Space Agency's ERS-2 satellite data. We then model the coseismic interferograms using elastic dislocations on rectangular faults with a nonlinear inversion procedure. Taymaz *et al.* (2007) also deduce fault parameters by inverting separately one of the coseismic interferograms of the earthquake we used in this study. However, they do not discuss or reconcile the discrepancy between their modelling results and field observations. Here, we analyze together with the field observations two additional and independent coseismic interferograms that enable us to interpret the surface deformation field and deduce the rupture characteristics with more confidence and in more detail. We also use the modelling results to interpret the active tectonics of the region, and finally discuss the pitfalls and shortcomings in determining the source parameters of earthquakes on the basis of field observations, seismicity and InSAR data when faulting does not reach to the surface.

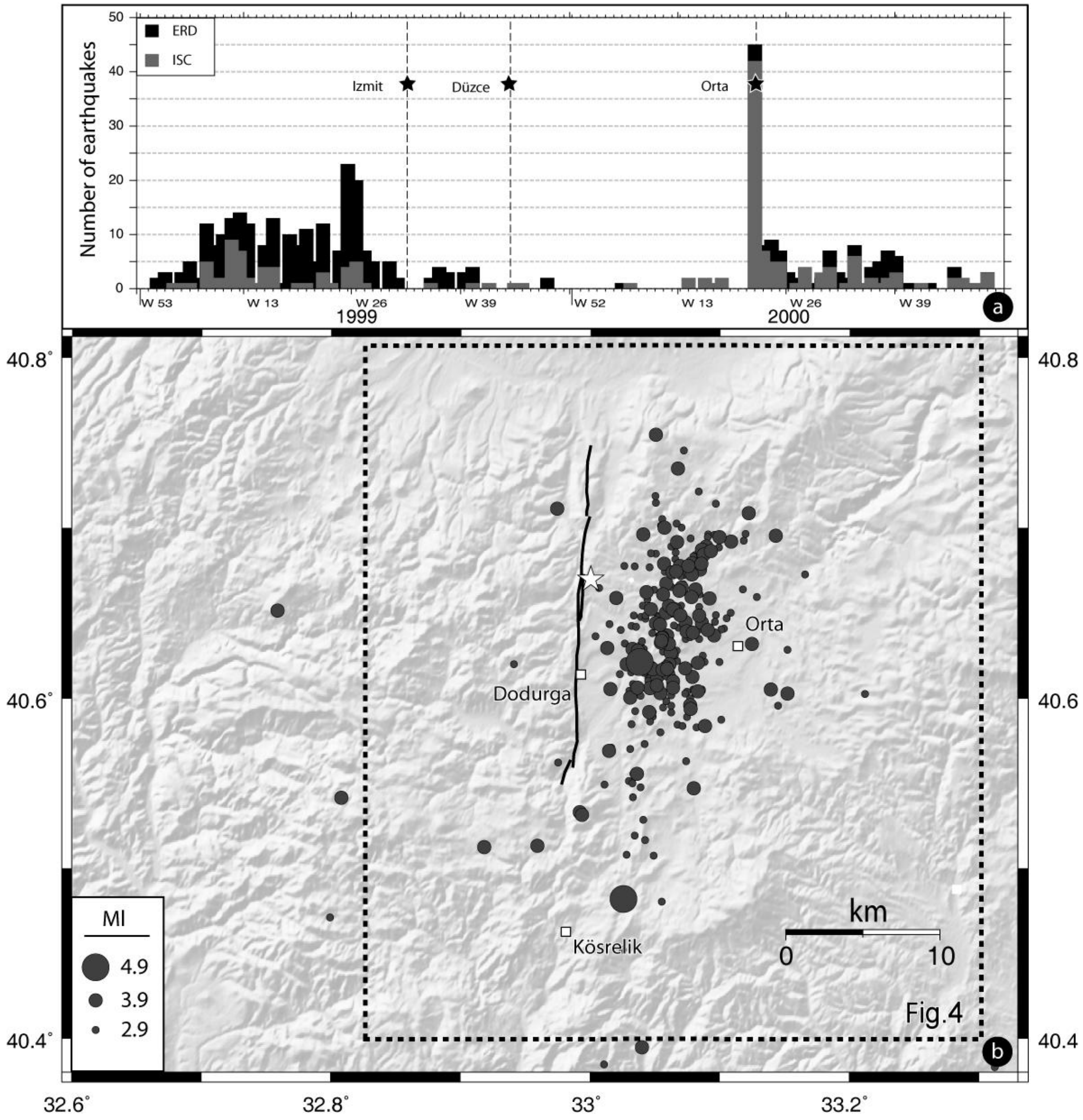

Figure 2.3: a. Seismicity in the Orta region (32.7°-33.3°E, 40.4°-40.85°N) before and after the main shock between January 1999 and December 2000, based on the catalogues of ERD and International Seismological Center (ISC). Lasting about 8 months as from the beginning of the year 1999, an earthquake storm occurred in the epicentral area. The seismic activity interestingly ceased after the 1999 Izmit and Düzce earthquakes. The quiescence was however broken by the Orta earthquake about 8-10 months later. **b.** Distribution of foreshocks between January 1999 and June 2000. Note that, like the aftershocks, seismic activity before the mainshock is concentrated to the east of the Dodurga fault (black lines) and distributed roughly in north-south direction, supporting the inference that this fault is the one that ruptured during the earthquake. Dashed rectangle is the area of Figure 2.4.

2.2 Seismotectonic Setting

The main neotectonic structure of the study area is the North Anatolian Fault (Fig.2.1). The epicentral area of the Orta earthquake of June 6, 2000, is located 30-35 km south of the İsmetpaşa creeping section of the NAF (Figures 2.1 and 2.2; Çakır et al., 2005). Extending for over 1500 km from the Karlıova triple junction in eastern Turkey to the Corinth Rift in central Greece, the right-lateral NAF is one of the most prominent and seismically active structures of the Eastern Mediterranean region (Fig. 2.1) (Barka, 1996; Armijo *et al.*, 1999; Şengör *et al.*, 2005). It accommodates, along with its conjugate left-lateral East Anatolian Fault (EAF), the westward extrusion of the Anatolian plate resulting from the collision between the Arabian and Eurasian plates in late Miocene (Şengör *et al.*, 1985). In north central Turkey, it follows an arc nearly parallel to, and about 100 km from, the Black Sea coast between Karlıova and Bolu, enabling the contour clock wise rotation of the Anatolian plate about a pole located in Sinai (Egypt) with a slip rate of about 2.4 cm/y (Fig. 2.1) (McClusky *et al.*, 2003; Reilinger *et al.*, 2006). However, the circle arc of the Anatolian plate rotation does not quite coincide with the trace of the NAF; while the plate motion is almost parallel to the NAF along the NW-SE trending portion of the arc in the east, imposing pure strike-slip motion on it, it is slightly oblique along its NE-SW trending section in the earthquake area to the west, promoting a minor thrust-slip component that is, according to the field observations (Hubert-Ferrari *et al.*, 2002), taken up by secondary thrust faults (McClusky *et al.*, 2000; Flerit *et al.*, 2003). Field evidence suggests that strike-slip deformation in this section of the NAF (i.e. north-central Turkey) is highly localized with large earthquakes occurring on the same fault segments over many seismic cycles

(Kozaci *et al.*, 2007). To the west of Bolu, the NAF is no longer a simple and single structure but, splits into several branches where the strike-slip regime becomes overwhelmingly transtensional (Armijo *et al.*, 2002).

While the NAF and EAF have attracted interest of many researchers due to the high rate of recent and historical seismic activity and the presence of conspicuous morphotectonic features associated with active faulting along them, little attention has so far been paid to the secondary active faults around them. Therefore, no active faults were reported to have been present in the Orta region before the earthquake nor does the Active Fault Map of Turkey (Şaroğlu *et al.*, 1992) include the causative fault of the Orta event (Fig. 2.1). Some secondary fault strands splaying from the NAF to the south are reported to be present east of the earthquake area (Bozkurt, 2001, Koçyiğit *et al.*, 2001). But no active faults of north-south trend were reported before the Orta earthquake. Neotectonic map of the epicentral area and the surrounding regions is done by Koçyiğit *et al.* (2001) shortly after the earthquake (Fig. 2.2). In the earthquake area, they mapped in detail the Dodurga fault claimed by Emre *et al.* (2000) to have ruptured during the Orta earthquake. They proposed that it is not a single structure but, comprises closely spaced (a few km) and N-S trending sub parallel strike-slip faults with significant normal component (Fig. 2.2). In addition, their map shows numerous other faults around the epicentral region. However, as can be seen in Figure 2.2, most of these faults do not have any morphological expression visible in the topography at a resolution of 90 meters (i.e. the SRTM digital elevation data), suggesting that most of the lineaments seen in the aerial or satellite imagery are inactive faults or have very low Quaternary activity, or have possibly nontectonic origin.

The NAF experienced a well-known sequence of westward migrating earthquakes in the last century between 1939 and 1999, three of which ruptured, with surface breaks, the NAF in the vicinity of the Orta earthquake region; the 1943 (Mw 7.6), 1944 (Mw 7.3) and 1951 (Mw 6.9) earthquakes (Fig. 2.1) (Toksoz *et al.*, 1979). Kandilli Observatory, Earthquake Research Department of the General Directorate of Disaster Affairs (ERD) and the United States Geological Survey located the epicenter of the earthquake at about 10 km northwest of the town of Orta roughly on the central part of the Dodurga fault (stars in Fig. 2.2). The earthquake was not a total surprise because the region had been seismically active quite for some time. The seismic activity started one year and a half before the main shock during which ~272 foreshocks of magnitudes reaching up to 4.9 were recorded by the Earthquake Research Institute of General Directorate of Disaster Affairs (Fig. 2.3b). Interestingly, seismicity vanished dramatically after the August 17, 1999, Izmit earthquake (Fig. 2.3a); only a few earthquakes occurring during the last 7-8 months before the main shock. This may suggest a possible stress interaction between the Orta and 1999 Marmara earthquakes. About 140 aftershocks took place within six months following the earthquake. Of these, ten are larger than magnitude 4. The largest one was an M=5 normal event, and occurred ~5 km south east of the main event three days after the mainshock. Focal mechanism solutions of two other large aftershocks also indicate nearly pure normal faulting (Fig. 2.2). Aftershocks were not recorded by a local network and thus were not precisely located.

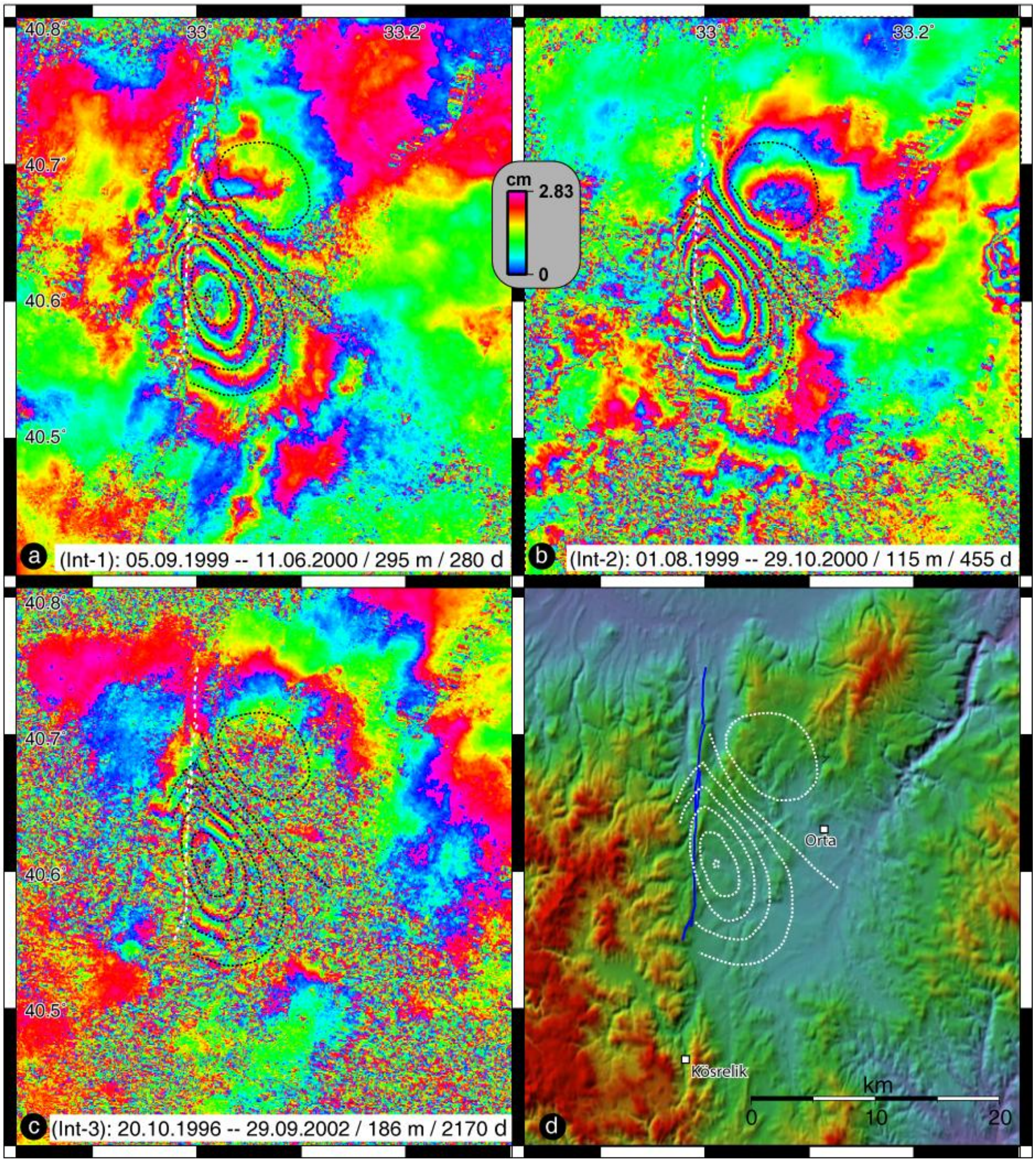

Figure 2.4: a-c. Three independent coseismic interferograms (Int-1, Int-2, Int-3) of the Orta earthquake of June 6, 2000. Date of the orbit pairs, altitude of ambiguity (m), and temporal baselines (time difference in day between the acquisitions of the two images) are given in white boxes at the bottom of the interferograms. Each fringe (a full color cycle) shows half a wavelength range change (i.e. 2.83 cm) between the radar and Earth's surface. The unit vector along the range is 0.35 -0.088 0.92 in east-north-up coordinates. White dashed line is the surface trace of the Dodurga fault. Star marks the earthquake epicenter determined by ERD. Black dashed lines show the digitized fringes of int-2 (southern lobe) and int-3 (northern lobe) used in the inversion. **d**. Shaded SRTM relief image of the epicentral region. Note that the Dodurga fault (i.e. blue line) crosscuts the fringes in the northern side of the tear-drop shaped fringe lobe.

Nevertheless, similar to the foreshocks (Fig. 2.3b), most of them are concentrated on the eastern side of the Dodurga fault and are distributed roughly in north-south direction, suggesting that the earthquake is indeed associated with a north-south trending and eastward dipping fault in agreement with focal mechanism solutions (Fig. 2.2; Table 2.1).

2.3 Surface deformation field from InSAR

In order to examine the ground displacements resulting from the Orta earthquake of June 6, 2000, we produced several coseismic interferograms using SAR data acquired by ERS-2 satellites from descending orbits (radar looking towards west; Fig. 2.1; Track: 479; Frame: 2781). Table 2.2 lists the SAR data used to calculate the coseismic interferograms shown in this chapter. Descending SAR images are the only geodetic data available for this earthquake; there are no suitable pairs from ascending images in the ERS SAR catalogue. The raw data are processed using JPL's (NASA) public domain RoiPac software and precise satellite orbits from Delft University (Scharroo and Visser, 1998). Contribution of topography is simulated and removed from the interferograms using the Shuttle Radar Topography Mission (SRTM) 3-arc-second posting digital elevation model (Farr *et al.*, 2007).

Figure 2.4 shows the best three interferograms that are filtered using a weighted power spectrum technique (Goldstein and Werner, 1998). Each fringe, that is, one cycle of phase difference (e.g. from blue to blue) in the interferograms corresponds to a range change of 2.83 cm along line of sight (LOS) between the radar and the Earth's surface.

Table 2.2. Interferometric pairs used to construct the coseismic SAR interferograms shown in Figure 2.4 (Int-1, Int-2 and Int-3). $B_\perp$, Δ and H_a are perpendicular baselines, temporal baselines and altitude of ambiguity, respectively.

Interferogram	Date-1	Orbit-1	Date-2	Orbit-2	$B_\perp$ (m)	Δ days	H_a (m)
Int-1	19990905	22878	20000611	26886	34	280	295
Int-2	19990801	22377	20001029	28890	87	455	115
Int-3	19961020	07848	20020929	38910	54	2170	186

Coherence in the interferograms decreases with increasing temporal baseline (i.e. time lapse between the image acquisitions) but, is well preserved even in the interferogram spanning 6 years (Int-3; Fig. 2.4c). This is owing to sparse vegetation cover and limited agricultural activity in this region of arid climate, which allowed us earlier to study the creeping phenomenon along the İsmetpaşa section of the NAF to the north using long term SAR interferometry (Çakır et al., 2005). The high signal correlation is also partly owing to the fairly flat topography of the region where most of the deformation fringes are located (Fig 2.3d). Although temporal decorrelation increases to the west of the Dodurga fault in the hilly areas where the topographic elevation increases ~350 meters in a very short distance, some closely spaced fringes are still visible as a result of the high altitude of ambiguity (sensitivity of the interferograms to the topography) of interferograms (Table 2.2). These fringes may partly contain atmospheric noise correlated with topography.

All the interferograms are independent from each other, that is, they do not share a common master or slave image (Table 2.2). This allows us to better evaluate atmospheric effects and have high degree of confidence in our interpretation of fringes.

As may also be seen from Figure 2.4, subtracting interferograms from one another shows that the difference between them is small and thus they do not contain any significant atmospheric artifacts. One of the interferograms (Int-2) spans a postseismic period of ~4.5 months and the other (Int-3) ~2 years. Comparison of the interferograms also reveals that postseismic deformation must be included in the noise level of the interferograms. The main fringe pattern in all of the interferograms is a teardrop-shaped lobe of up to 14 cm (~5 fringes) of range increase with a northward pointing cusp and a NW-SE trending long axis (Fig. 2.4). Following Amelung and Bell (2003), we refer this fringe pattern as the teardrop feature. In all the interferograms there is also a second but, much smaller fringe lobe of circular shape to the north of the teardrop feature. Although its shape, location and amplitude slightly vary from one interferogram to the other, it shows an area of up to 5 cm range decrease. The most likely and reasonable explanation for the cusp seen in the fringe pattern of all the interferograms is the presence of a nearby fault rupture. Continuity of the fringes around the cusp suggests that the rupture did not quite reach to the surface. The first fringe in the south however abuts the fault and do not seem to continue on the western side of the fault, implying that the faulting might have indeed reached to the surface along this part of the fault as suggested by Emre *et al.* (Emre *et al.*, 2000).

2.4 Source Model of the Orta Earthquake

We model the interferograms in an inverse approach using dislocations in a homogenous and elastic half space. To perform the inversions, we employ a residual-minimization procedure based on a downhill simplex simulated annealing algorithm (Donnellan and

Lyzenga, 1998). A χ^2 goodness of fit objective function is formed from SAR data set and its measurement uncertainties. Function evaluations are based on the analytical solutions for rectangular dislocations in a homogenous half-space given by Okada (1985). Simulated annealing parameter estimation process is able to locate the global objective function minimum by climbing out of local minima. For the inversions, we use digitized fringes (Fig. 2.4b) instead of unwrapped data because some parts of the teardrop feature cannot be properly unwrapped due to the temporal decorrelation. This also allows us to reduce the large amount of SAR data down to about 1600 data points and hence expedite the modelling process. We sample the interferograms in such a way that data spacing increases from the edge to the center of the teardrop feature, which to some extent is similar to the quadtree sampling of unwrapped interferograms (Jònsson *et al.*, 2002). Nine fault parameters can be solved by the inversion; longitude, latitude, strike, dip, depth, width, length, strike-slip and dip-slip. Although orbital residuals are not taken in to account in the inversions, visual inspection of the interferograms confirms that none of them contains orbital residuals more than a fringe at the scale of the interferogram (i.e. ~100x100 km). Therefore, bias in the fault parameters introduced by orbital residuals should be minimal.

In the first stage of modelling, we invert all the parameters holding only the fault dip fixed. Inversions with a fixed fault dip ranging between 20° and 70° show that the best fit model has an RMS misfit of ~8 mm and is obtained with 110 cm of oblique left-lateral slip on a 11-km long fault dipping 36° towards the east and striking 348° (i.e. N12°W) (Figure 2.5a).

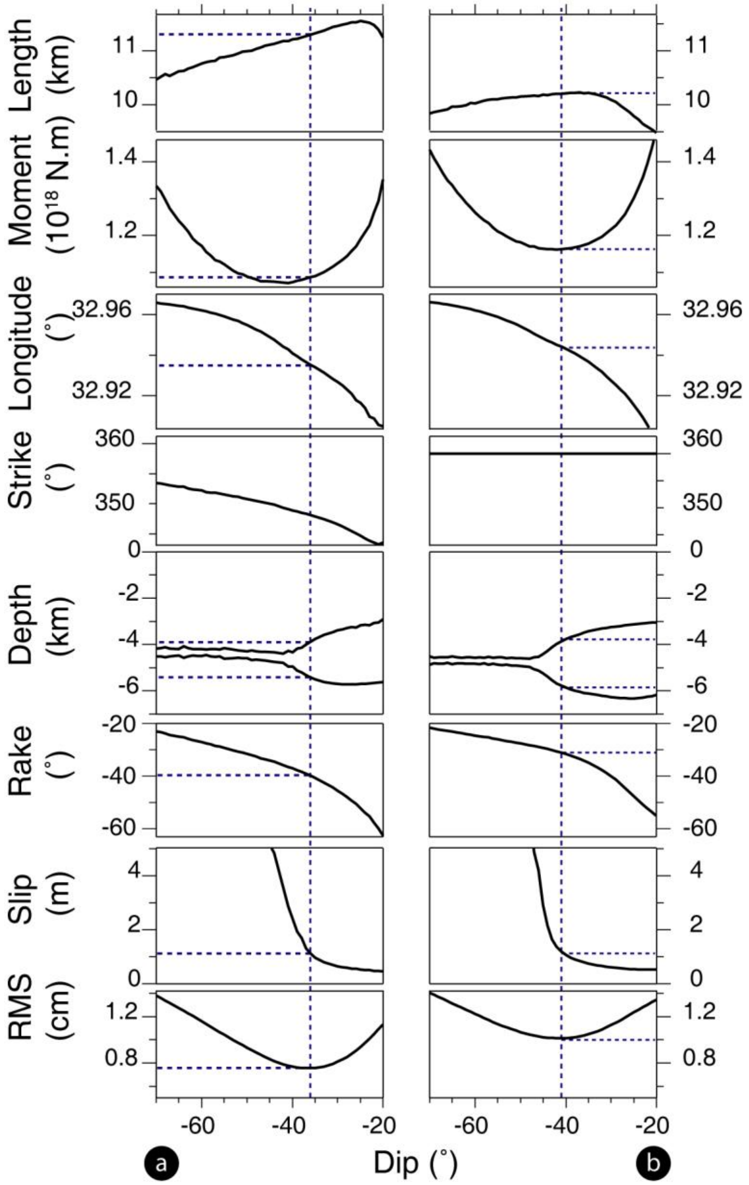

Figure 2.5: Plots showing the variation of fault parameters and root mean square (RMS) misfit with a fixed fault dip between 20° and 70° when the SAR data set is inverted (**a**) keeping all the other parameters free or (**b**) holding also the fault strike fixed. The best fit with the free inversion has a ~8 mm of RMS misfit and is obtained with a fault dipping 36° to the east. When the fault strike is kept fixed at 360° (i.e. north-south) approximately parallel to the strike of the Dodurga fault, most of the model parameters remains essentially the same. Faulting is now dominantly strike-slip (-31° of rake) on a steeper fault (41°). Dashed lines are drawn for a better visualization of the parameters predicted by the best fitting models.

Although the strike of the best fit fault is not in disagreement with all of those determined from seismology, it contradicts with the field observations because it crosscuts the Dodurga fault and a fault with such a NNW-SSE trend does not seem to exist in the epicentral area (Fig. 2.2). Therefore, in the second stage of modelling, we invert the fault parameters keeping the fault strike fixed at 360° (i.e. north-south), that is, roughly parallel to the strike of the Dodurga fault.

What essentially changes regarding with the best fit model when the fault strike is held fixed is the decrease in the fault rake from 40° to 31° (Fig. 2.5b). Almost all the modeled faults with various dip angles are now located on the eastern side of the Dodurga fault (Fig. 2.6). The best fit to the SAR data in both modelling steps is obtained with faults with rather low dip angles (37°-41°), in agreement with the seismological estimates (e.g. USGS and Harvard solutions; Table 2.1). Such low-angle faults are known to exist elsewhere but, are normally associated with pure dip-slip normal faulting that may be facilitated by the presence of unusually high pore fluid pressure on a preexisting plane of weakness or rotation of the stress field at the hypocentral depth within the brittle layer (Bernard *et al.*, 1997; Westaway, 1999). Thus, the dominant strike slip component of this earthquake makes it interesting and is somewhat similar to the Düzce earthquake that took place on a surprisingly low angle (~60°) fault with nearly pure strike-slip displacement (Bürgmann *et al.*, 2002, Çakır *et al.*, 2003).

As also noted by Taymaz *et al.*, (2007) there are tradeoffs between several fault parameters. For example, as seen in Figure 2.5, dip angle tradeoffs with slip and also with rake such that slip decreases with dip (Figure 2.5).

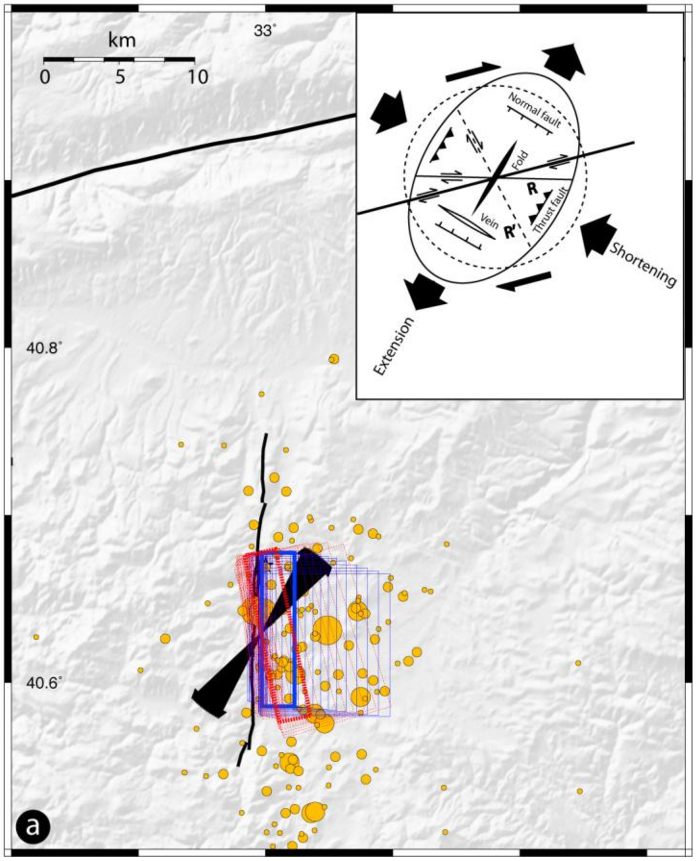

Figure 2.6: Map showing the surface projections of the rectangular dislocation planes predicted by the inversion with a fault dip ranging between 20° and 70° when the strike being held free (red dashed boxes) or kept fixed at north-south (blue solid boxes). Best fitting faults are shown with thick dashed lines. Note that when the strike is let free, the inversions predict NNW-SSE trending faults that crosscut the Dodurga fault (black lines) to the north. Yellow circles are aftershocks as in Figure 2.2. Black arrows are the T-axes of the focal mechanism solutions calculated from all the models shown in Figure 2.5 with dip angles ranging between 30° and 70°. Inset shows a strain model explaining subsidiary structures along an active fault with a simple shear model. R and R′ shears form at an acute angle to the shortening direction. In this context, the Dodurga fault is an R′ shear fracture. T-axes orientation is sub-parallel to the direction of extension, suggesting that the Dodurga fault and the North Anatolian fault are the products of the same stress regime.

Thus, one parameter must be known or held fixed at a value consistent with some fault scaling laws (e.g. Wells and Coppersmith, 1994) to constrain the other one. The upper boundary for an acceptable fault dip can be constrained by the amount of slip and the width of the fault. With increasing amount of dip, while the fault width gets thinner and thinner becoming less than half a km, the slip reaches over 5 m above ~47° (Fig. 2.5b). Therefore, faults dipping above ~47° have unusual aspect ratios and predict abnormally high coseismic slip for an earthquake of magnitude 6 (e.g. Wells and Coppersmith, 1994). Despite such tradeoffs, some parameters like, the length, location, depth range of faulting and moment, are well determined.

Figure 2.7a shows the synthetic interferogram obtained by projecting to the satellite the 3D surface deformation predicted by the best fitting model with a north-south striking fault. Overall fringe pattern of the observed interferograms are well reproduced by the model. The excellent fit between the model and data is demonstrated by the residual interferograms plotted in Figures 2.7b and 2.7c. Model fault parameters, including the geodetic moment, are also in good agreement with seismological observations (Table 2.1). However, the relationship between the modeled fault at depth and those mapped at surface is not quite obvious and thus requires some explanation. As illustrated in the map and the profile plotted in Figure 2.7a, the surface trace of the best fit fault will be located 4-5 km west of the Dodurga fault if it is projected up dip to the surface (white dashed line in the map and in the inset profile). Otherwise, the modeled fault will require a sharp decrease in the dip angle if it is to be connected to the Dodurga fault at surface (blue line in the inset profile). Arranged in a configuration similar to that illustrated in the profile shown in Figure 2.7a, the Dodurga fault might also have been reactivated together with its master fault as a synthetic fault. Therefore, the earthquake might have been associated with multiple ruptures similar to the 25 February 1981

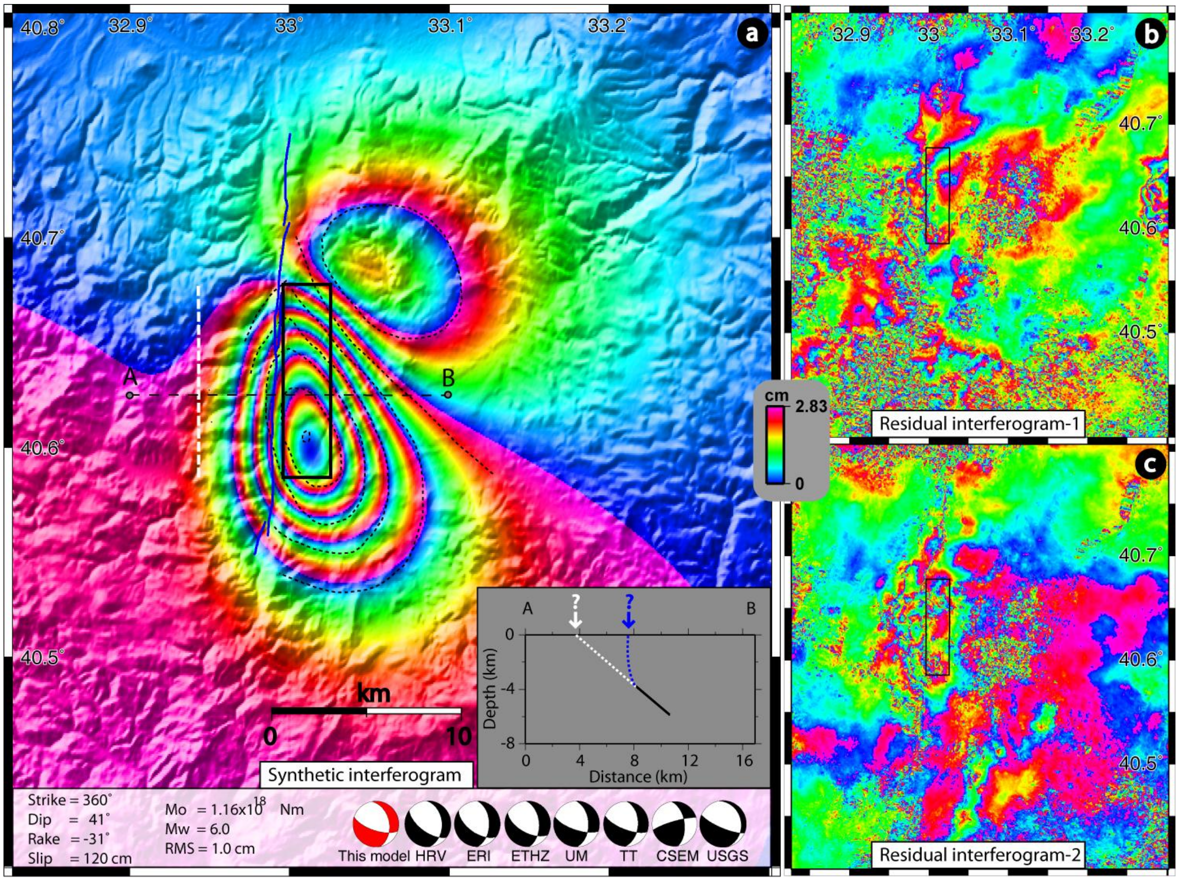

Figure 2.7: **a.** Synthetic interferogram predicted by the best fitting single-fault model with a north-south strike, 41° eastward dip and -31° rake (left-lateral with normal component). Moment (Mo), moment magnitude (Mw) and the RMS misfit values are indicated at the bottom (see Figure 2.5b for other parameters). Digitized fringes (dashed lines) used in the inversion are shown for visual comparison between the observed and modeled fringes. Also shown for comparison are the focal mechanism solutions determined from seismology (black beach-balls) and from this model (red beach-ball). Bold black rectangle is the surface projection of the ~10-km-long modeled fault located between ~3.8 and 5.8 km depth. North-south trending white bold dashed line is the up-dip projection of the model fault to the surface which is located about 4 km west of the surface trace of the Dodurga fault (blue lines) as illustrated in the inset box with a vertical cross section. This suggests that if the Dodurga fault ruptured during the earthquake, it must have listric geometry or connects to a master fault at depth that reaches to the surface west of the Dodurga fault as illustrated in the inset box. **b-c**. Residual interferograms obtained by subtracting the synthetic interferogram from the best two interferograms shown in Figure 2.4a and 2.4b. Small residual fringes illustrate that the model successfully predicts the observed interferograms. The remaining fringes are mostly atmospheric noises that are obvious outside the earthquake area.

Corinth event (Jackson *et al.*, 1982). However, no such fault is mapped by Emre *et al.* (2000) or Koçyiğit *et al.* (2001) (Figure 2.2) nor its morphological signature is present in the topography. Even if it exists, the rupture does not seem to reach to the surface because there is no apparent anomaly in any of the interferograms even though signal correlation is low west of the Dodurga fault. On the other hand, the SAR data clearly support the field observations that suggest that the Dodurga fault ruptured during the earthquake (Emre *et al.*, 2000). Reactivation of the Dodurga fault with a small amount of slip is evident by the discontinuity of some fringes across the fault, and particularly by the presence of the cusp in the fringe pattern that cannot be otherwise explained by atmospheric artifacts since it exists in all the interferograms constructed from different orbits. In the absence of additional field observations, it follows that either the Dodurga fault has listric geometry or it cuts a preexisting low-angle surface (e.g. an old thrust plane) that was later reactivated during the earthquake.

In the third stage of modelling, we therefore use two rectangular faults in order to approximate roughly the geometry of a listric fault, one having a steep dip angle and coinciding with the Dodurga fault trace at the surface and the other having a low dip angle at deeper depths. We construct an 83° dipping fault that connects the best fitting fault of 41° dip at depth of ~4 km to the Dodurga fault near the surface (0.5 km). When we keep the fault geometry fixed and invert slip on both faults, inversion deduces a few cm of slip on the steeply dipping upper fault, but with a right-lateral sense, and no significant change compared to the previous single-fault model. This is because the digitized fringe data used in the inversion contain little information about the western side of the Dodurga fault. To overcome this, we fix also the slip on the steep shallow patch and invert all the parameters of the low-angle fault again with a predefined strike at 360°. The parameters of the low-angle fault remains nearly the same compared to the best fit single-fault model (Table 2.1). As shown in Figure 2.8, the resemblance between the model and data becomes remarkable when ~7 cm of left-lateral oblique normal slip is imposed on the shallow fault despite a slight decrease in the goodness of fit in terms of RMS. The cusp in the teardrop feature is now mimicked very well by the model. Near surface faulting on the Dodurga fault also explains disappearing of the fringes west of the Dodurga fault in the southern side of the teardrop feature. In fact, as can be seen particularly from the Figures 2.4a and 2.4b, the first one or two fringes in the south does not continue to the west across the Dodurga fault, which according to our modelling, can be perfectly explained if the rupture is allowed to reach to the surface with a few cm of slip. This is because LOS components of the south westerly horizontal (away from the satellite) and vertical (uplift; towards the satellite) movements on the southwest quadrant of the deformation field of a NS trending, left-lateral strike slip fault cancel each other out, resulting in practically no phase difference. However, we do not think it is worthwhile to complicate the model further by introducing a third or even more patches to obtain a model with a variable slip distribution because the simple two-fault model provides quite a reasonable and satisfactory fit to the observed SAR data set, accounting for large majority of deformation fringes in the interferograms as illustrated by small residual phase in the Figures 2.8b and 2.8c.

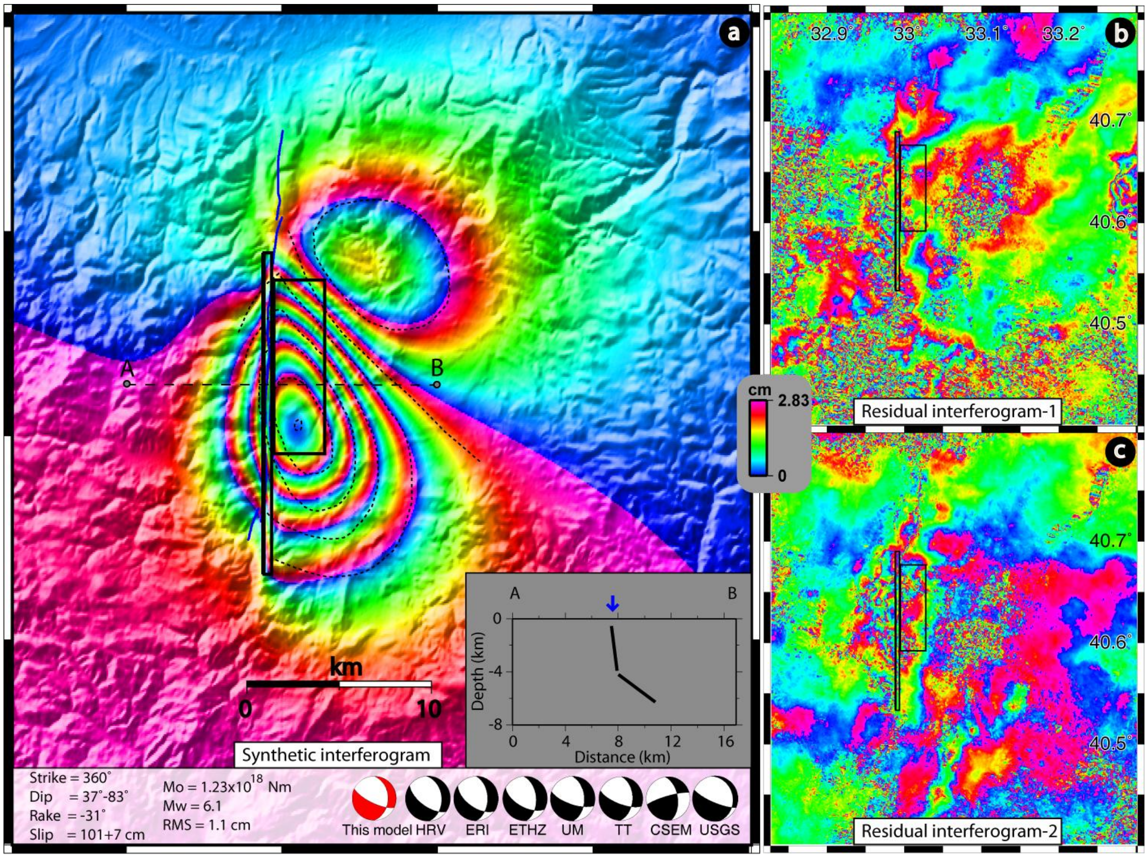

Figure 2.8: a. Synthetic interferogram predicted by the two-fault model, one dipping 83° at shallow depths (0.5-4 km) and the other 37° at deeper depths (4.2-6.2 km). Inset box illustrates the relationship between the two faults in an east-west trending vertical cross section with a blue arrow showing the location of the Dodurga fault trace at surface. The two faults can be considered as a simple representation of a listric fault. See Figure 2.7 for the explanations of other symbols shown. **b-c**. Residual interferograms as in Figure 2.7.

2.5 Discussion and Conclusions

Careful analyses of multiple interferograms and modelling of InSAR data combined with field observations allow us to deduce that the earthquake was associated with a shallow (< 6 km) left-lateral oblique normal displacement that occurred on a north-south striking, eastward dipping, listric fault. When it is not examined carefully as we initially did (Akoğlu and Çakır, 2007), the teardrop feature seems like a single compact lobe composed of closed polygonal fringes. Thus, one would normally expect the surface fault rupture to be located at the edge of this lobe, not crosscutting it. However, as Figure 2.4 shows, the Dodurga fault runs through the teardrop feature. This implies subsidence (i.e. range increase) on either side of the fault, which at a first glance does not make sense, and consequently leads one to think that the Dodurga should not be directly blamed for the earthquake as implicitly suggested by Taymaz *et al.* (2007). As shown in Figure 2.9, subsidence on the footwall block of a normal or oblique-normal fault does occur if the fault has listric geometry and the coseismic slip takes place essentially on its shallow dipping portions at depth. This would not be the case if the fault had planar geometry.

Although with a much higher RMS fit, interferograms may also be explained, to some extent, with right-lateral faulting (Taymaz *et al.*, 2007) and one can reasonably attribute the anomalies in the fringe pattern resulting from near surface slip on the Dodurga fault to atmospheric artifacts. This implies that interpretation of the rupture characteristics of an earthquake based on a single interferogram may thus be misleading because even the determination of the fault mechanism may not be possible with a noisy interferogram, especially when the evidence of surface faulting in the field is not quite clear. It follows that, field observations provide essential piece of information in constraining fault parameters using geodetic data, and that, the use of multiple interferograms, if possible, is necessary to discriminate surface deformation from atmospheric effects (Massonnet and Feigl, 1998).

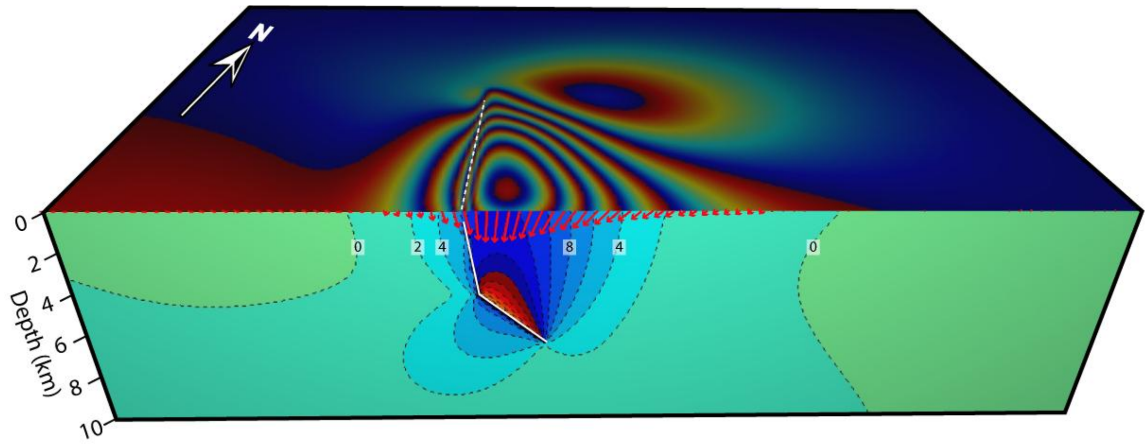

Figure 2.9: 3D perspective view of the interferogram predicted by two-fault model, and the distribution of vertical displacements (with dashed contour lines in cm) on a fault-normal vertical section, constructed using the Poly3D boundary element program (Thomas, 1993). Arrows indicate the direction and the magnitude of the surface displacement resolved on a fault-normal vertical plane.

We have calculated the orientation of the T-axes from all the models with a fault dip ranging between 30 and 70° shown in Figure 2.5. Regardless of the change in fault dip or strike, the models show that the range of the T-axis orientation projected horizontally to the surface is fairly narrow and in the azimuth of N40±7°E (Fig. 2.9). This is consistent with the focal mechanism of earthquakes on the NAF in this region (Taymaz *et al.*, 2007), and with the orientations of the NAF and other faults, suggesting that the Dodurga fault is reactivated under same present-day stress regime that governs the central western section of the NAF (Fig. 2.9). Thus, the Dodurga fault may be considered as part of a relatively wider shear zone due to the restraining bend on this section of the NAF, instead of an evidence for internal deformation of the Anatolian block (e.g. Utkucu *et al.*, 2003) where transpressional deformation causes the development of active thrust faults between NAF and Çerkeş-Kurşunlu valley (Fig. 2.2) (see Figure 2.5 of Hubert-Ferrari *et al.*, 2002).

Faulting depth is well constrained and centered at ~5 km depth, in good agreement with inference of Utkucu *et al.* (2003) and Taymaz *et al.*, (2007). Although faulting took place at such a shallow depth it did not quite reach to the surface, similarly to the 1994-2004 Al Hoceima and 2003 Bam earthquakes (Akoğlu *et al.*, 2006; Fialko *et al.*, 2005). As estimated by Utkucu *et al.*, (2003), the coseismic slip is perhaps too small to reach to the surface. Otherwise, if it is as large as 2.3 m as inferred from waveform inversion by Taymaz *et al.* (2007), the shallow slip deficit can be attributed to the distributed deformation at surface or to layering in the crust (Fialko *et al.*, 2005).

Chapter 3

The 1994-2004 Al Hoceima (Morocco) Earthquake Sequence: Conjugate fault ruptures deduced from InSAR

3.1 Introduction

The city of Al Hoceima and Rif Mountains, located on the Mediterranean coast in northern Morocco (Fig. 3.1), was struck by two strong earthquakes within ten years; first on May 26, 1994 (Mw=6.0) and later on February 24, 2004 (Mw=6.4) (Fig. 3.2). The latter produced severe damage (about 600 deaths and more than 2500 buildings destroyed) in Al Hoceima and the surrounding areas (Ait-Brahim *et al.*, 2004). These two events are the strongest earthquakes in the period of instrumental seismicity to strike the eastern part of the Rif Mountain range, a thrust-and-fold belt within the east-west trending Africa-Eurasia plate boundary in the western Mediterranean (DeMets *et al.*, 1990; Fig. 3.1). The epicenters of the earthquakes are reported to be close to each other and located 15-20 km south west of Al Hoceima (Fig. 3.2). However, the source parameters of these earthquakes are not known in detail because (1) neither of them produced surface ruptures (i.e. both took place on blind faults) (Ait-Brahim *et al.*, 2004; El Alami *et al.*, 1998; Jabour *et al.*, 2004); (2) the absence of obvious morphological features typical of active faults prevents a clear identification of the causative seismogenic faults in the epicentral region; (3) the regional network is too sparse to monitor and precisely locate the seismic activity (Jabour *et al.*, 2004); and (4) aftershocks collected by local networks are complex and distributed (El Alami *et al.*, 1998; Calvert *et al.*, 1997; Dorbath *et al.*, 2005).

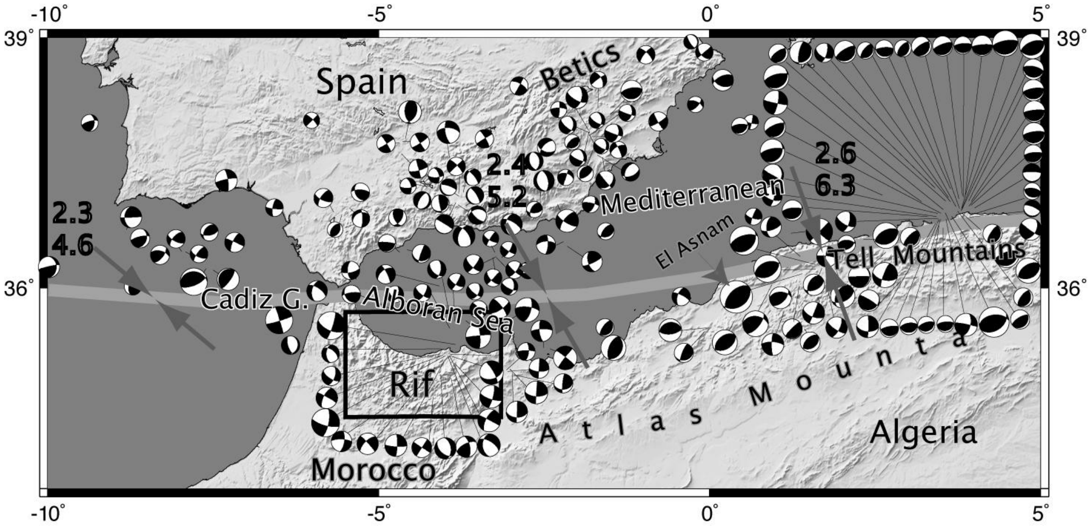

Figure 3.1: Shaded relief map of eastern Mediterranean with focal mechanism solutions of earthquakes between 1951 and 2005 (data from Buforn et al. (2004), Instituto Geografico Nacional and Swiss Seismological Service). Note the change in the type of deformation from Algeria in the east to Gulf of Cadiz in the west along the African-Eurasian plate boundary (thick gray line with arrows illustrating the direction of convergence in mm/yr) (DeMets *et al.*, 1990; Nocquet and Calais, 2004). Black rectangle shows the location of Figure 3.2 in eastern Rif.

Focal mechanism solutions indicate that the two earthquakes are associated with oblique strike-slip faults trending either NE-SW with left-lateral slip or NW-SE with right-lateral slip (Table 3.1). Despite the disagreements in the location and geometry of the coseismic fault ruptures, seismic studies based on aftershock distribution, wave modelling and apparent source time functions imply that the two earthquakes have left-lateral mechanisms (El Alami *et al.*, 1998; Calvert *et al.*, 1997; Dorbath *et al.*, 2005; Bezzeghoud and Buforn, 1999; Buforn *et al.*, 2005; Stich *et al.*, 2005). In contrast to the seismic observations, the recent analysis and modelling of Envisat InSAR data provided by Cakir *et al.* (2006) suggest that the 2004 earthquake took place most likely on a NW-SE trending right-lateral fault. In this previous work, Cakir *et al.* (2006) indicated how the left-lateral solutions for the 2004 earthquake conflict with the InSAR data, whereas the likely model with right-lateral faulting was illustrated and discussed in detail.

Table 3.1: Focal mechanism solutions of the 26 May 1994 and 24 February 2004 Al Hoceima earthquakes. SED: Swiss Seismological Service, HRV: Harvard, IGN: Instituto Geografico Nacional, IAG: Instituto Andaluz de Geofisica, USGS: United States Geological Survey, EMSC: European-Mediterranean Seismological Centre, BB: Bezzeghoud and Buforn (1999), AL: El Alami et al. (1998), InSAR: this study.

	Source	Lon.	Lat.	Depth (km)	Mo (N.m) 10^{18}	Mw	Plane 1			Plane 2		
							Strike	Dip	Rake	Strike	Dip	Rake
2004	SED	-3.997	35.142	12.0	5.18	6.4	115	84	157	208	67	7
	HRV	-3.840	35.270	12.0	3.93	6.3	113	61	-170	18	81	-29
	IGN	-3.997	35.142	6.0	2.70	6.2	107	67	171	200	82	23
	IAG	-4.000	35.140	-	2.88	6.3	107	73	-161	11	72	-17
	USGS	-3.997	35.142	13.0	4.90	6.4	111	89	-176	21	86	-1
	EMSC	-4.000	35.000	29.0	3.60	6.3	128	69	-158	30	69	-23
	InSAR	-3.993	35.127	6-10	6.60	6.5	322	87	-161	231	71	-3
1994	BB	-3.920	35.160	7	1.18	6.0	335	69	2	244	88	178
	USGS	-4.100	35.305	9	0.97	6.0	93	80	-174	2	84	-6
	HRV	3.910	35.370	10	1.01	5.9	112	48	-173	17	85	-7
	AL	3.990	35.280	13	-	-	100	70	157	202	60	23
	EMSC	-4.100	35.305	-	-	-	291	86	-166	200	76	-14
	InSAR	-4.039	35.202	6-10	2.00	6.1	292	84	-170	23	80	-6

In this chapter, we study the two earthquakes of 1994 and 2004, and their relationship using ERS and Envisat SAR data. We model the interferograms of the two earthquakes with a particular attention to the 1994 event using dislocations on triangular faults embedded in a homogenous and elastic half space (Comninou and Dunders, 1975). The availability of ascending and descending interferograms for both earthquakes allows us to constrain their rupture parameters with high confidence. The existence of conjugate faults shed light on the understanding of regional tectonics and related seismic hazard assessment in this region. Finally, we discuss the kinematics of conjugate faults and implications of coseismic strike-slip ruptures within the Africa-Eurasia plate boundary deformation zone.

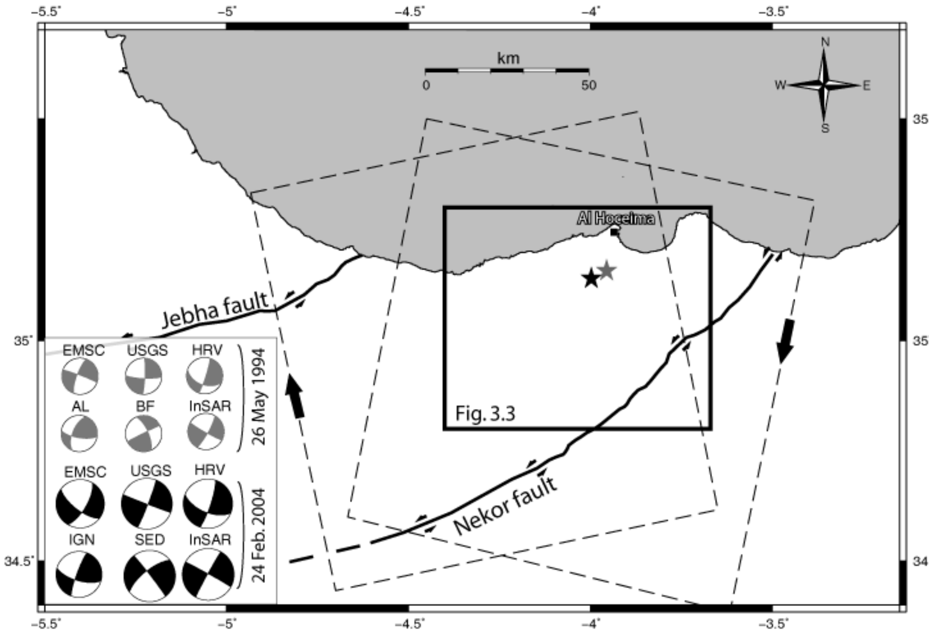

Figure 3.2: Map of the study area showing the ERS/ENVISAT radar frames (dashed rectangles with arrows indicating the satellite flight direction) for ascending and descending orbits. Heavy black lines are major strike-slip faults in the region. Beachballs are focal mechanism solutions of the May 26, 1994 and February 24, 2004 Al Hoceima earthquakes from various sources (gray and black solutions, respectively). The epicenters indicated by stars are from Calvert et al. (1997) and USGS. Black box shows the location of figures 3.3-6.

3.2 Seismotectonic setting

The Rif Cordillera belong to the E-W trending thrust-and-fold system of north Africa that results from the collision between Africa and Eurasia. The system includes the Tell Atlas mountain ranges of Algeria and Tunisia along the Mediterranean coast to the east, and forms a collision tectonics strip along the African-Eurasian plate boundary. Based on the global plate models and GPS observations, the rate of the ongoing shortening between Africa and Eurasia decreases towards the west from 6.3 to 2.3 mm/year from Sicily to northern Morocco (Fig. 3.1) (Nocquet and Calais, 2004). The pattern of active deformation can be interpreted as an anticlockwise rotation of Africa relative to Eurasia with an approximate Euler pole location between 2.1 and 21.0 in latitude and –20.0 and –18.3 in longitude (DeMets *et al.*, 1990; McClusky *et al.*, 2003). Despite the apparent coherent plate rotation in a global scale, the seismicity along the plate boundary is rather complex and varies significantly from west to east (Buforn *et al.*, 2004). The recent seismicity and the 1994-2004 Al Hoceima seismic sequence indicate that the Rif is being deformed under a strike-slip tectonic regime. However, adjacent regions in northern Algeria to the east and the Gulf of Cadiz to the west, are subject to thrust faulting deformation (Grimison and Chen, 1986; Morel and Meghraoui, 1996). Further seismological observations over longer timescales are required to determine if the rate of seismicity along the plate boundary reflects the change in the shortening rate from east to west.

Neotectonic features of the Rif consist of the major Nekor and Jebha, left-lateral strike-slip faults of NE-SW trend (Fig. 3. 2), accompanied by north-south trending normal faults that form a graben-like structure east of Al Hoceima city and a conjugate network of relatively small (10 to 20-km-long) NW-SE and NE-SW strike-slip faults (Fig. 3.3). The transpressive tectonics and existence of a complex fault network with thrust, normal and strike-slip faulting in the Rif probably reflect the rapidly changing local tectonic regime with block rotations during the Neogene and Quaternary (Meghraoui *et al.*, 1996). Although the region exhibited fairly moderate seismicity in the instrumental period before the 1994 earthquake, several strong earthquakes are known to have occurred in the historical times, the largest one being the 1801 event (Jabour *et al.*, 2004; Ramdani *et al.*, 1989). However, further work in the Rif region is required to identify the active and seismogenic faults that can be associated with such large historical seismic events. Microseismic observations suggest that the Nekor fault that once acted as a major continental strike-slip fault until late Miocene (Frizon de Lamotte, 1987), is now probably inactive due to the changes in the regional stress field (Hatzfeld *et al.*, 1993).

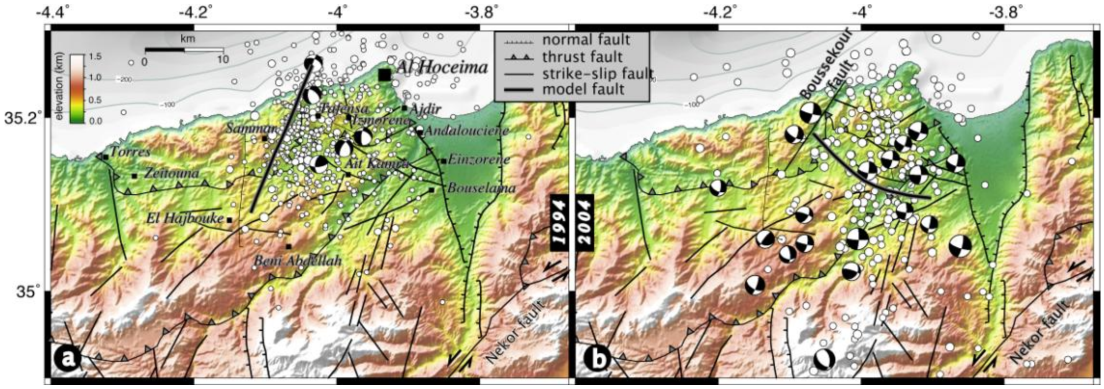

Figure 3.3: Morphotectonic framework of the Al Hoceima region with aftershocks distribution of the 1994 (a) and 2004 (b) earthquakes from El Alami et al. (1998) and IGN (compiled from Calvert et al. (1997), El Alami et al. (1998), and Ait-Brahim et al. (2004)).

Although the mechanism of the 1994 earthquake rupture, based on different observations (i.e. aftershock distribution, macroseismicity, regional tectonics and offshore seismic profiles) made by various investigators, is in agreement with left-lateral faulting, there are inconsistencies in the literature regarding the location and geometry of the rupture. While Calvert *et al.* (1997) infer that the rupture lies between Beni Abdellah and Al Hoceima, El Alami *et al.* (1998) propose a fault of similar trend (N20°-30°E) but shifted of about 6-7 km westward (Fig. 3.3). On the contrary, Bezzeghoud and Buforn (1999) infer a complex rupturing with two sub-events on N5°W and N30°W trending faults in the same region. Similar inconsistencies also exist for the 2004 event: while based on apparent source time functions and seismic wave modelling, Stich et al (2005) and Buforn *et al.* (2005) deduce NNE-SSW trending left-lateral ruptures south of Al Hoceima, Dorbath *et al.* (2005) based on aftershock distribution infer two possible fault ruptures striking NW-SE with right-lateral or/and NE-SW with left-lateral mechanism. The absence of coseismic surface ruptures and the complex tectonic context clearly require adapted methods of investigations to characterize blind or hidden faults.

3.3 Analysis of InSAR data

In order to examine and model the ground deformation associated with the 1994 and 2004 Al Hoceima earthquakes we used European Space Agency's (ESA) ERS and Envisat SAR data, respectively. While the ERS Level-0 (raw) SAR data were processed using the JPL ROI_PAC software (Rosen *et al.*, 2004) , the Envisat Level-1 (single-look) ASAR data were processed using DORIS SAR processing software (Kampes *et al.*, 2003), and precise satellite orbits from Delft University (Scharroo and Visser, 1998). The effect of topography which depends on the perpendicular separation between orbital trajectories is removed from the interferograms using the SRTM 3-arc-second (~90 m) posting digital elevation model (Farr *et al.*, 2007). The interferograms were filtered using a weighted power spectrum technique (Goldstein and Werner, 1998). We obtained a minimum of two coseismic interferograms for each earthquake, one in the ascending and one in the descending imaging geometry of the ERS and Envisat satellites (Table 3.2). Some of the calculated interferograms are shown in Figure 3.4 with wrapped fringes, each representing half a wavelength (i.e. 2.83 cm) range change along the radar line sight. Despite signal decorrelation in the vegetated and cultivated areas away from the coast and in the mountainous region to south, the interferograms reveal quite well the coseismic deformation fields of the earthquakes in the coastal region of Al Hoceima. Part of the 1994 earthquake however appears to be offshore (Fig. 3.4). The number of fringes in the interferograms is naturally proportional to the earthquake size with a maximum peak-to-peak line-of-sight (LOS) displacement of about 11 cm (4 fringes) in the 1994 descending interferogram (Figs. 3.4c,d) and 23 cm (8 fringes) in the 2004 ascending interferogram (Fig. 3.4e). The low coherence in the earthquake area particularly in the 1994 interferograms is likely due to the changes in the reflective properties of the ground during the long-time span (up to 3 years) of the interferometric pairs. Having the shortest temporal baseline (7 months), the 2004 ascending interferogram experienced minimum decorrelation.

Availability of independent interferograms in the descending geometry for both earthquakes allows us to confirm that the overall fringe pattern is the same and thus they

Table 3.2: SAR data used in this study. Interferometric pairs with bold faces are those shown in Figure 3.4. $B_\perp$ perpendicular baseline (m) $\mathbf{H_a}$ altitude of ambiguity (i.e. elevation change required to create one fringe due to topography).

	Orbit	**Orbit-1**	**Date-1**	**Orbit-2**	**Date-2**	**Δ Date**	$\mathbf{B_\perp}$	$\mathbf{H_a}$
1994	**Asc.**	**12399**	**1993-11-28**	**3090**	**1995-11-22**	**724**	**47**	**213**
	“	**12399**	**1993-11-28**	**7599**	**1996-10-02**	**1039**	**28**	**359**
	“	12399	1993-11-28	22763	1995-11-21	723	174	57
	Des.	**11447**	**1993-09-23**	**23314**	**1995-12-30**	**828**	**80**	**125**
	“	**10445**	**1993-07-15**	**3140**	**1995-11-26**	**864**	**96**	**104**
2004	**Asc.**	**9302**	**2003-12-10**	**12308**	**2004-07-07**	**210**	**13**	**773**
	“	9302	2003-12-10	12809	2004-08-11	245	153	65
	Des.	**5845**	**2003-04-13**	**11857**	**2004-06-06**	**420**	**26**	**386**
	“	5845	2003-04-13	13360	2004-09-19	525	194	51
	“	7849	2003-08-31	11857	2004-06-06	280	290	34
	“	6847	2003-06-22	12358	2004-07-11	385	284	35

do not contain any significant atmospheric signal that could potentially be interpreted and hence modeled as surface deformation. The ascending interferograms of each earthquake however share the same pre-earthquake image (Table 3.2) and thus the possibility of atmospheric artifacts in the ascending interferograms cannot be excluded. The fact that the fringes in the 2004 ascending interferogram are smooth and homogeneous suggests that atmospheric artifacts in the earthquake area are absent or negligible. On the contrary, some of the fringes in the 1994 ascending interferograms are discontinuous and clearly disturbed by atmospheric noise. However, the pattern and distribution of the fringes suggest that they are associated most likely with surface deformation rather than atmospheric signal delay. Analysis of the fringes of 1994 earthquake together with the digital elevation model indicates that there is not any significant correlation between the fringes interpreted as surface deformation and topographic elevation, except the northwestern lobe of the ascending interferogram which may partially contain atmospheric phase. Although atmospheric signal correlated with topography should be negligible in the coastal region, it can be significant to the southwest of the earthquake area where high mountains with considerable elevation changes are present in the topography (Fig. 3.3). Indeed, the first fringe along the southern thrust fault in the ascending interferogram of the 2004 earthquake is clearly correlated with topography (Fig. 3.4).

Unlike the Global Positioning System (GPS) that records three components of the coseismic displacement at a benchmark, InSAR records only the component along the line of sight between the satellite and ground point. The line of sight between the point on the ground and the radar satellite in space defines the unit vector. In an East, North, Up coordinate system, the unit vector is +0.39, -0.08, +0.92 for the descending interferogram and -0.41, -0.09, +0.91 for the ascending interferogram, respectively, indicating that the radar is most sensitive to vertical displacements and less sensitive to north-south displacements. Displacements in east-west direction will induce LOS displacement with opposite signs (i.e. range increase or decrease depending on the sense of motion) in descending and ascending interferograms. Consequently, the ascending and descending interferograms of the same earthquake will differ from each other. The difference becomes noteworthy in our case since the surface deformations are related to horizontal displacements on strike-slip faults trending NE-SW or NW-SE at a high angle to the LOS. In some other cases, the overall fringe pattern will remain the same when the fault slip is dominantly vertical (e.g. dip slip faulting, see Amelung and Bell (2003), Talebian *et al.* (2006)), or the pattern will be asymmetric about a N-S axis when the faulting mechanism is mainly horizontal in N-S direction (Funning *et al.*, 2005). In Figure 3. 4, the common lobes between the ascending and descending interferograms with the same sense indicate areas where the ground deformation is mainly vertical (i.e. subsidence or uplift depending on the increase or decrease in range change).

Looking at the shape and distribution of the fringe lobes in the coseismic interferograms of the same type (i.e. ascending or descending) one can immediately infer that the two earthquakes must have taken place on two separate faults of different strike since a rotation of roughly 90° is required to match the orientation of the lobes (Fig. 3.4). This implies that the two earthquakes cannot share a common fault mechanism. From the semicircular shape and distribution of the fringe lobes, it is clear that the 1994 earthquake rupture trends NE-SW in between the two lobes of the ascending interferograms and thus is associated with left-lateral faulting, in agreement with the

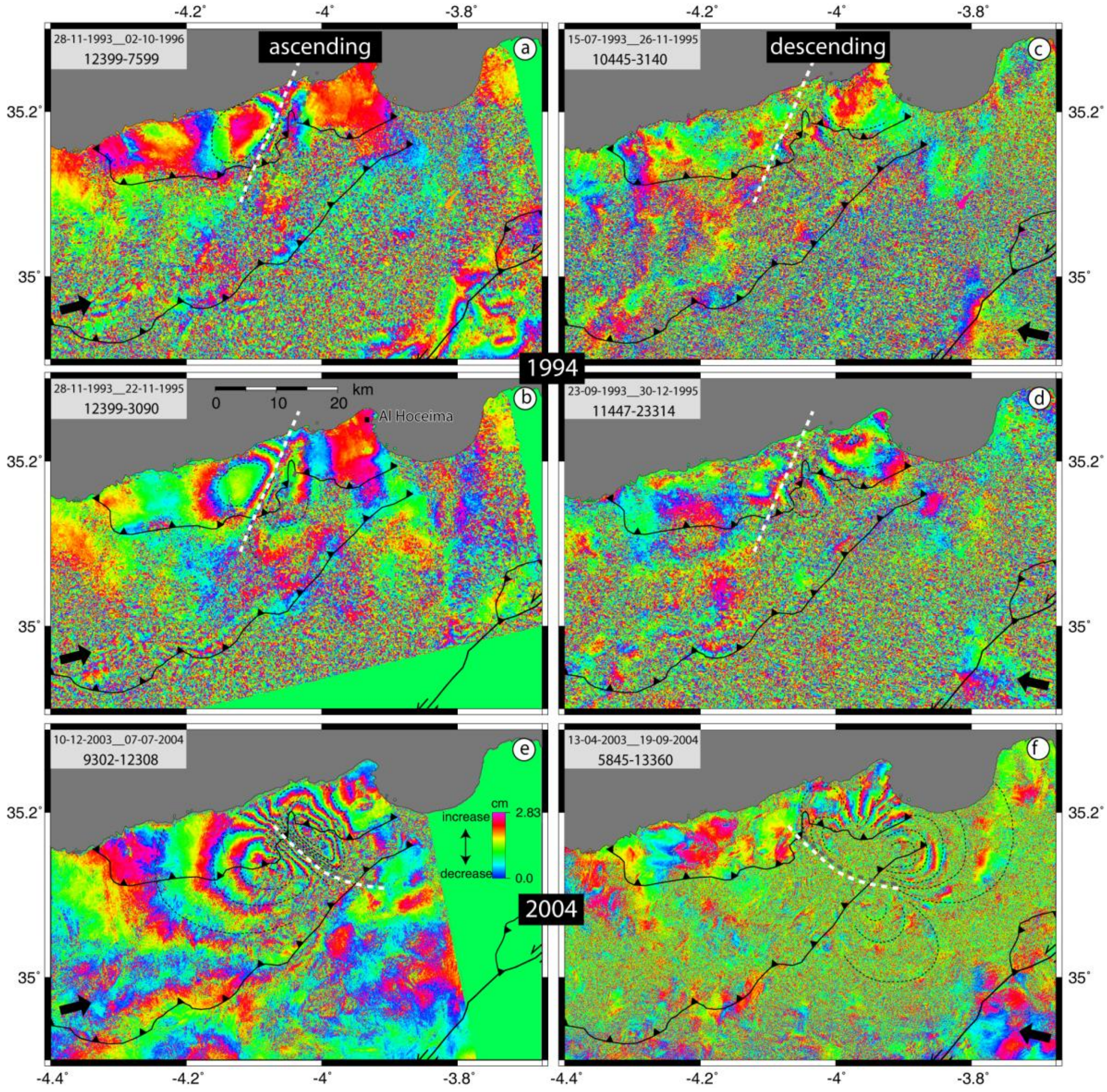

Figure 3.4: Coseismic interferograms of the 1994 (a, b, c, d) and 2004 (e, f) earthquakes in the ascending (a, b, e) and descending (c, d, f) radar geometry with arrows indicating the satellite look direction. Each fringe shows 2.83 cm surface deformation along the radar line of sight. Bold white dashed lines are the surface trace of the modeled fault and the surface projection of the bottom line of the modeled fault (at 16.5 km of depth), respectively. Digitized fringe curves are used to invert the coseismic slip on the modeled fault surfaces. Thrust faults are shown for spatial comparison of fringe patterns in the interferograms.

seismic observations (El Alami *et al.*, 1998; Calvert *et al.*, 1997; Bezzeghoud and Buforn, 1999; Fig. 3.4a). This in turn implies, in contrast with seismic interpretations of Buforn *et al.* (2005) and Stich *et al.* (2005), that the 2004 event is indeed associated with a right-lateral fault trending NW-SE as suggested by Cakir *et al.* (2006; Fig. 3.4e-f). The pattern of fringe lobes and related coseismic displacement fields imply that the two earthquakes took place on blind conjugated strike-slip faults. Indeed, the continuity of fringes across the faults and the location of lobe centers (i.e. zones of maximum deformation) being several km away from the faults, indicate that the 1994 and 2004 coseismic ruptures did not reach the surface and that the significant slip occurred at depth on blind faults rather than at the surface.

3.4 Elastic modelling of the 1994 and 2004 fault ruptures

The analysis of coseismic interferograms provides significant information on the main characteristics and location of the 1994 and 2004 earthquake ruptures. However, to determine the detailed geometry of fault ruptures and related slip distribution we model the interferograms using Poly3Dinv, a 3D-boundary element method that uses triangular dislocations in a linear elastic and homogeneous half-space with a damped least square minimization (Maerten *et al.*, 2005). As shown below, InSAR data require intersection of the two fault ruptures with the 2004 earthquake fault having a non-planar surface. Therefore, we were able to reconstruct realistic 3D fault surfaces with triangular elements using Poly3D (Thomas, 1993), avoiding gaps and overlaps that are otherwise inevitably encountered when modelling curved or segmented faults with rectangular dislocations. This method improves the fit to the geodetic data particularly in the near field when modelling complicated fault ruptures (Maerten *et al.*, 2005; Resor *et al.*, 2005).

Fault surfaces meshed with triangles were constructed using MATLAB®. While the length of the triangular elements is kept approximately the same (1.7-2 km) along the fault, their sizes are gradually increased from 1 km to 3.5 km along the dip direction down to 16.5 km of depth because the resolution of inverted slip decreases with increasing depth. Instead of unwrapped data, digitized fringes are used in the inversion because most of the fringes that are readily visible could not be unwrapped without large errors due to the poor coherence to the south of the earthquake area (Fig. 3.4). The slip distribution on the triangular elements was then inverted with a negativity constraint on the strike-slip component (i.e. left-lateral for the 1994 fault and right-lateral for the 2004 fault). No sign constraints were imposed on the dip-slip component. To avoid unphysical oscillatory slip, the scale-dependent umbrella smoothing operator of Poly3Dinv is applied to inverted slip distribution (with a factor of 0.3 for both earthquakes). Since we use digitized contours of fringes, the smoothing operator with a zero slip constraint on the fault edges, including the topmost patches, also prevents deducing high slip peaks where the inverted data are insufficient or absent (particularly at the fault termination). In addition, a uniform tilting in the data is searched to prevent any orbital errors from biasing the slip estimates.

In order to deduce the fault parameters of the 1994 earthquake we run series of inversions using both left and right lateral faults with varying strike and dip even though all the previous studies (El Alami *et al.*, 1998; Calvert *et al.*, 1997; Bezzeghoud and Buforn, 1999) propose a left lateral fault mechanism (Table 3.3). The best fitting model (model 15 in Table 3.3) predicts a left lateral fault rupture of about 16-km-long running between the town of El Hajbouke in the south to several kilometers offshore (~3 km) near Tafensa in the north. This is in good agreement with the distribution of aftershocks and, supports the inference of El Alami *et al.* (1998) that the causative fault of the event is the Boussekkour fault (Fig. 3.3b). It strikes N23°E and dips towards the southeast at an angle of 77°, in good agreement with the Harvard CMT solution (Table 3.1). Since the modeled fault must not cross cut any visible fringes in the ascending or descending interferograms, the possible range for fault strike is quite narrow (±5°). The dip of the fault is established after a series of inversions with faults dipping from NW to SE (Fig. 3.5, Table 3.3). Our best slip model indicates that slips on the southern part of the fault have largely dip-slip component (i.e. normal faulting) with displacements reaching up to 0.8 m at 4 to 8 km of depth (Fig. 3.6). The dip-slip deduced explains the ground subsidence indicated by the presence of a common lobe between the ascending and descending interferograms, and is consistent with most of the focal mechanism solutions deduced from seismology (Table 3.1). Towards the north, the displacement is mainly strike-slip with similar amplitudes (~0.9 m). It is worthwhile to note that the fault parameters of the earthquake are well constrained owing to the presence of ascending and descending interferograms. Because the surface deformation is imaged from two different positions (i.e. in ascending and descending view), the ambiguity whether the LOS range change is due to vertical or horizontal motion is largely solved (Wright *et al.*, 2004).

We modeled the interferograms of the 2004 earthquake with a curved right-lateral strike-slip fault of about 19 kilometers that dips 87-88° eastward with a strike changing from N85°W in the south, to N38°W in the north (N45°W in average; Fig. 3.7). This fault geometry is the same as that of Cakir *et al.* (2006) except that here, the fault length is shortened for a few km from the northern edge to prevent the intersection with the modeled 1994 earthquake fault. The slip pattern deduced from the inversion shows two asperities separated by a low slip zone around the fault bend (Fig. 3.6). The asperity on the WNW-ESE trending part of the fault to the south releases approximately the 70% of the seismic moment with predominantly strike-slip displacements of up to 2.7 meters at 7 km depth. Located slightly deeper (~9 km) on the fault near the 1994 rupture, the smaller asperity with a maximum slip of 1 m is now better revealed as compared to the previous model of Çakır *et al.* (2006).

The inferred geodetic moments of 2.0×10^{18} Nm (Mw=6.1) and 6.6×10^{18} Nm (Mw 6.5) obtained from the modelling for 1994 and 2004 earthquake ruptures, respectively, are in good agreement with those obtained from seismological observations (Table 3.1). As shown in Figure 3.6, the main features of the observed interferograms of the two earthquakes are successfully reproduced by the best slip models with RMS (root mean square) misfits well below an individual fringe (2.8 cm). The best fit between the modeled and observed interferograms is also revealed from the profiles and residual interferograms (i.e. models minus data) shown in Figures 3.7e and 3.8. Some of the

Table 3.3: Modelling results with varying fault kinematics and geometry.

Model		Length (km)	Depth (km)	Strike (°)	Dip (°)	RMS (cm)			M_o (N m) x 10^{18}	Mw
						ascending	descending	average		
right lateral	1	23	16.5	127	90 ----	1.37	1.14	1.25	2.0	6.1
	2	23	16.5	122	90 ----	1.26	0.96	1.11	1.8	6.1
	3	23	16.5	117	90 ----	1.26	1.13	1.23	1.6	6.0
	4	23	16.5	122	80 NE	1.37	1.45	1.41	1.9	6.1
	5	23	16.5	122	85 NE	1.30	1.17	1.24	1.9	6.1
	6	23	16.5	122	85 SW	1.17	1.00	1.09	1.7	6.1
	7	23	16.5	122	80 SW	1.13	1.06	1.10	1.7	6.1
	8	**23**	16.5	**122**	**75 SW**	**0.82**	**1.23**	**1.03**	**1.3**	**6.0**
	9	23	16.5	122	70 SW	1.04	1.32	1.18	1.4	6.0
left lateral	10	16	16.5	020	90 ----	0.86	0.96	0.91	2.1	6.1
	11	16	16.5	023	90 ----	0.84	0.94	0.89	2.1	6.1
	12	16	16.5	026	90 ----	0.85	0.94	0.89	2.1	6.1
	13	16	16.5	023	85 SE	0.67	0.79	0.73	2.1	6.1
	14	16	16.5	023	80 SE	0.55	0.72	0.64	2.0	6.1
	15	**16**	16.5	**023**	**77 SE**	**0.53**	**0.70**	**0.62**	**2.0**	**6.1**
	16	16	16.5	023	75 SE	0.54	0.69	0.62	2.0	6.1
	17	16	16.5	023	70 SE	0.65	0.72	0.69	2.0	6.1

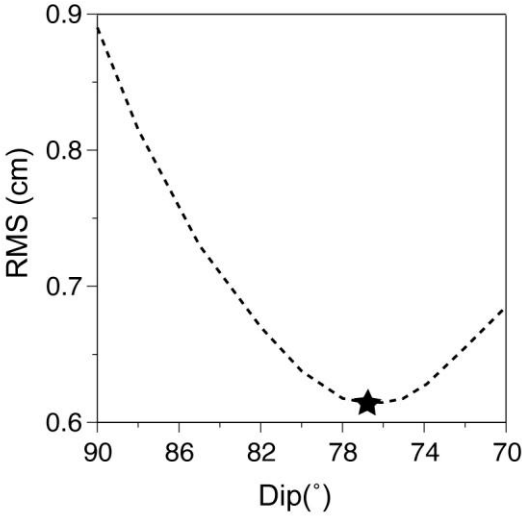

Figure 3.5: RMS misfits plot for the southward dip of the rupture plane for distributed-slip models inverted from InSAR data (both ascending and descending). All the other fault parameters are fixed. Star indicates the best-fit dip which is 77° SE.

remaining fringes in the residual interferograms are most probably due to atmospheric artifacts and unmodeled fault complexity in the near field. For example, part of the phase west of the fault in the 1994 residual ascending interferogram (Fig. 3.8a) is most likely associated with homogenous atmospheric artifacts since there is a clear correlation between the phase and topographic elevation (Fig. 3.8a). Therefore, although small, this interferogram may also contain some homogeneous atmospheric effects.

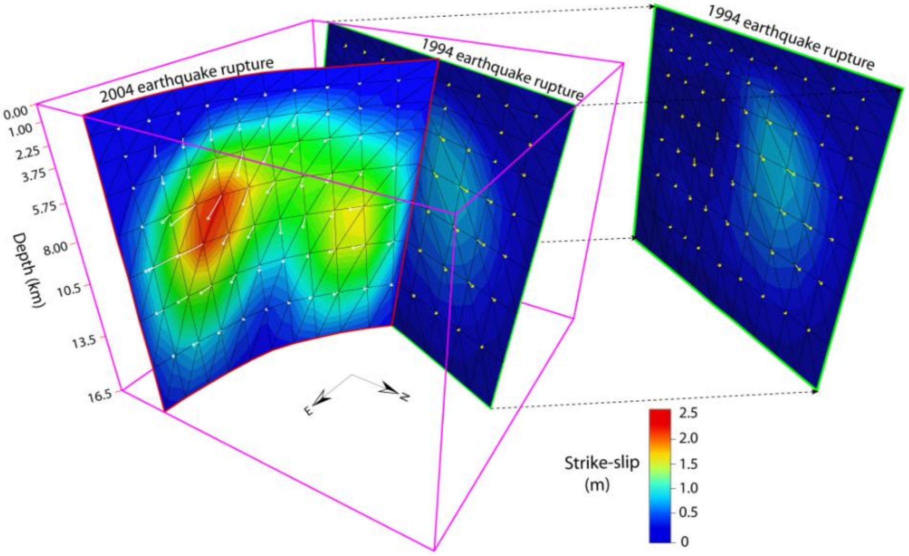

Figure 3.6: 3D view of the best slip models of the 1994 and 2004 earthquakes. Strike and dip components of the coseismic slip on each triangular element are inverted using Poly3Dinv (view towards SW). Color maps of the fault surfaces show interpolated strike-slip distribution with arrows indicating the direction of motion of the eastern block relative to the western one. The intersection between the two fault planes may well be the locus of the 2004 earthquake rupture initiation.

3.5 Discussion and conclusions

The analysis and modelling of InSAR data indicate that the May 26, 1994 (Mw=6.0) and February 24, 2004 (Mw=6.4) earthquake sequence occurred on conjugate strike-slip faults trending approximately N45°W and N23°E (Fig. 3.9a). The acute angle between the conjugate faults is thus roughly 70°, which is 5-10° greater than that expected from Coulomb friction in a homogeneous, unflawed, intact rock which, according to

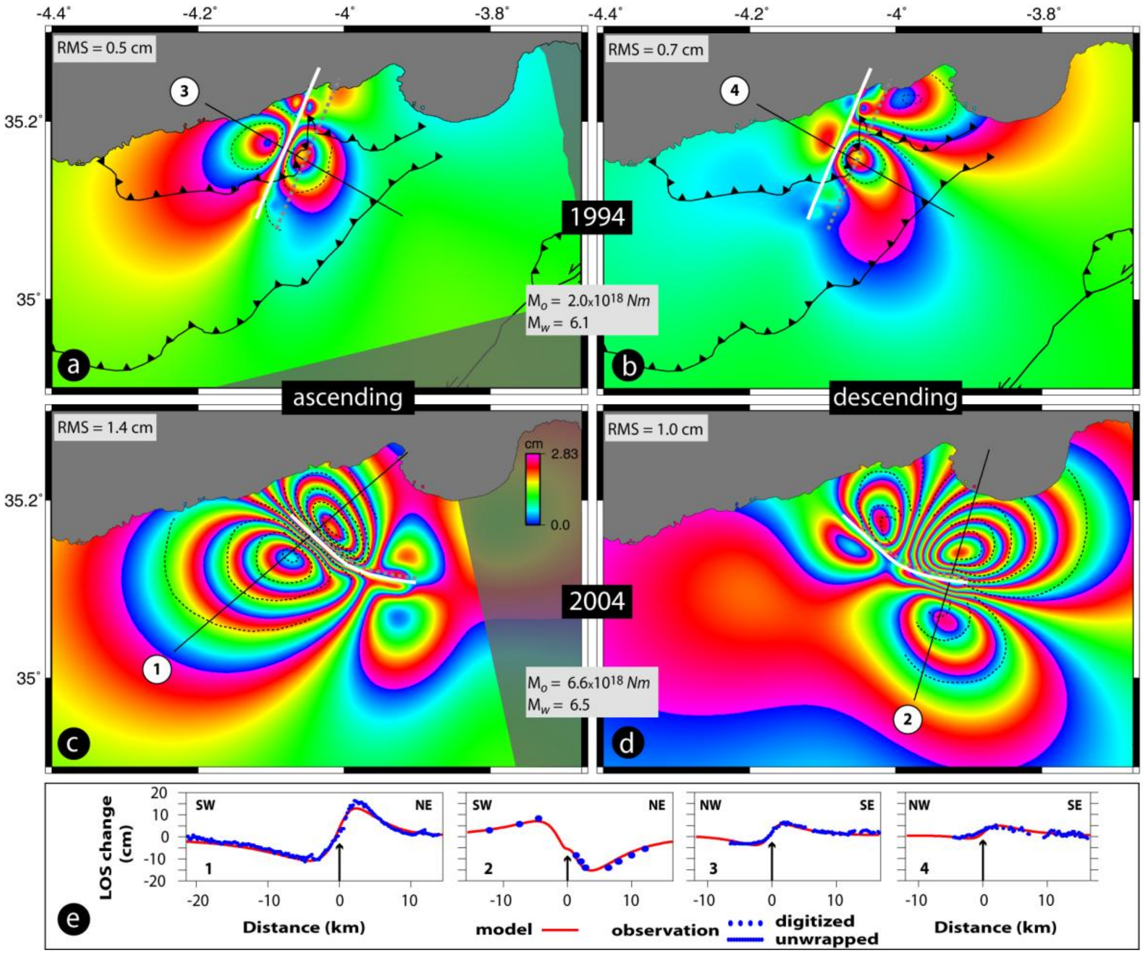

Figure 3.7: Modelled interferograms of 1994 (a, b) and 2004 (e, f) earthquakes obtained from inversion of the observed data (fringe lines). Geodetic moment (Mo) and corresponding moment magnitude (Mw) of each earthquake are consistent with those determined from seismology (Table 3.1). The fit between the data and models is illustrated by line of sight (LOS) profiles (e).

laboratory experiments (Byerlee, 1978), has a coefficient of friction between 0.6 and 0.85. This suggests that either the conjugate faults have low coefficient of friction or at least one of them is a pre-existing rupture plane reactivated under a relatively lower shear stress. Assuming an Anderson-Byerlee fault mechanics (Anderson, 1951) which predicts that the maximum horizontal stress (σ_1) axis bisects the acute angle between the conjugate faults, the direction of σ_1 in the Al Hoceima and Rif region is ~N12°W, in good agreement with N15°-25°W direction determined from seismic tensor inversions

(Medina, 1995) and the orientation of the P-axes of 44 earthquakes that occurred in the region between 1968 and 1994 (Fig. 3.9a). This may seem inconsistent to some extent with the NUVEL-1A plate motion (DeMets *et al.*, 1990) and GPS models (Nocquet and Calais, 2004) that predict a convergent direction of N40°-50°W. These models, however, do not integrate local block tectonics and possible local variations in the stress field along the plate boundary as they are based on large scale observations and sparse GPS measurements. Indeed, the discrepancy between the N40°-50°W convergence and the inferred N12°W horizontal stress s_1 (Fig. 3.9a) can be in agreement if we consider the Rif region as an E-W trending deforming zone between the oblique convergence of the rigid Africa and Eurasia plates (Figure 3.9b). In this transpressive system, the strike-slip partitioning induces a direction of shortening that bisects the angle between plate motion vector and normal to plate margin (Teyssier *et al.*, 1995).

The occurrence of earthquakes on left- and right-lateral strike-slip faults supports the assumption that the Rif is subject to distributed strike-slip deformation (Calvert *et al.*, 1997). Although the modeled fault of the 1994 event coincides with the Boussekkour fault (Fig. 3.3b), the 2004 earthquake took place on an unknown active fault. That the Nekor and Boussekkour faults are sub-parallel to each other implies that the Nekor fault is also optimally oriented in the present day stress field and thus may now be potentially accumulating elastic strain to be released in a future large earthquake. Therefore, the available maps of active faults capable of producing large earthquakes in the Rif should be reevaluated based on new field investigations using improved remote sensing techniques.

That the NW-SE to NE-SW trending faults including the 1994-2004 earthquake ruptures crosscut the thrust faults of the Rif (Fig. 3.3) reflects Quaternary strike-slip tectonics superimposed on Tertiary thrust-and-fold tectonics (Meghraoui *et al.*, 1996). At present the strike-slip regime is probably on its early stages since geomorphological features associated with strike-slip faults are not well developed on the landscape. The focal solutions of earthquakes in the Rif Mountains (Figures 3.2 and 3.3) indicate strike slip mechanisms showing normal faulting component with N15°W $\sigma_1$and N75°E σ_3 in agreement with a transpression tectonic model. Therefore, the conjugate system can be interpreted as fragmentation with slip partitioning affecting the Rif tectonic block associated with a westward tectonic escape in the frame of the Africa-Eurasia (Iberia) collision tectonics (Figure 3.9b; Morel and Meghraoui, 1996).

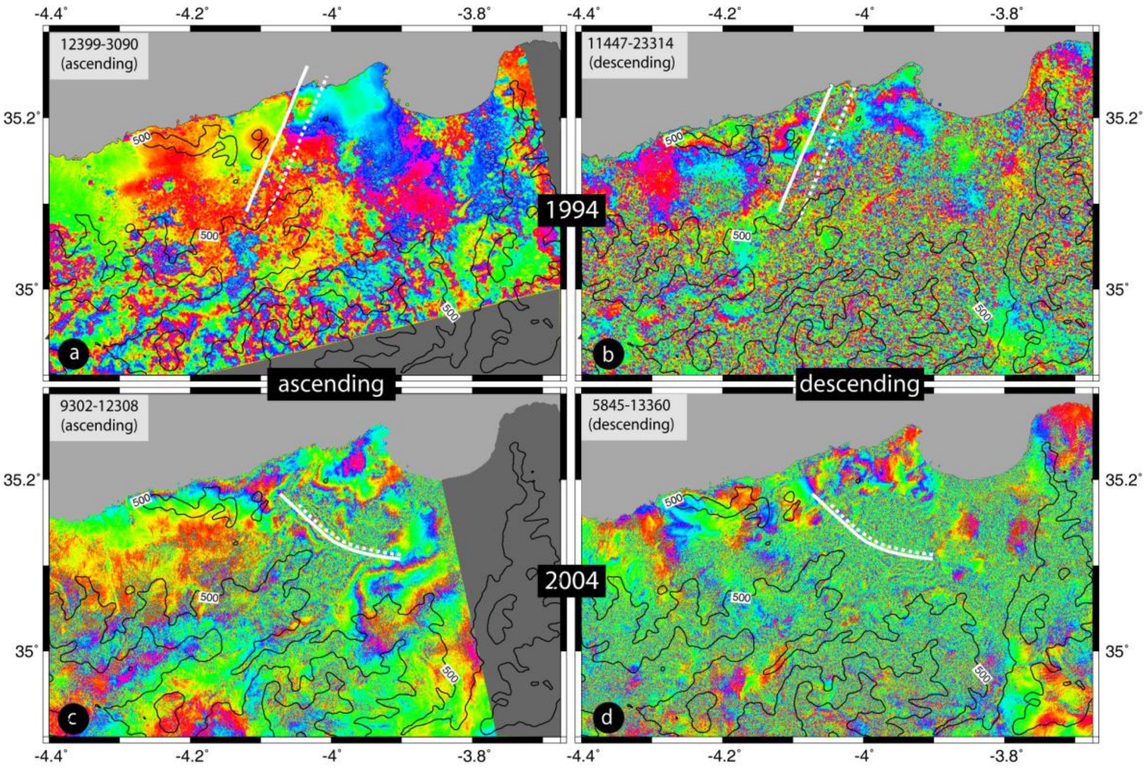

Figure 3.8: Residual interferograms obtained after subtracting the synthetic interferograms (Fig. 3.7) from the observed data (Fig. 3.4). Black lines are topographic contours at every 500 m of elevation.

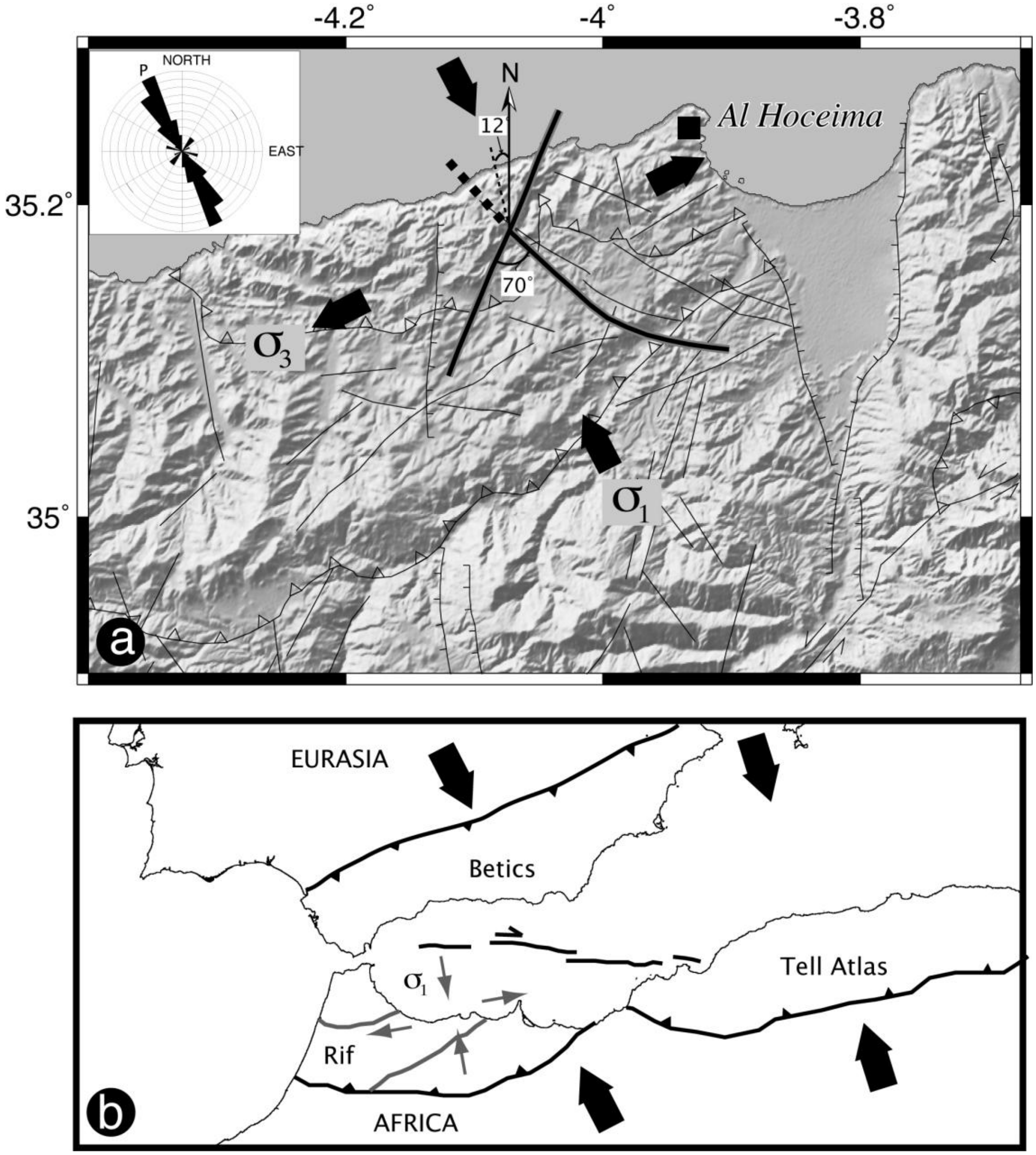

Figure 3.9: (a) Stress field in the Al Hoceima region and block tectonic model associated with Africa-Eurasia (Iberia) plate boundary. Arrows show the direction of the maximum (σ_1) and minimum (σ_3) horizontal stresses based on seismic tensor inversion (from Medina (1995)). Rose diagram shows P-axes orientation of 44 earthquakes that occurred in the region since 1968. (b) Block tectonic model with oblique plate convergence and transpression affecting the Rif, Betics and Tell Atlas Mountains. In this transpressive system, the N15°W shortening in the Rif bisects the angle between plate convergence vector and normal to the deforming zone (Teyssier *et al.*, 1995).

Chapter 4

Creeping along the İsmetpaşa section of the North Anatolian Fault (Western Turkey): Rate and extent from InSAR

4.1 Introduction

While the majority of active faults are locked, accumulating strain over a long period of time and hence producing earthquakes, some faults freely slip at the surface. This slow aseismic slip, called fault creep, may occur at varying scales and rates. In some cases, faults are thought to creep throughout the seismogenic layer at a rate comparable to the geologically determined slip rate and cannot therefore generate large earthquakes (e.g. central San Andreas Fault (Burford and Harsh, 1980; Thatcher, 1979)). In other cases, fault-creep appears to take place within a shallow depth interval and/or at a rate slower than the overall slip rate, and hence does not prevent the fault from producing moderate-to-large size earthquakes (e.g. southern and northern Hayward fault (Lienkaemper and Williams, 1999; Schmidt *et al.*, 2005). Therefore, the rate and extent of fault-creep along strike and depth are key parameters to assess seismic hazard, and to understand faulting behavior and the earthquake cycle (Malservisi *et al.*, 2003; Bilham *et al.*, 2004).

Although creeping along the North Anatolian Fault (NAF) at İsmetpaşa (Fig. 4.1) was discovered over thirty years ago (Ambraseys, 1970), about a decade after the first observation of the phenomenon in the USA (Steinbrugge *et al.*, 1960), little is known about its three dimensional nature. To date, no observations indicative of fault creep at other sites along this section of the NAF have been reported. In this study, we use Synthetic Aperture Radar Interferometry (InSAR) with 10 years of data collected by the

European Space Agency’s ERS satellites to deduce the extent of the creep and its variation along strike in time and space. InSAR can map ground deformation at a high spatial resolution with sub-centimeter precision (Massonnet *et al.*, 1993), and has been successfully used to study fault-creep along the San Andreas, Calaveras and Hayward faults (Bürgmann et al., 1998; Bürgmann *et al.*, 2000; Rosen *et al.*, 1998; Lyons and Sandwell, 2002; Johanson and Burgmann, 2005). The interferograms obtained in this study include atmospheric effects and have generally low coherence due to the vegetation cover and long temporal baselines necessary to monitor long-term surface changes (Wright *et al.*, 2001). Nevertheless, we are able to detect clear signals of the fault-creep and measure its rate all along the fault owing to numerous SAR images used. We model the InSAR data along with the available GPS data (McClusky *et al.*, 2000) using rectangular dislocations in an elastic half-space to determine the depth to which creep occurs. Finally, we discuss the relationship between fault segments, earthquake generation and the fault interactions.

4.2 Creep on the North Anatolian Fault at İsmetpaşa

The North Anatolian Fault is one of the most seismically active structures in the eastern Mediterranean with a slip rate of 22±3 mm/year (McClusky *et al.*, 2000). With the conjugate East Anatolian Fault, it accommodates the westward motion of the Anatolian block relative to Eurasia resulting from the collision between the Arabian and Eurasian plates and the trench pull along the Hellenic subduction zone in the Aegean (Fig. 4.1). A sequence of eight M>7 westward-migrating earthquakes ruptured ~900 km of the North Anatolian Fault from 1939 to 1999, beginning from the Karlıova triple junction in the east, to the Sea of Marmara region, in the west. The creeping section of the NAF at İsmetpasa ruptured with surface breaks twice within 7 years; first in the M=7.3 1944 Bolu-Gerede earthquake and later in the M=6.9 1951 Kurşunlu earthquake (Ambraseys, 1970; Aytun, 1982; Barka, 1996). According to Ambraseys (1970), the Ankara-Zonguldak railway at İsmetpaşa was displaced by about 1.5 m during the 1944 earthquake. In the following 6 years, the fault at same site manifested aseismic surface slip of about 0.3 m before rupturing again during the 1951 earthquake (Ambraseys, 1970). Detailed surface slip distributions of these earthquakes are not known. However, it is thought that part of the ~ 50-km-long low slip section (< 1.5 m) of the 1944 rupture to the east of İsmetpaşa was re-ruptured by the 1951 earthquake (Ambraseys, 1970; Barka, 1996; Pinar, 1953).

Since the observation of an offset wall at the railway station in the town of İsmetpaşa (Fig. 4.2), numerous measurements have been performed to deduce the rate of creep.

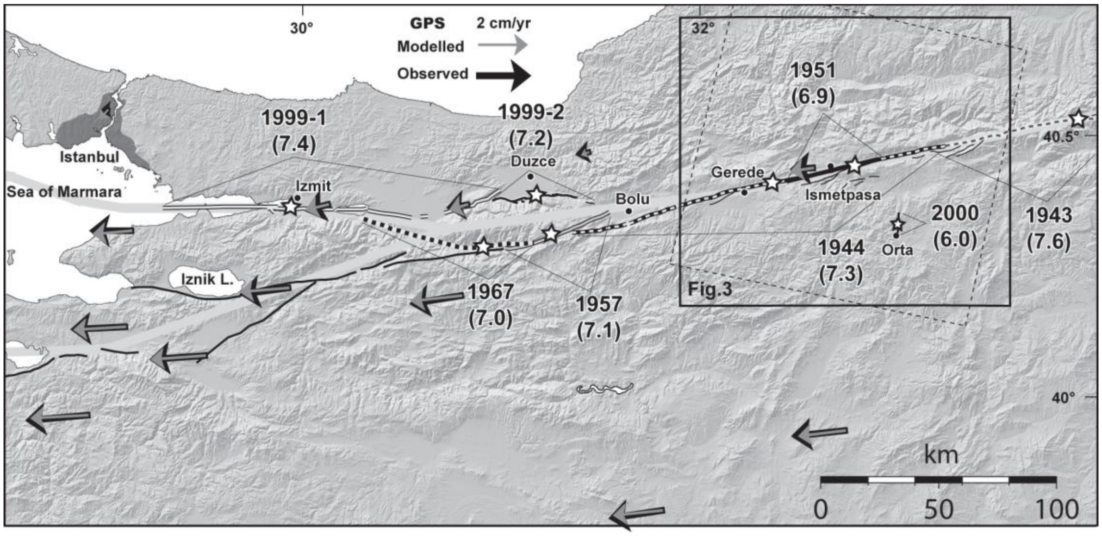

Figure 4.1: Map of the North Anatolian Fault (NAF) in the Sea of Marmara region (Şaroğlu *et al.*, 1992) with the rupture segments of the large earthquakes that occurred in the last century. Arrows are GPS observed and modeled vectors relative to the Eurasian plate (McClusky *et al.*, 2000). The dashed rectangle is the ERS image frame. The inset map shows the schematic plate configurations (Eu=Eurasia, Ar=Arabia, An=Anatolia, EAF=East Anatolian Fault).

Based on the measurement of this wall, Ambraseys (1970) was the first to report a creep rate of about 20 mm/year for the period between 1957 (i.e. construction date of the wall) and 1969. Instrumental measurements (i.e. local triangulation networks and creep-meters) between 1982-1992 at this site have later shown that the creep rate is 7.7±1.1 mm/year (Aytun, 1982; Deniz *et al.*, 1993). Data from another small triangulation network installed about 40 km west of İsmetpaşa in Gerede (Fig. 4.1) indicate that no significant movement was taking place across the fault between 1982 and 1991 (Deniz *et* *al.*, 1993). Therefore, fault-creep ceases to the west somewhere between Gerede and İsmetpaşa. Except for the village of İsmetpaşa, there is no urban site through which the fault runs. Thus, the extent and variation of creep along the fault cannot be deduced without instrumental measurements. Earthquake scaling laws (Amelung and King, 1997), seismicity streaks (Rubin *et al.*, 1999), and repeating microearthquakes (Schmidt *et al.*, 2005; Nadeau and McEvilly, 1999) may help one detect creeping sections of faults, but the present day seismic network is too sparse to study the microseismicity in this region.

Doğan *et al.* (2002) observed some fissures and cracks that show right-lateral slip of up to 6 cm at several new sites around the town of İsmetpaşa after the 1999 Izmit earthquake. They conclude that a creep event was triggered by the distant 1999 Izmit earthquake (Fig. 4.1) as a result of passage of large-amplitude surface waves (Bodin *et al.*, 1994). The effects of nearby earthquakes on a creeping fault have long been known (Allen *et al.*, 1972) and have been confirmed by instrumental measurements such as creepmeters (Lienkaemper *et al.*, 1997; Bokelmann and Kovach, 2003) and InSAR(Bürgmann et al., 2000). Therefore, creep events may also have taken place after the Mw 7.2, Düzce (November 12, 1999) and Mw 6.0, Orta (June 06, 2000) earthquakes. The epicenter of the latter event is very close (~25 km) to the İsmetpaşa fault section and its coseismic fringes can be observed in several interferograms (e.g. Fig. 4.3a). Therefore, using InSAR we also aim to investigate the triggered slip inferred by Dogan *et al.* (2002), and characterize the nature of creep and the effects of the recent nearby earthquakes. We shall later discuss the nature of creep inferred from the previous measurements and this study.

4.3 InSAR observations

We calculated more than 20 interferograms from SAR images acquired in the descending mode of ERS satellites between 1992 and 2002 using the SRTM 3-arcsecond (~ 90m) data for the removal of topographic phase. Of these, only seven interferograms have usable data (Fig. 4.4). One of the main restrictions on obtaining high-quality interferograms is the temporal decorrelation resulting from changes in the target scene due to erosion, vegetation, cultivation, seasonal fluctuation of water content, etc. For example, coherence is completely lost in the north western corner of all the interferograms due to the presence of a forest (Figs. 4.3 and 4.1). The other obstacle for obtaining high-quality interferograms is atmospheric water vapor. Most of the interferograms contain atmospheric effects due to turbulent mixing and stratification. Nevertheless, we were able to obtain useful interferograms with temporal baselines of up to 5 years to detect and measure the amount of aseismic slip (Fig. 4.4).

Figure 4.2: Photographs showing the warped and offset wall (~40 cm) due to fault-creep in the İsmetpaşa train station (September 2004, view towards the north). Note the extension of the wall due to the oblique cross cutting relationship between the wall and the fault in the inset photograph.

The sign of fault-creep in interferograms appears as a step or shift in phase at the surface trace of the fault (Bürgmann et al., 1998; Rosen *et al.*, 1998). In other words, fault-creep gives rise to a discontinuity in phase across the fault if it reaches to the surface. Therefore, the amount of phase shift defines the creeping rate. The uncertainty arises

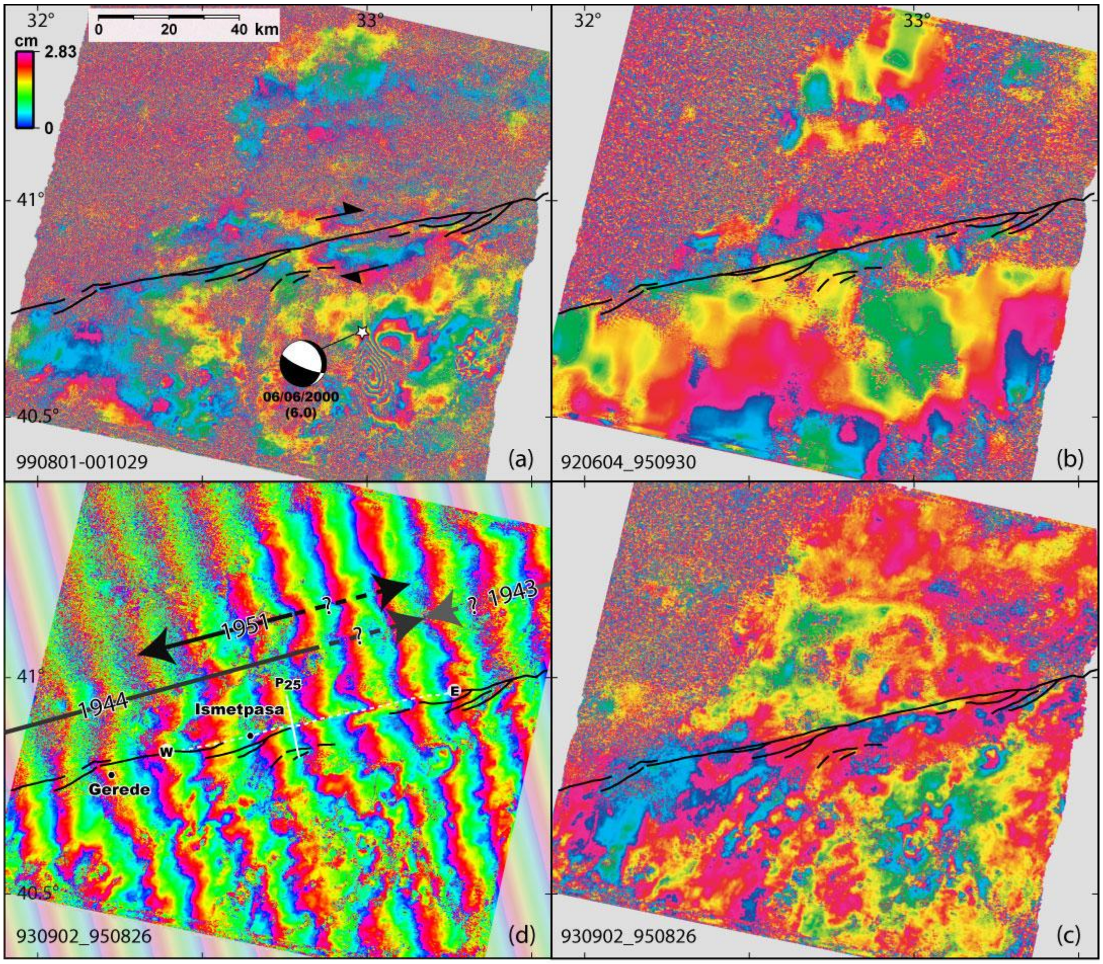

Figure 4.3: **a-c**, Three of the interferograms used to measure the creep rate. Each fringe shows 2.83 cm of phase change along the radar line of sight. Black lines show the North Anatolian Fault zone. Note the concentric coseismic fringes of the 2000 Orta earthquake (focal mechanism from USGS). **d**, Same interferogram as in *c* but, a plane of fringe ramp is added perpendicular to the fault strike in order to better illustrate the discontinuity in phase across the fault as a result of fault creep. The extent of the creeping section of the fault is shown with a white dashed line. One of the profiles (i.e. P_{25}) from which the creep rate was measured is shown with a solid white line.

mainly from errors in phase unwrapping, and in some cases from atmospheric phase correlated with topography (i.e. when there is a significant difference in elevation across the fault). Atmospheric effects due to turbulent mixing are negligible as it is unlikely that such effects can sharply change across the fault. Phase residuals due to errors in the digital elevation model we use to remove the topographic phase, should also be minimal for the same reason. Furthermore, considering a vertical accuracy of 5-10 m for the SRTM 90-m data (Farr, 2004), artifacts remaining from topographic residuals in the interferograms (except interferograms 11145-01335 and 22377-28890) should be less then 1 mm of apparent range change (because the altitude of ambiguity heights of the interferograms are over 500 m). Discontinuity in phase across the fault can be observed in the interferograms shown in Figure 4.3 although they are noisy and contain atmospheric effects. To better illustrate the discontinuity, a plane of fringes running orthogonal to the fault is added to one of the interferograms (Fig. 4.3d). Fringes are clearly offset along ~70 km-long fault section due to the fault creep. Although disturbed by atmospheric effects, bending of some fringes across the fault may also reveal a contribution of interseismic strain accumulation.

Phase profiles extracted from four independent interferograms across the fault east of İsmetpaşa indicate a consistent phase step across the fault (Fig. 4.3d and 4.4b). Since InSAR measurements are in the radar line-of-sight (LOS) reference, we project them into the fault-parallel direction, assuming that surface deformation is purely horizontal strike slip. We then determine the rate of creep between 1992 and 2001 from fault-perpendicular profiles extracted from the interferograms every ~1.5 km along the fault (Fig. 4.4d). These measurements show that fault-creep initiates to the east at the western termination of the 1943 earthquake rupture and continues about 70 km to the west overlapping with the eastern part of the 1944 earthquake fault segment (Fig. 4.3d and 4.4d). The maximum creep rate is 11±3 mm/year approximately in the mid point of the creeping part of the rupture segment diminishing gradually towards the edges. Near İsmetpaşa, InSAR data yield 8±3 mm/year of creep rate, comparable with those deduced from recent instrumental (triangulation) measurements (Deniz *et al.*, 1993) Creep with an average rate of 7 mm/year thus releases 30% of the tectonic loading (22 ± 3 mm/year; McClusky *et al.*, 2000). The error bar of ±3 mm represents the variation of the creep rate from one interferogram to another at the same site (Fig. 4.4d), and the uncertainty in our measurements of creep rates from the profiles. The error will be much larger if there is any vertical motion (i.e. subsidence or uplift) along the fault as we assume the InSAR

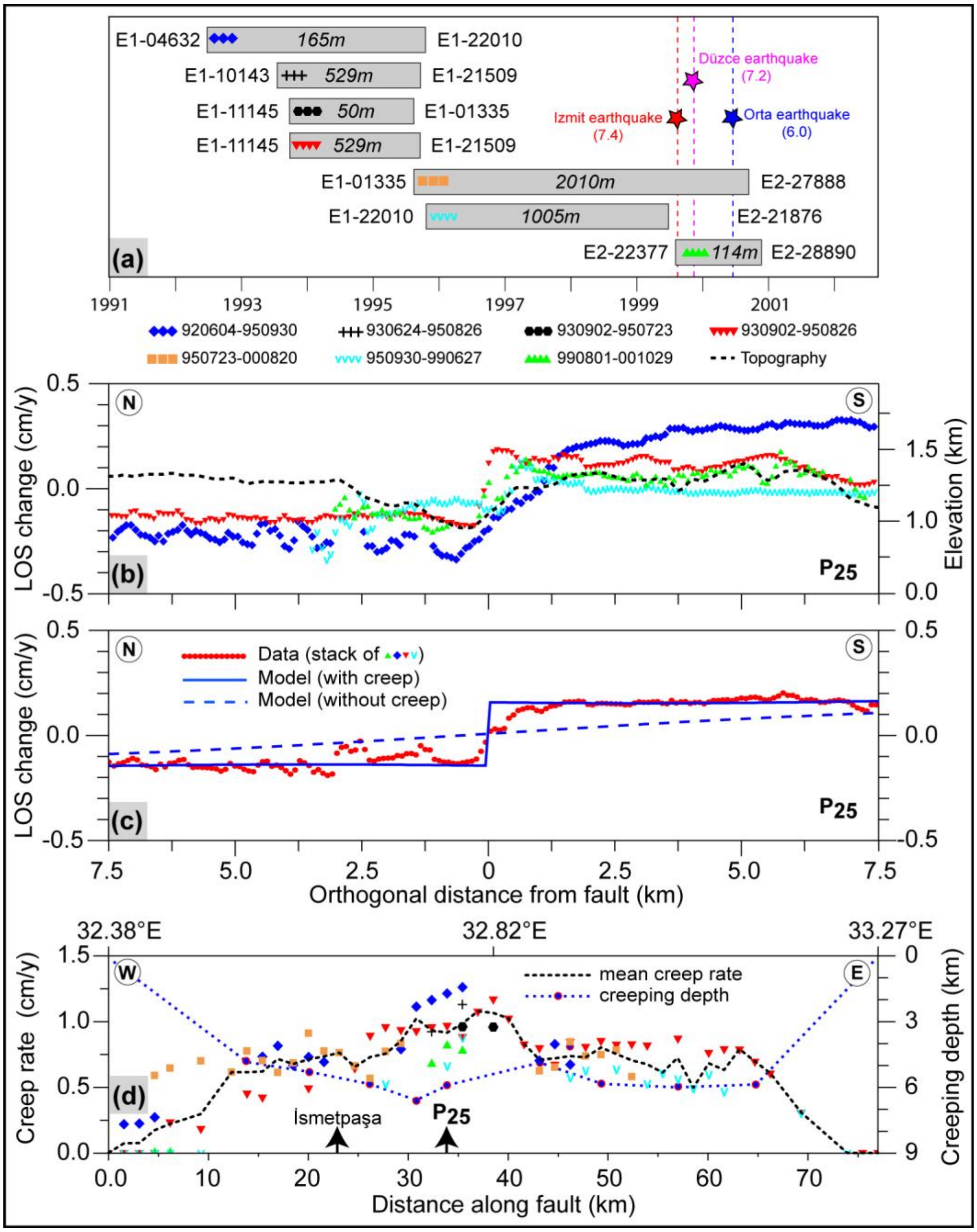

Figure 4.4: a, Interferometric data used (ERS track 479; frame 2781). Bars represent the temporal baselines of the ERS interferograms with their orbit numbers on both sides and the altitude of ambiguity at the centre. A colored pattern is assigned to each interferogram with the exact dates of the images to facilitate comparison of the profiles and measurements shown below. **b**, LOS (line of sight) profiles from four independent interferograms yielding up to 12 mm/year of creep rate (see Fig. 4.3d for profile location - i.e. P_{25}). **c**, Modelling the data obtained after stacking the profiles of different interferograms shown in *b* (creeping depth = 6 km; locking depth = 14 km). **d**, Plot showing the creep rate measured from various interferograms along the fault, and variation of creeping depth obtained from elastic modelling. Locations of the encircled labels W and E are shown in Fig. 4.3d.

signal is due to horizontal motion only. The available data set does not allow us to deduce whether the variation in creep rate is episodic or otherwise time dependent (Roeloffs, 2001) .

We have two interferograms that span the Izmit, Düzce and Orta earthquakes (Fig. 4.4a). Figure 4.4b illustrates that these interferograms do not yield relatively higher creep rates indicative of triggered slip. Triggered slip of 2 cm would be easily observed in the interferogram 22377-28890 spanning two years (Fig. 4.4) since it would double the inferred creep rate. Thus, if triggered slip occurred it must have been superficial and localized at a few points.

4.4 Modelling

In order to deduce the depth extent of the creep, we model the InSAR observations using elastic dislocations in a homogenous elastic half space (Okada, 1985). We assume that a model of uniform slip from surface to some depth characterizes creep along the fault. Regional deformation due to secular loading is modeled by strike slip on buried dislocations below the NAF. However, as shown in Figure 4.5, there is a tradeoff between the creeping depth and locking depth. Therefore, other sources of information (seismicity, GPS, etc.) are necessary to constrain the locking depth of the fault to confidently define the creeping depth (Lyons and Sandwell, 2002). Unfortunately, the GPS and seismic networks are too sparse in this region. Nevertheless, modelling the available GPS data suggests (Fig. 4.1) that the locking depth is somewhere between 10 and 17 km. The InSAR data near İsmetpaşa favor a locking depth of 14 km (Fig. 4.5), consistent with seismic (Özalaybey *et al.*, 2002) and other GPS-based models (Flerit *et al.*, 2003).

To model the InSAR data, interferograms were filtered and then unwrapped. Because the coherent patches vary from one interferogram to another and atmospheric effects and orbital residuals result in phase shifts, we were not able to stack the interferograms. Instead, we stack all the profiles of different interferograms at the same site after removing offsets between the individual profiles. Assuming a locking depth of 14 km and uniform slip, we then invert the resulting profiles using least square minimization (e.g. Fig. 4.4c). The results suggest that creeping occurs down to 6-7 km of the uppermost seismogenic crust (Fig. 4.4d).

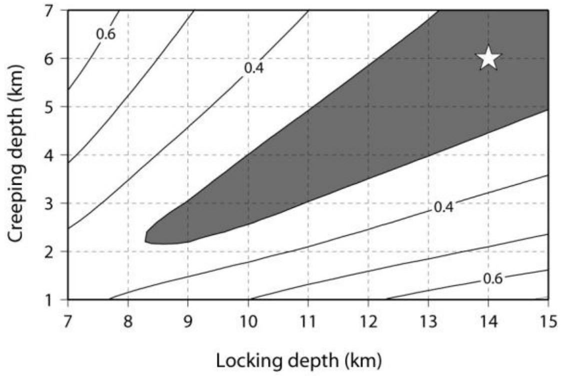

Figure 4.5: RMS misfit (mm) between InSAR observations in Figure 4.4c and models with varying locking depths and creeping depths. Star indicates the minimum misfit model parameters plotted in Figure 4.4c. Shaded areas are minimum misfit plus 5%.

4.5 Discussion and conclusions

It is not known whether or not the fault was creeping before the 1944 earthquake. However, as shown in Figure 4.6, the rate of creep appears to have exponentially decreased with time for the last ~50 years, implying that creeping may have commenced or accelerated after the 1944 event as postseismic deformation, and hence is transient. It is possible that a fast postseismic creep following the earthquake was coupled with a stable background creep, which could give rise to a creep rate higher than the far field velocity (Ben-Zion *et al.*, 1993) as predicted by the exponential function shown in Figure 4.6. If the fault was creeping before the 1944 earthquake, rupturing of the creeping section during these earthquakes would imply that the creeping zone must extend only to a shallow depth and that a strong asperity exists below. Otherwise, the slip deficit that led to the 1951 event could have been taken up at once by the 1944 event.

Modelling of the InSAR data also favors a shallow creep at present. However, as mentioned above, it is difficult to constrain the locking depths from geodetic data alone. There are conflicting results as to the extent of creep on the Hayward fault despite of the intensive studies with wide range of data sets (Malservisi *et al.*, 2003; Bürgmann et al., 2000; Savage and Lisowski, 1993; Simpson *et al.*, 2001).

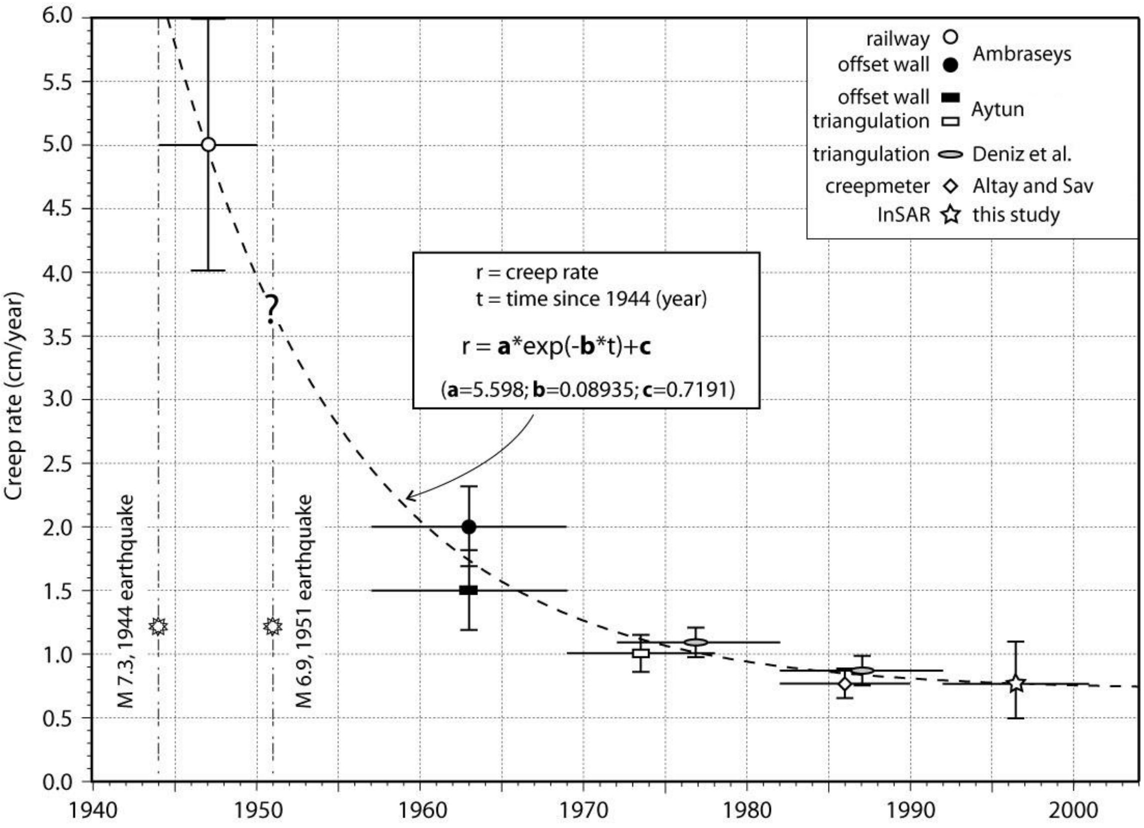

Figure 4.6: Time-history of fault-creep at İsmetpaşa as revealed by various measurements. Horizontal and vertical bars are the time window and error range of the measurements, respectively. Change in the creep rate with time is fitted to an exponential curve (heavy dashed line) using the function in the inset rectangle. The question mark corresponds to the unknown effect of the 1951 earthquake on the creep rate.

InSAR data indicate that creeping initiates around the western termination of the 1943 earthquake rupture (Fig. 4.3d), suggesting that the creeping section arrested the propagation of the 1943 earthquake rupture. Since detailed maps of surface ruptures of the 1943, 1944 and 1951 earthquakes are not available, it is not known if the creeping section was entirely ruptured during the 1944 event or if there was a gap between the 1944 and 1943 ruptures that was later broken by the 1951 event, overlapping with the 1944 rupture. If true, the latter case would explain why the creeping section of the fault at İsmetpaşa ruptured twice within such a short time.

Chapter 5

Coulomb Stress Interactions at the Karlıova Triple Junction: Earthquake Hazard in the Yedisu Seismic Gap along the North Anatolian Fault (Eastern Turkey)

5.1 Introduction

The 20th century was the century of the North Anatolian Fault (NAF); rupturing the Earth crust for more than 10 times, it once again dominated the Anatolian Plate along a zone of about a 1000 km-long from Karlıova in the east to the Saros Gulf in the west. Like domino tiles that topple each other, all the segments of the NAF ruptured during the last century, except the branches in two regions: the portion of NAF under the Marmara Sea and the portion between Erzincan and Elmalı. The latter is known as the Yedisu seismic gap which, according to the historical records, is last broken in 1784 (Ambraseys and Finkel, 1995). Why they did not rupture in the last century and when/how they may rupture in the future are the questions that are currently been investigated by several research groups all along the world.

In this study, we try to seek answers to the Yedisu seismic gap problem by using the Coulomb failure stress (CFS) criterion. It has been 30 years since its foundations are laid and the criterion itself has been applied to various earthquakes during the period. The NAF and its conjugate East Anatolian Fault zone (EAF) have also been study cases during the evolution of the CFS criterion. For example, Stein *et al.* (1997) investigated the aforementioned earthquake sequence along the NAF and Nalbant *et al.* (2002) studied the stress changes along the EAF for the last 200 years. To date, the state and the evolution of stress in the Yedisu seismic gap has not been studied in detail. Therefore, in the present study, taking into account an annual stress loading that results from the plate motions, we calculate stress changes caused by medium-to- large (M > 6) earthquakes that took place around the Karlıova triple junction since 1866 (Table 5.1) and reveal the fault interactions and the stress evolution on the Yedisu fault.

5.2 Tectonic Setting of the Study Area

The study area is located in a tectonically complex region in eastern Turkey where the Eurasian, Arabian and Anatolian plates intersect and interact with each other along the North and East Anatolian faults around the Karlıova triple junction since the continental collision in Early Miocene (Şengör *et al.*, 1985). Westward movement caused by this collision is enhanced when the propagation of the NAF reached to the North Aegean through the Sea of Marmara as a result of the slab pull from the Hellenic subduction zone in southern Aegean (Flerit *et al.*, 2003; Reilinger *et al.*, 2006). The slip rate along the NAF in the study area is about 2 cm/yr, nearly half of the plate velocity in the Aegean (Reilinger *et al.*, 2006). Whereas, the slip rate is about 1 cm/yr on the EAF.

As shown in Figure 5.1, deformation in the Karlıova triple junction is not concentrated only along the NAF or EAF zones but, is distributed. There are numerous short active faults of NE-SW strike with left-lateral sense and NW-SE strike with right-lateral sense parallel to the two major plate bounding faults (Şaroğlu *et al.*, 1992). This observation is supported by the recent seismic activity with small-to-medium sized earthquakes that have taken place on these small faults. Going away from the triple junction, deformation zone along the NAF becomes fairly narrow particularly westward of Yedisu. Therefore, most of the strain due to the Anatolian plate motion is accumulated on the Yedisu fault segment, posing a serious seismic hazard.

5.3 Materials and Methods

To model the stress changes caused by earthquakes and secular loading, we use the method of the Coulomb failure criterion, details of which are explained in Chapter 1. For the calculations, we used the “Coulomb 3” software, a freely available Matlab based code from the United States Geological Survey (Toda *et al.*, 2005; Lin and Stein, 2004). The stress values are calculated at a depth of 8 km in an elastic half-space with uniform isotropic elastic properties (Okada, 1992) and with an apparent coefficient of friction of 0.4. Majority of the events along the NAF appear to occur in the first 20 km of the brittle crust (mostly between 10 and 20 km). However, deeper events (>20 km) are also observed around the Karlıova triple junction and along the EAF (Turkelli *et al.*, 2003). We prefer to extend our modelled faults down to 18 km below the surface and let them reach to the surface if there is any report of field evidence for surface rupture. Due to the nature of a triple junction, there are different types of fault mechanisms in the study area. Both right (NAF) and left (EAF) lateral faulting and their stress interaction with each other should be taken into account. A negative stress change caused by one mechanism may encourage failure on a different mechanism. Therefore, we calculated Coulomb stress changes separately for left- and right-lateral mechanisms. Since we know the kinematics of the faults from their orientation, we calculate the Coulomb stress separately on right and left lateral specified faults instead of calculating it on optimally oriented faults. This also diminishes the necessity to enter a regional stress direction (approximately N-S in the study area).

In order not to plot two maps of Coulomb stress change for the same event, we also applied the concept introduced by Nalbant *et al.* (2002), and display CFS only on surface trace of the faults, which enables us to plot the corresponding CFS values for different fault mechanisms (right-lateral, left-lateral, or thrust) together on the same map. For example, if a fault is right-lateral then, the corresponding calculated right-lateral specified coulomb value over it is plotted.

Another factor we must take into account is the long term tectonic loading which is the yearly stress change caused by the steady state movement of the plates along the major faults (i.e. NAF and EAF). To calculate the long term or secular loading from below, we model the GPS velocity field (McClusky *et al.*, 2003) using elastic dislocations in a homogenous and elastic half space (Okada, 1985) with buried faults below the NAF and EAF from a locking depth of 18 km to great depth (i.e. 150 km) (Fig. 5.2). The yearly stress change value is multiplied with the number of years that passed since the first earthquake (1866 event for this particular study) which yields the corresponding interseismic stress change value. For example, the secular stress that accumulates on the Yedisu segment in 10 years is 1.73 bar.

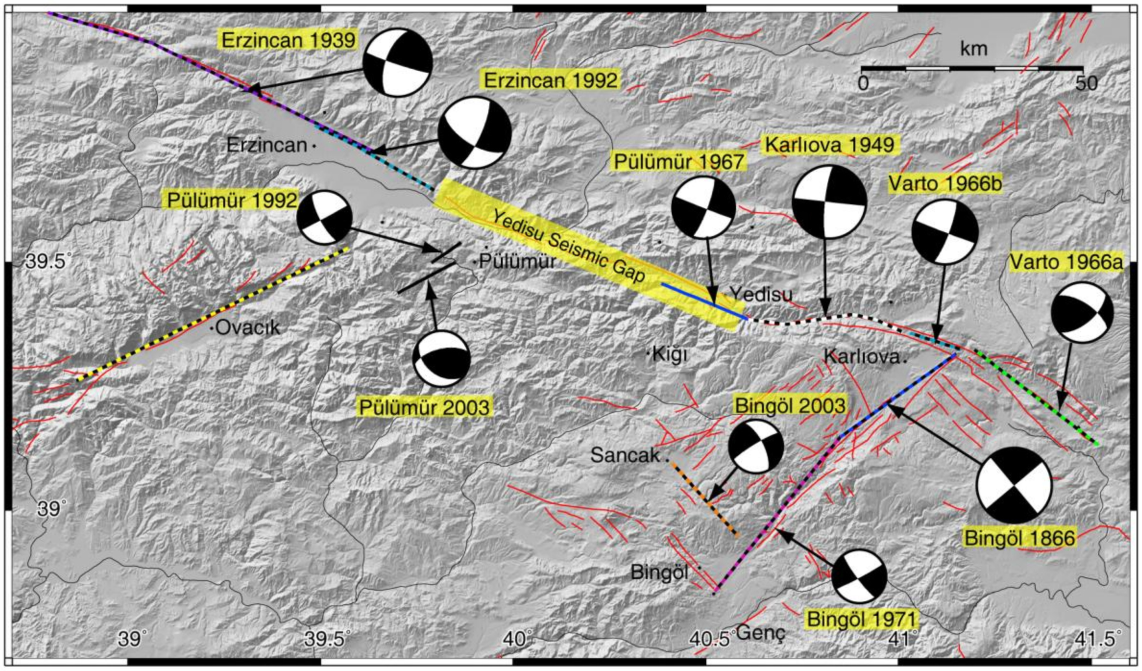

Figure 5.1: Shaded relief image of the Karlıova region from SRTM 90-m-posting digital elevation data. The yellow shaded zone is the Yedisu seismic gap with the blue line showing the likely location of the 1967 Pülümür earthquake. Beach balls depict the focal mechanisms of the earthquakes studied in this work (from McKenzie, 1972; Udias et al., 1989; Eyidoğan et al., 1991 and Harvard CMT catalogue) with dashed lines of various colours showing modelled earthquake ruptures. Red lines are the mapped active faults from Şaroğlu et al. (1992).

5.4 Earthquakes Studied and the Resulting Stress Changes

We include all the earthquakes that had magnitudes greater than 6.0 in the study area. Their locations, surface ruptures and focal mechanisms (except the 1866 event) are given in Table 5.1 and in map view in Figure 5.1. We did not start our calculations with the 1784 Yedisu event due to the lack of sufficient information about it. Neither the location nor the rupture range is known clearly. As the affected region extends from

Table 5.1: Modelled earthquakes (Ms>6) around the Karlıova triple junction and their corresponding parameters used in the calculations. Negative slip values represent left lateral faulting. Rake convention is that of Aki and Richards (1980). See text for the sources of the earthquake parameters.

Date	**Epicenter** (°)		**Mag.** (M_s)	**Depth** (km)	**Fault Length** (km)	**Strike** (°)	**Dip** (°)	**Rake**	**Max. Slip** (cm)	**Event**
12.05.1866	41	39	6.8	0-18	31.98	52	90	0	-100	Bingöl
26.12.1939	39.51	39.80	7.9	0-18	310.4	-67/-86	90	-180	150-650	Erzincan
17.08.1949	40.62	39.57	6.8	0-18	35.4	96/113	90	-180	50-150	Karlıova
19.08.1966a	41.56	39.17	6.8	0-18	34.98	-53	70	150	70	Varto
20.08.1966b	40.98	39.42	6.1	0-18	11.98	106	90	-180	25	Varto
26.07.1967	40.38	39.54	6.0	0-18	20	111	90	-170	15	Pülümür, Kiğı
22.05.1971	40.52	38.83	6.7	0-18	44.98	38	86	-8	-45	Bingöl
13.03.1992	39.63	39.72	6.8	1.5-18	30.16	115/119	63	-164	90-143.3	Erzincan
15.03.1992	39.93	39.53	6.0	1-18	8	-125	61	57	-20	Pülümür
27.01.2003	39.66	39.58	6.1	1-18	14.62	-118	90	0	-20	Pülümür
01.05.2003	40.53	39.04	6.4	1-18	21.98	137	90	-180	40	Bingöl

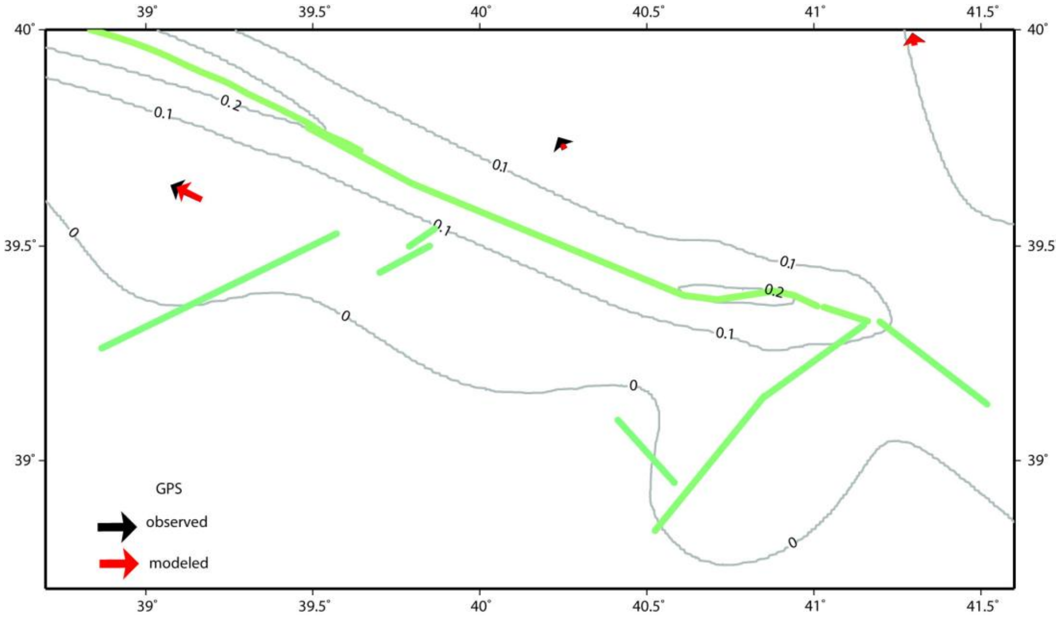

Figure 5.2: Secular Coulomb stress change due to plate loading from below based on modelling GPS data (McClusky et al., 2000).

Erzincan to the districts of Muş (Ambraseys and Finkel, 1995), the earthquake was assumed to have occurred along the NAF between Erzincan and Karlıova. Figure 5.3 shows the Coulomb stress changes due to the each earthquake listed in Table 5.1. As we mentioned above, the static stress changes are mapped on the specified faults of our interest instead of producing classical Coulomb stress maps for right and left-lateral faults separately. Stress changes shown in this figure do not include the secular stress loading in order to provide a clear illustration of the effects of earthquakes on the neighbouring faults.

Our earthquake sequence in this study starts with the 1866 Bingöl earthquake which, surprisingly, was unknown before 1997 (Ambraseys, 1997). Although it was a 19th century event, the causative fault, which is along the left lateral EAF, could be identified owing to a report of an eyewitness; the Russian consul toured the affected region and observed the fault rupture along the Göynük valley. Initial fault length estimation by Ambraseys (1997) is about 45 km. Due to the existence of the 1971 event to the south, we choose a shorter fault of about 31-km-long which corresponds to a magnitude of 6.8 (Wells and Coppersmith, 1994). As shown in Figure 5.3a, the 1866 earthquake increased the stress at the neighbouring faults that rupture later during the 1966 and 1971 earthquakes. It loads the 1971 left-lateral Bingöl and the 1966 right-lateral second Varto events for more than 10 bars. However it decreases the Coulomb stress along the first Varto event of 1966 to the east for nearly the same amount.

After the 1866 event, there is no significant earthquake activity reported in the region until the M=7.9, December 26, 1939 Great Erzincan earthquake, the first event in the westward migrating sequence of earthquakes of the 20th century along the NAF. With a right-lateral displacement of up to 7.5 m, the earthquake produced a surface rupture of about 400 km of long, parts of which are still visible in the field today (Ketin, 1948; Barka, 1996). Figure 5.3b shows the stress change due to the 1939 earthquake. All the neighbouring faults are affected and loaded by this major event. The fault of the future Erzincan event is loaded for more than 5 bars. The earthquake also increased the static stress on the left lateral Pülümür and Ovacık faults.

The Ms=6.8, 1949 Karlıova earthquake occurred along the NAF between Elmalı and Kantarkaya about 10 years after the 1939 event. Ambraseys (1998) estimated 150 cm of maximum right-lateral slip for this earthquake. The Coulomb stress changes following the 1949 Karlıova Event is shown in Figure 5.3c. Its effect on the 19 August 1966 Varto event fault is between 0.5 and 1 bar along the western part. The stress increase reaches to 4 bars on the fault of the second Varto event in 1966. The event increased the stress on the left-lateral 1866 fault up to 3 bars. We also observe a partial stress increase (~1 bar) on the future 1971 fault due to the 1949 earthquake.

The 1949 Karlıova event was followed by the two earthquakes in the Varto region in 1966 (Ambraseys and Zatopek, 1968; Wallace, 1968). As mentioned earlier the first event in 1966 occurred to the east of Karlıova triple junction near Varto. The stress change caused by this earthquake is complex. While the earthquake leads to a stress increase up to 2 bars on the eastern edge of the fault of the second event, it decreases the stress on the rest of the fault for about 0.2 bars. The other fault loaded up to 2 bars by this first shock of the 1966 events is the fault that ruptured during the 1866 earthquake (Fig. 5.3d). The second event of 1966 occurred just west to the triple junction between the 1949 Karlıova and the first Varto event. It increases the stress on the eastern end of the Karlıova rupture zone up to 5 bars.

The 1971 Bingöl earthquake occurred to the south of the 1866 earthquake along the EAF. One particular effect of the 1971 earthquake is the stress drop it caused on the 2003 Bingöl fault. It caused a stress increase of about 0.4 bars on the eastern segments of the Karlıova 1949 fault (between Kızılçubuk and Kantarkaya).

The 1992 earthquake in Erzincan has a strike-slip mechanism with a slight normal component. There is an absence of aftershock activity after the main event east of Tanyeri, indicating a possible decoupling between the 1992 event and the 1784 gap (Fuenzalida, 1997). The event loaded the left-lateral fault of the 1992 Pülümür earthquake (which happened 2 days after the main event) and the parallel Pülümür 2003

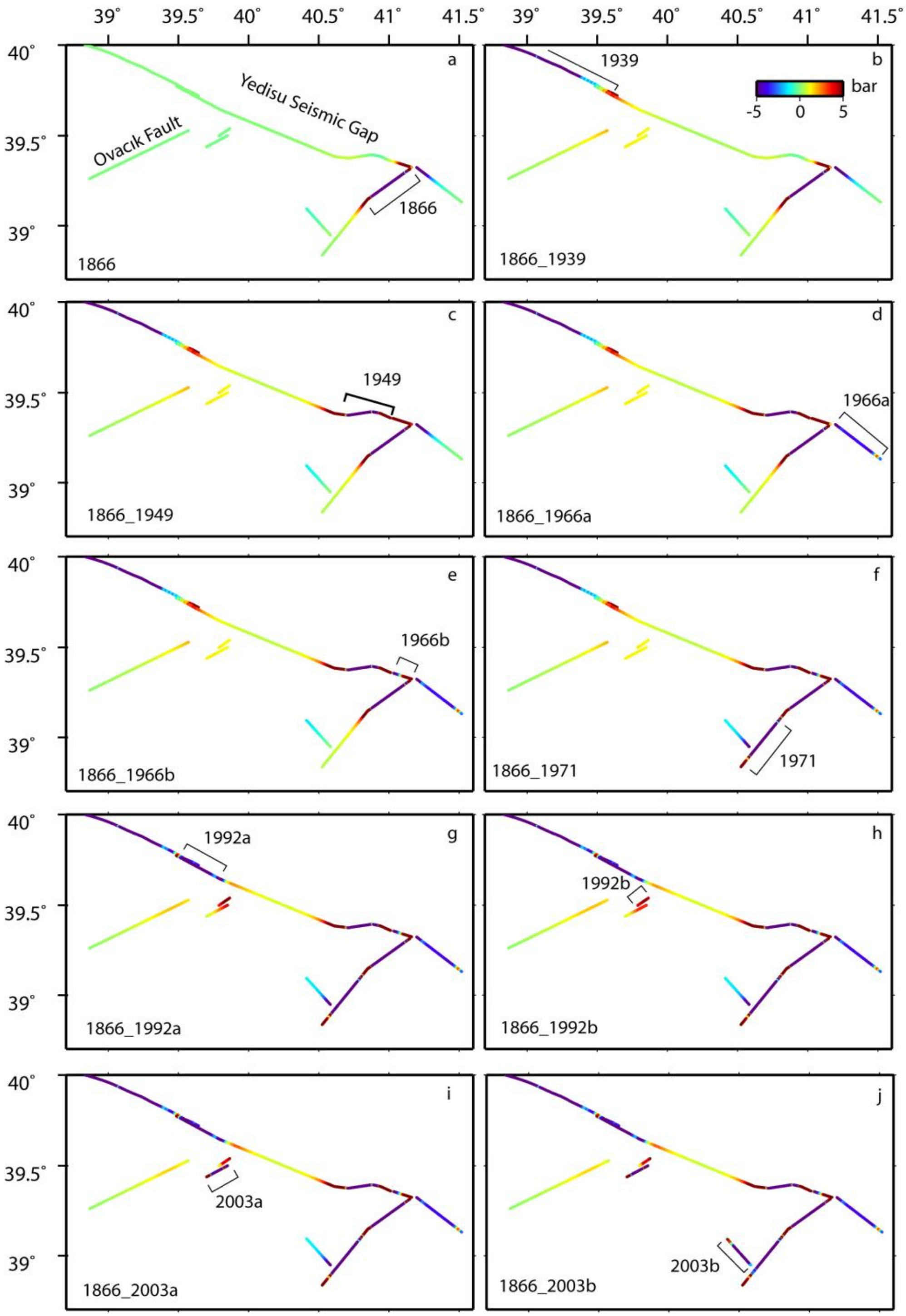

Figure 5.3: Coulomb stress changes mapped on the faults in the study area. In order to better illustrate the static stress changes on the neighbouring faults caused by earthquakes, annual stress loading due to plate motions is not taken in to account in the Coulomb stress calculation for this figure.

fault more than 3 bars. The Pülümür 1992 event itself manages to increase the stress on the 2003 fault up to ~1 bar. However part of the fault also experiences a smaller stress decrease due to the same earthquake.

Two separate events occurred inside our study area during 2003: the Mw 6.1, Pülümür earthquake on January 27th and the Mw 6.4, Bingöl-Sudüğünü earthquake on May 1st. As mentioned earlier, we have tried to analyze both events with InSAR but, cannot accomplish the task due to the gyroscope problem of ERS2. No significant coseismic features observed on land after both events. However the aftershocks clearly define the alignment of the faults (Bekler *et al.*, 2003; Milkereit *et al.*, 2004). The effect of 2003 Pülümür event on Yedisu will be discussed later in the resolved stresses section. It is worth mentioning that it has no effect on the Bingöl event which occurred 5 months later.

In the year 2005, four earthquakes with magnitudes ranging from 5.5 to 5.7 occurred along the 1949 earthquake rupture zone. Since they have not produced any surface ruptures and the seismic network is too poor to accurately determine the epicentres of these earthquakes, it is difficult to infer confidently which fault segment they ruptured. Based on some new field evidence and eye witnesses, Özalp *et al.*, (2005) suggests that the 1949 earthquake occurred most probably on a different segment also because this particular segment is known to have broken during the 1949 event.

The evolution of the stress in time along the NAF between near Reşadiye and Varto (38.5°-41.5°E) is plotted in Figure 5.5. Each line shows the change in static stress after an earthquake with the addition of the effect of tectonic loading. We opt to separate the event graphs into four groups in order to present the stress changes more clearly. As seen in Figure 5.5d, the accumulated static stress on the Yedisu seismic gap since 1866 is in average 30 bars and reaches up to 40 bars to the south.

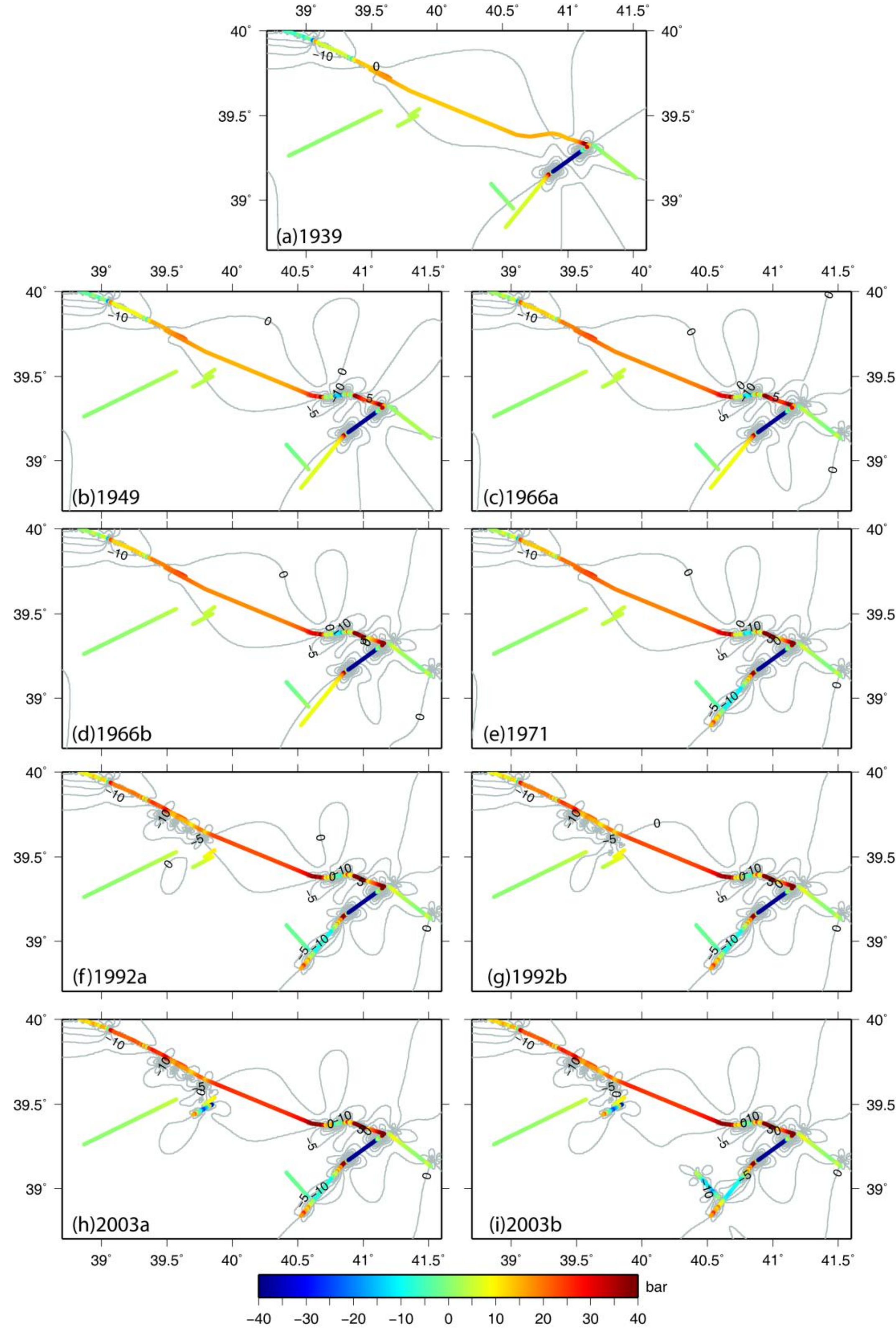

Figure 5.4: Coulomb stress change with the addition of interseismic loading. Contours are at 5 bar intervals.

5.6 Resolved Stress Calculations

In order to illustrate the distribution of the Coulomb stress in two dimensions, stress changes caused by each of the studied earthquakes are resolved and mapped on some specified faults. These are the Yedisu fault, the Ovacık fault, and the Bingöl fault of 2003 event.

5.6.1 Yedisu Fault

We calculated the normal, shear and Coulomb stresses resolved on the Yedisu fault using a 70-km-long and 18-km-wide fault surface parameterized in to rectangular fault patches of 2 km along strike and 2 km down dip (Fig. 5.6). As seen in Figure 5.6b, the 1939 Erzincan earthquake increases the stress only along the western edge of the Yedisu fault. Although the earthquake has a Richter magnitude of 7.9, the stress increase it caused is only 1 bar along a 2-3 km wide zone since the 1939 rupture stopped in the western border of the Erzincan basin far away from the Yedisu area. Whereas, the 1949 earthquake increased the stress up to 8 bars along the eastern edge of the Yedisu fault since they are two connected neighbouring faults. The two smaller events of 1966 and the 1971 Bingöl earthquake did not affect the total resolved stress (Figures 5.6d, e and f). The 1992 Erzincan earthquake that ruptured part of the NAF along the Erzincan basin had a major effect on the Yedisu fault zone. The related stress decrease is over 4 bars and occurred between the depths of 5 and 18 km. In the meantime, over 10 bars of stress increase has been calculated in the upper 5 km of the model fault due to the oblique dextral mechanism of the earthquake.

The aftershock of the Erzincan earthquake also has an effect on the same 15-km-wide zone, dropping the stress up to 2 bars. Nevertheless, since it is a thrust fault, an increase of 1 bar was also observed in a small region. Among the events that took place in the Karlıova region in the year of 2003, only the Pülümür earthquake caused some stress change in the Yedisu area. The event increased the stress on the western half of the seismic gap for about 0.5 bars. The Bingöl earthquake did not have any effect on the area.

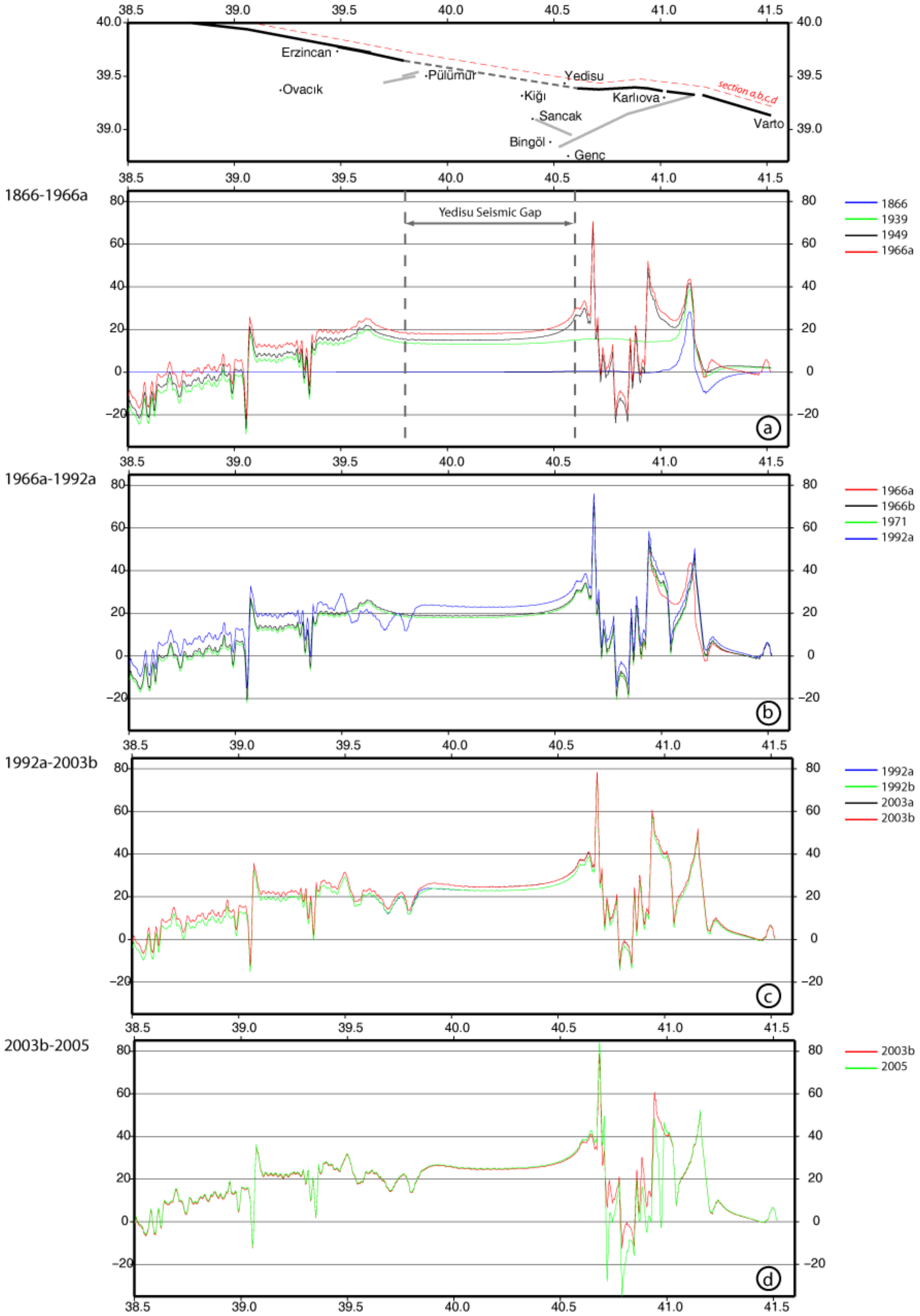

Figure 5.5: Coulomb stress evolution between 1866 and 2005 along the NAF.

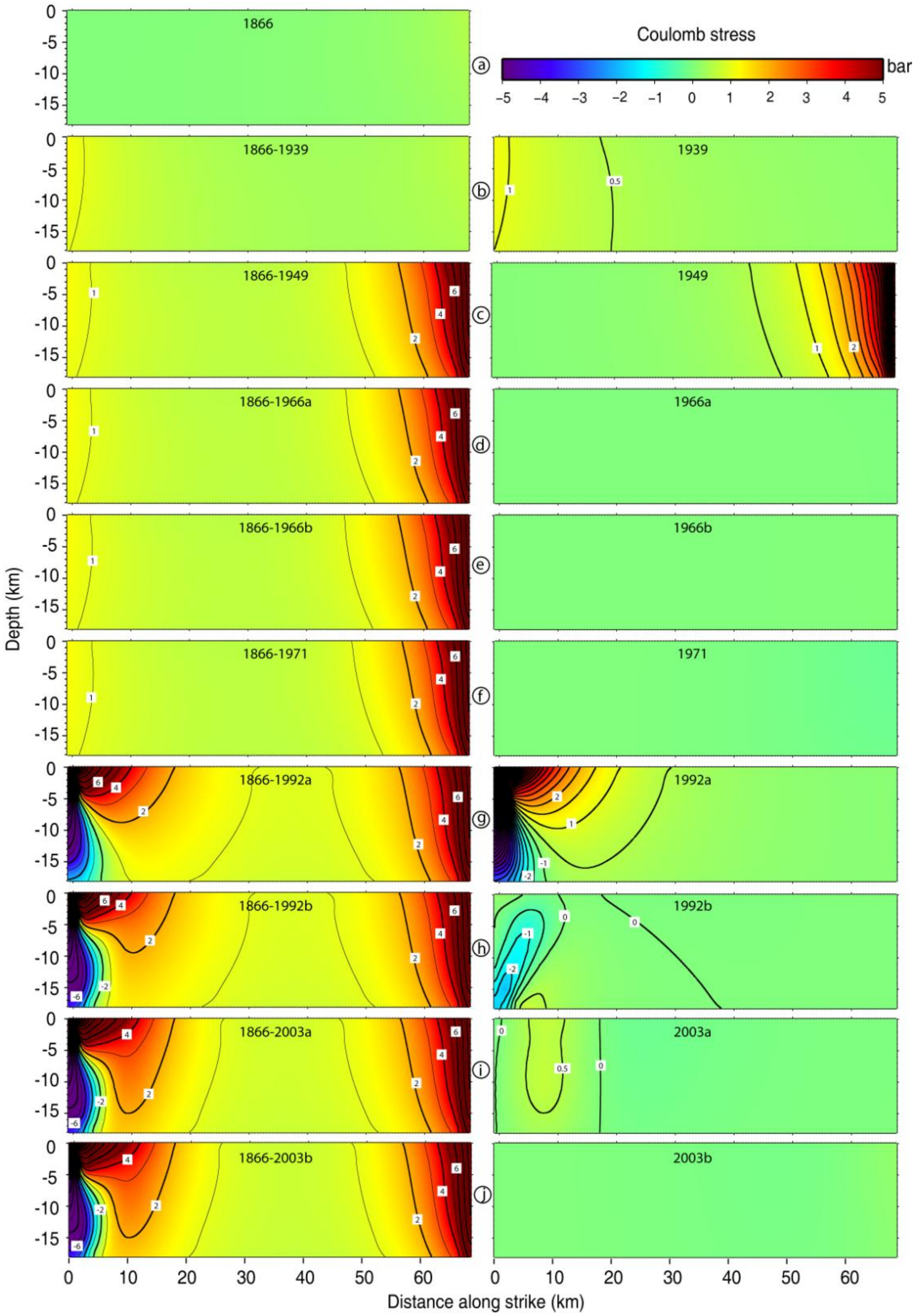

Figure 5.6: Coulomb stress changes resolved on the Yedisu fault segment due the medium-to-large (M>6) earthquakes since 1866. Left column shows the cumulative Coulomb stress change at the Yedisu seismic gap after each event. The right panel shows the effects of each individual earthquake.

The resolved stress calculations show us that only the 1949 and the 1992 earthquakes had significant impacts on the state of stress on the Yedisu seismic gap in the past 150 years. The 1939 Erzincan and the 2003 Pülümür earthquakes also changed the stress positively, but to a lesser amount. The total stress change reaches their maximum values at the two edges of the seismic gap. The accumulated stress change on both ends is over 5 bars. However, the average stress increase along the rest of the Yedisu zone is around 1 to 2 bars.

5.6.3 Ovacık Fault

The Ovacık fault is a 240-km-long, left-lateral strike-slip fault parallel to the EAF. So far, there is no historical report found that indicates any seismic activity along the Ovacık fault at least for the past one thousand years. We also calculated the resolved stresses on this fault even though it is thought by some researchers (e.g. Westaway and Arger, 2001) as a non-active fault. The distribution of the total stress accumulated since 1866 is shown in Figure 5.7. The 1939 Erzincan earthquake is the most significant event for the Ovacık fault that lead to an increase of 2.5 bars. The other event that affected the Ovacık fault is the 1992 Erzincan earthquake with 0.5 bars of stress increase. The left lateral 2003 Pülümür earthquake is the last to change the state of stress on this fault; it caused a 0.5 bar stress drop on the northern edge of the Ovacık fault. As shown in Figure 5.7, failure on the Ovacık fault is promoted by the earthquake on the neighbouring fault segments with an overall stress increase of about 1.5-2 bars. Therefore, it is most probable that the stress accumulated on this fault will be released by future earthquakes since it is optimally oriented in the present stress regime.

5.6.4 The 2003 Bingöl earthquake

The 2003 Bingöl earthquake occurred along a right-lateral fault that has a strike of NW-SE, diagonal to the 1971 Bingöl earthquake rupture on the EAF. Similar to the 2003 Pülümür earthquake rupture, it was not identified as an active fault before the event. To

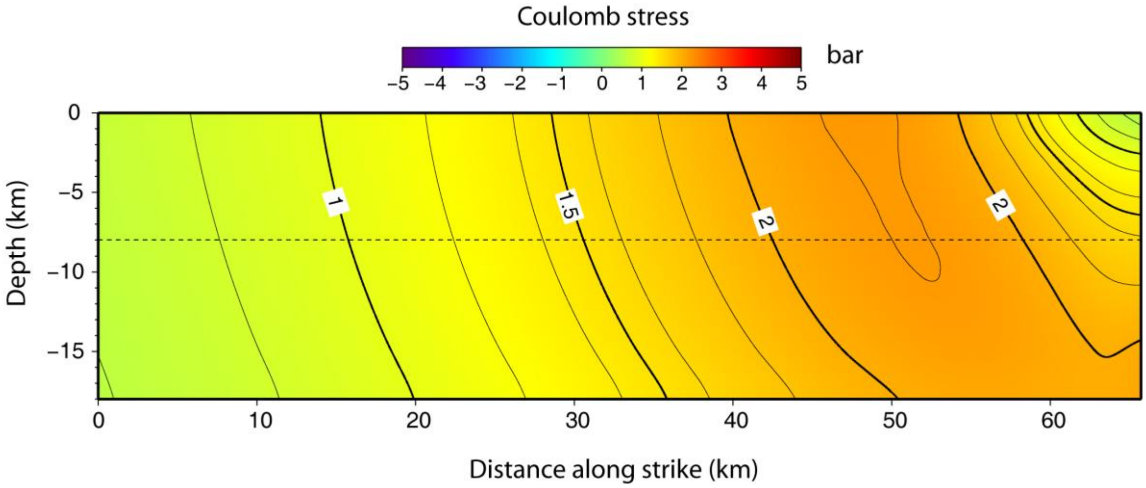

Figure 5.7: Stress change along the Ovacık Fault. The dashed horizontal line at 8 km represents the depth at which the Coulomb stresses in Figure 5.3 are calculated and mapped.

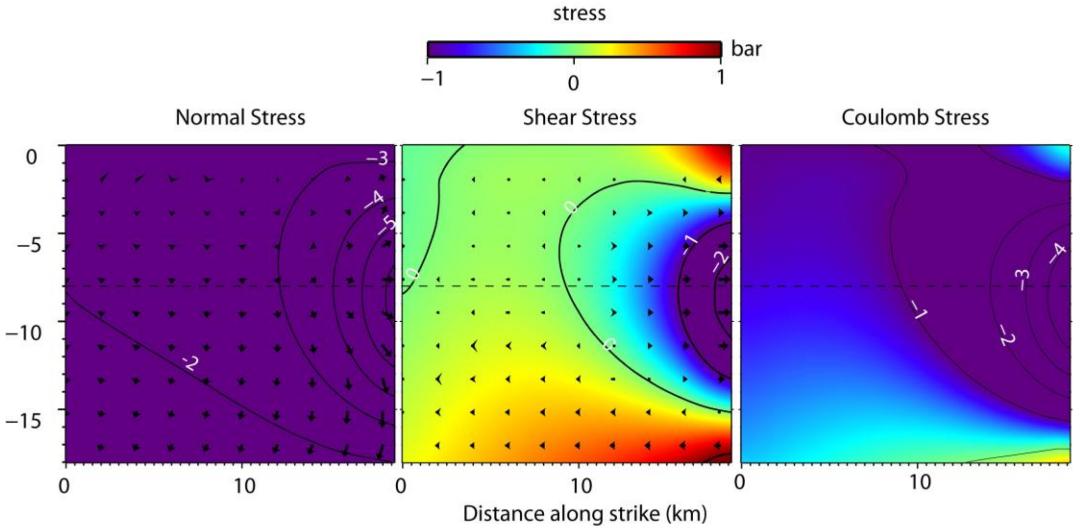

Figure 5.8: Stress change on the 2003 Bingöl earthquake rupture surface caused by the previous events. Left panel shows the resolved normal stress which is negative. The dashed horizontal line at 8 km represents the depth at which the Coulomb stresses in Figure 5.3 are calculated and mapped. Arrows illustrate the maximum shear stress (left panel) and the lateral shear stress (middle panel) indicating that the previous earthquakes promoted left-lateral slip (arrows pointing to the right), which is why the Coulomb stress (right panel is mostly negative since this fault is right-lateral.

calculate stress changes on this fault, we constructed a fault plane using again 2x2 km sized rectangular sub-patches. Calculation of the stress changes resolved on these small fault patches reveals that the previous earthquakes did not promoted failure on the fault. On the contrary, they gave rise to clamping effects with a Coulomb stress decrease of about 4 bars and thus inhibit the failure on this fault. In other words, the 2003 Bingöl earthquake appears to have taken place on a stress shadow. However, there is a small region with 0.1 bar stress increase on the lower eastern corner of the fault at a depth of about 17 km. The earthquake might have been nucleated there and ruptured a small portion of the fault at its bottom since the earthquake rupture did not reach to the surface. Otherwise, similar to the 1992 Landers and 2000 Hector Mine earthquake sequence (Freed *et al.*, 2007), occurrence of the 2003 earthquake can be explained by postseismic effects of the previous as already suggested by Nalbant *et al.* (2005).

5.7 Earthquakes in the Last Four Years

In 2005, four small to medium sized earthquakes (5.5-5.8) took place along the NAF where the 1949 earthquake occurred (Figure 5.9). As shown in Figure 5.10, plotting the locations of these and other accompanied events on the map of Coulomb stress changes caused by the previous events between 1866 and 2003 indicates that the Coulomb stress criterion fails to explain their occurrence because they are located in the stress shadows, that is, in regions with negative Coulomb stress (i.e. blue areas). The stress shadow is in fact caused by the 1949 Karlıova earthquake. This can also be easily observed from the Figure 5.5 in which the stress evolution along the NAF is shown. Our modelling results show that these four earthquakes may raise the stress along Yedisu for a maximum of 0.6 bars (Fig. 5.5). However the affected area is shorter than 5 km at the eastern edge of our model grid fault.

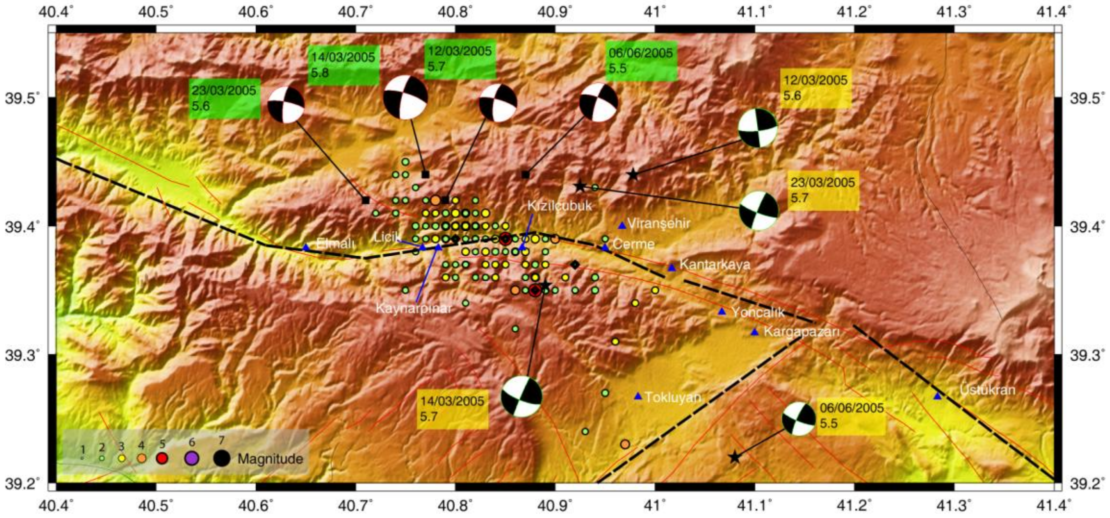

Figure 5.9: Seismicity in the region between 12 and 16 March 2005. Yellow and green focal mechanism solutions are from USGS and Harvard, respectively. Epicenters of the events are from Kandilli observatory. The dashed black lines show our model faults that are used in the Coulomb stress calculations to represent the previous events.

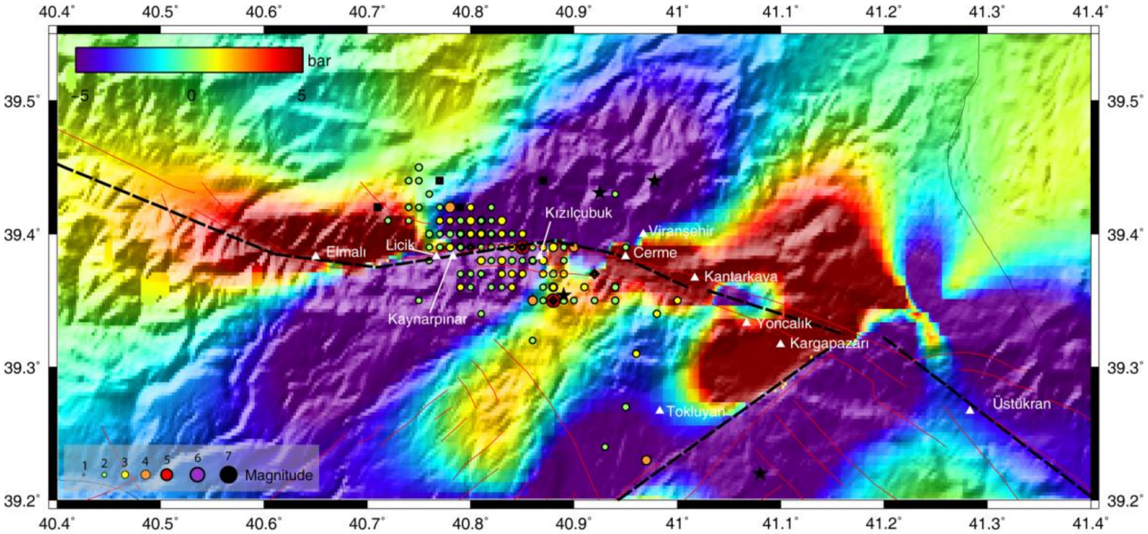

Figure 5.10: Seismicity in the region between 12 and 16 March 2005 plotted over the map of Coulomb stress changes caused by the neighboring earthquakes since 1866. Note that the seismic activity is in general located in areas of negative stress changes (blue areas).

5.8 Discussion and Conclusions

We have investigated the triggering of events in the Karlıova triple junction since 1866. Stress change calculations show that 6 earthquakes can be explained by Coulomb failure stress approach. The 2003 Bingöl, the 1966 first Varto and the smaller earthquakes of the year 2005 are located where the Coulomb stress is particularly negative or does not implicate failure. This may be due to the fact that we consider only elastic stress changes throughout the study; the effect of time dependent processes like viscoelastic relaxation can provide a plausible explanation to these events and must be investigated in future research.

Resolved stress calculations along the Yedisu segment show that a potential risk is imminent as predicted. However, before making any seismic hazard estimation, the length of the Yedisu fault needs to be established. The fault shown in Figure 5.1 (yellow shaded zone) and Figure 5.6 represents the maximum length of the Yedisu seismic gap, which is about 70 km, and even 80 km (Akyüz, personal communication). Taking into account the accumulated slip of about 5 m since the last event in 1784 with a 2 cm/yr rate from GPS, a fault length of 70 km implies an earthquake of magnitude (Mw) 7.23 (or even 7.29 for 80 km) based on fault scaling laws derived from statistical observations (Wells and Coppersmith, 1994). The size of the seismic gap however can be much smaller depending on the location of the 1967 earthquake (M=6.0). If, as suggested by Ambraseys (1988), the earthquake broke part of the NAF between Erzincan and Yedisu, the length of the seismic gap has to be shorter. Ambraseys reports 25 cm of right-lateral surface slip over a 4-km-long and N118°E trending rupture which, according to Barka and Wesnousky (unpublished manuscript), is located about 30 km to the western termination of the 1949 Karlıova earthquake. However, it is very likely that the earthquake did not took place in the middle of the Yedisu fault but, as shown in Figure 5.1, probably ruptured 20-30 km-long section of the fault westward from the end of the 1949 earthquake rupture. Otherwise, a very short seismic gap would have been present today between the 1967 and 1949 earthquakes. It would have been very difficult to find any physical basis for such a short gap because the eastern end of the fault had been accumulating elastic strain since 1784 and received significant amount of static stress from the neighbouring 1949 earthquake. Therefore, we conclude that the length of the Yedisu seismic gap is about 50 km which is 20 km less than previously thought, in which case, the magnitude of the expected in the Yedisu seismic gap gets lower to (Mw) 7.06 from 7.23 which will correspond to a 1.5 times weaker ground shaking. An earthquake of this size in the region will give rise to severe damage especially to populated cities like Erzurum, Erzincan and Bingöl as well as the coastal cities of Turkey next to the Black Sea due to the poor building quality.

Chapter 6

Conclusions

In this thesis we have used the Synthetic Aperture Radar Interferometry technique to map the crustal deformation as a result of both sudden (coseismic) and slow (interseismic or aseismic creep) motions along active faults in the Alp-Himalayan belt from Tell-Atlas Mountains (Morocco) in the west to the Zagros Mountains (Iran) in the east. Using freely available software packages, we have processed the InSAR data acquired by European Space Agency's ERS1, ERS2 and Envisat satellites for 11 medium-to-large sized (M>6) earthquakes (Table 1.1). For some cases, like the 2000-2002 Afyon-Akşehir (Sultandağı), the 2003 Pülümür (Tunceli) and the 2003 Bingöl earthquakes, InSAR did not provide any information useful for determining the characteristics of the earthquake ruptures. In other cases, we were able to obtain little but valuable information about the earthquakes. For example, for the 2005 İzmir-Sığacık earthquake, we detected a small amount of uplift (up to 4 fringes, i.e., 113 mm) along northern shore of the Sığacık Bay even though the earthquake occurred offshore. The area of surface uplift marked by the coseismic fringes in the interferograms is just a small fraction of a much larger region of crustal deformation under the sea bottom. As a result, we were not be able to determine the source parameters of the earthquakes by elastic dislocation modelling. Nevertheless, the interferograms helped us to solve the ambiguity whether the first event took place on the NW-SE trending left-lateral fault plane or on the NE-SW trending right-lateral fault plane. In some other cases, like 2003 Bam and 2005 Zarand earthquakes of Iran, the coseismic surface deformation was successfully determined and mapped by InSAR. Unfortunately, lack of field data and communication problems with Iranian scientists for scientific collaboration discouraged us to continue much further and study these earthquakes in detail. Therefore, much effort was given to the other cases in Turkey and Morocco where collaboration with local scientists were available and ongoing active tectonic processes are well known. These are the 1994-2004 Al Hoceima (Morocco) and the 2000 Orta (Çankırı) earthquakes, and the subtle changes due to aseismic surface creep along the İsmetpaşa segment of the North Anatolian Fault.

Using elastic dislocations on rectangular fault surfaces with a nonlinear minimization procedure based on simulating annealing algorithm, we modelled the coseismic surface displacement field due to Mw 6.0, Orta (Çankırı) earthquake of June 6, 2000 and deduce its source parameters (Fig. 2.1). Modeling results indicate that the earthquake was associated with a shallow (< 6 km) left-lateral oblique normal displacement that occurred on a north-south striking, eastward dipping, listric fault trending at a high angle to the plate boundary, right-lateral strike-slip North Anatolian fault. Careful analyses of multiple interferograms together with the field observations allowed us to infer the rupture geometry in fine detail. Modeling shows also that the coseismic slip occurs nearly only on the lower portion of the listric fault at depths of 4 to 6 km, but partially reaches to the surface along the surface trace of the Dodurga fault, in agreement with the field observations (Emre *et al.*, 2000). We suggest that the Dodurga fault is a result of a restraining bend along the North Anatolian fault since its left-lateral kinematics is consistent with the stress regime that favors the right-lateral North Anatolian fault.

Other earthquakes we studied in this work are the May 26, 1994 (Mw 6.0) and the February 24, 2004 (Mw 6.4) events that affected the Al Hoceima region of northern Morocco (Fig. 3.2). These events are the two strongest earthquakes recorded in this region. Yet, the exact location, kinematics and relationships between these earthquakes were not known prior to this study since neither of them produced surface ruptures. Using InSAR again we mapped the surface displacement field of the two earthquakes to characterize their seismic source parameters. Analysis of the interferograms constructed from two different viewing angles (i.e. from ascending and descending orbits) for both earthquakes and subsequent elastic modelling using slip inversions on triangular fault patches suggest that the two mainshocks occurred on blind conjugate strike-slip faults; the 1994 earthquake being associated with N23°E trending left-lateral fault and the 2004 earthquake with N45°W trending right-lateral fault. This result contradicts previous inferences on the kinematics, location and rupture geometry of the earthquakes deduced from conventional analyses of seismic waveforms and aftershocks distribution. This study reveals the fragmentation of the Rif Mountain throughout a complex network of conjugate blind faults consistent with the transpression tectonics along the plate boundary in North Africa. Although the two earthquakes took place in the Rif thrust-and-fold belt, the late Quaternary deformation indicates E-W extension in agreement with the NW-SE and NE-SW trending conjugate strike-slip faulting.

Taking advantage of the spatial and temporal coverage of the ERS1 and ERS2 satellites since 1992, we investigated the interseismic surface creep at İsmetpaşa, first spotted by Ambraseys 30 years ago on a brick wall built on the North Anatolian Fault (Ambraseys, 1970; Figures 4.1 and 4.2). Our study reveals the extent of the creep for the first time: the creeping starts at the western termination of the 1943 earthquake rupture and continue about 70 km to the west overlapping with the eastern end of the 1944 rupture (Fig. 4.3). The creep rate reaches its peak value of 11±3 mm/year at about the middle of the creeping section and is about 8±3 mm/year near İsmetpaşa where the brick wall is located, in agreement with the previous measurements (Fig. 4.6). A combined modelling of InSAR data with GPS suggests that the creep occurs most probably at the uppermost part (0-7km) of the seismogenic crust. The exponential decrease rate of creep in time postulates that the aseismic movement started following the 1944 Bolu-Gerede earthquake.

This study shows once again that InSAR is an extremely useful and powerful tool in studying crustal deformation due to earthquakes and aseismic surface or deep fault creep as a result of plate motions. We show here that this is especially the case for medium size earthquakes that do not produce clear surface ruptures. This work also demonstrates that without InSAR analysis, even the mechanism of faulting may not be confidently determined if active faults in the earthquake area are not well known and aftershocks are not precisely located (e.g. the case of 2004 Al Hoceima event). However, this report also illustrates that in the absence of field observations, additional measurement or multiple interferograms that capture the surface deformation from different directions, SAR interferometry alone may not be sufficient enough to constrain earthquake rupture geometry if there is no clear surface faulting.

The second method we use here in this study is the Coulomb Failure Criterion. We make use of this method in order to assess the static stress transfer and fault interactions around the Karlıova Triple Junction, and the overall stress change on the Yedisu seismic gap in eastern Turkey since the 1866 Bingöl earthquake. Our modelling reveals that out of 10 earthquakes, 6 can be explained with Coulomb stress triggering. This method however fails to explain the 2003 Bingöl, the first Varto event of 1966, and the smaller seismic activity around Karlıova in 2005. The effect of time dependent processes like viscoelastic relaxation may provide a plausible explanation to these events. We deduced that during the last 141 years the stress change due to the neighbouring earthquakes is about 2 bars in the center and reaches to 5 bars on the eastern edge of the Yedisu seismic gap. The size of the future event on this gap depends naturally on its length; the longer the gap the larger the earthquake. Our reasoning based on Coulomb stress calculations suggests that the total length of the Yedisu seismic gap might be significantly shorter than previously thought if the 1967 Pülümür-Kiğı event broke part of the Yedisu fault segment as suggested by Ambraseys (1988). If indeed the event took place on the Yedisu fault it must have broken its easternmost section, not the middle part, of the Yedisu fault thereby decreasing the length of the seismic gap down to 50 km. Fault scaling laws based on statistical observations (Wells and Coppersmith, 1994) suggest that a fault rupture of this size will lead to an earthquake of moment magnitude 7.06. If on the other hand, the 1967 Pülümür event took place on a different fault, then the length of the seismic gap will be around 70, and even 80 km (Serdar Akyüz, personal communication), in which case the size of the earthquake will increase to 7.23 or 7.29, leading to a 1.5 or 1.7 times more stronger ground shaking.

References

Ait-Brahim, L., Nakhcha, C., Tadili, B., Mrabet, A. E. and N. Jabour, 2004. Structural analysis and interpretation of the surface deformations of the February 24th, 2004 Al Hoceima earthquake, *EMSC-Newsletter*, 10-12.

Aki, K. and Richards, P. G., 1980. *Quantitative Seismology: Theory and Methods*, WH Freeman, San Francisco.

Akoğlu, A. M., 2001. 17 Ağustos 1999 İzmit Depremi Postsismik Deformasyonlarının Sentetik Açıklık Radar İnterferometrisi Yöntemi ile İncelenmesi, *Yüksek Lisans Tezi*, İ.T.Ü. Avrasya Yer Bilimleri Enstitüsü, İstanbul

Akoğlu, A. M. and Çakır, Z., 2007. Yüzey kırığı oluşturmayan depremlerin yorumlanması: Mw 6.0, 6 Haziran 2000 Orta, Çankırı, depreminden çıkarılacak dersler, Aktif Tektonik Araştırma Grubu 11. Toplantısı (ATAG11), Tübitak MAM, Gebze, November 8-9

Akoğlu, A. M., Çakır, Z., Meghraoui, M., Belabbes, S., El Alami, S. O., Ergintav, S. and Akyuz, H. S., 2006. The 1994-2004 Al Hoceima (Morocco) earthquake sequence: Conjugate fault ruptures deduced from InSAR, *Earth and Planetary Science Letters*, **252**, 467-480.

Aktar, M., Karabulut, H., Özalaybey, S. and Childs, D., 2007. A conjugate strike-slip fault system within the extensional tectonics of Western Turkey, *Geophysical Journal International*, **171**, 1363-1375.

Akyüz, S., 2008. Personal Communication

Akyüz, S., Uçarkuş, G., Şatır, D., Dikbaş, A. and Kozacı, Ö., 2006. 3 Şubat 2002 Çay depreminde meydana gelen yüzey kırığı üzerinde paleosismolojik araştırmalar, *Yerbilimleri*, **27**, 41-52.

Allen, C. R., Wyss, M., Brune, J. N., Grantz, A. and Wallace, R. E., 1972. Displacements on the Imperial, Superstition Hills, and San Andreas faults triggered by the Borrego Mountain earthquake, *U. S. Geological Survey Professional Paper*, **87**, 87-104.

Ambraseys, N. N., 1970. Some Characteristic Features of the Anatolian Fault Zone, *Tectonophysics*, **9**, 143-165.

Ambraseys, N. N., 1988. Engineering seismology, *Earthquake engineering & structural dynamics*, **17**, 1-105.

Ambraseys, N. N., 1997. The little-known earthquakes of 1866 and 1916 in Anatolia (Turkey), *Journal of Seismology*, **1**, 289-299.

Ambraseys, N. N. and Finkel, C., 1995. *The Seismicity of Turkey and Adjacent Areas: A Historical Review, 1500-1800*, Eren, Beyoğlu, İstanbul.

Ambraseys, N. N. and Jackson, J. A., 1998. Faulting associated with historical and recent earthquakes in the Eastern Mediterranean region, *Geophysical Journal International*, **133**, 390-406.

Ambraseys, N. N. and Zatopek, A., 1968. The Varto Üstükran (Anatolia) earthquake of 19 August 1966 summary of a field report, *Bulletin of the Seismological Society of America*, **58**, 47-102.

Amelung, F. and Bell, J. W., 2003. Interferometric synthetic aperture radar observations of the 1994 Double Spring Flat, Nevada, earthquake (M 5.9): Main shock accompanied by triggered slip on a conjugate fault, *Journal of Geophysical Research*, **108**, 2433, doi:2410.1029/2002JB001953.

Amelung, F. and King, G., 1997. Earthquake scaling laws for creeping and non-creeping faults, *Geophysical Research Letters*, **24**, 507-510.

Anderson, E. M., 1951. *The dynamics of faulting and dyke formation with applications to Britain*, Oliver and Boyd, Edinburgh.

Armijo, R., Meyer, B., Hubert, A. and Barka, A., 1999. Westward propagation of the North Anatolian fault into the northern Aegean: timing and kinematics, *Geology*, **27**, 267-270.

Armijo, R., Meyer, B., Navarro, S., King, G. and Barka, A., 2002. Asymmetric slip partitioning in the Sea of Marmara pull-apart: a clue to propagation processes of the North Anatolian Fault?, *Terra Nova*, **14**, 80.

Aytun, A., 1982. Creep measurements in the Ismetpasa region of the North Anatolian Fault zone, *Multidisciplinary Approach to Earthquake Prediction: Proceedings of the International Symposium on Earthquake Prediction in the North Anatolian Fault*, Braunschweig/Wiesbaden, 279-292.

Bamler, R., 2000. Principles of synthetic aperture radar, *Surveys in Geophysics*, **21**, 147-157.

Barka, A., 1996. Slip distribution along the North Anatolian fault associated with the large earthquakes of the period 1939 to 1967, *Bulletin of the Seismological Society of America*, **86**, 1238-1254.

Barka, A., 1999. The 17 August 1999 Izmit Earthquake, *Science*, **285**, 1858-1859.

Barka, A. A., Reilinger, R., Şaroglu, F. and Şengör, A. M. C., 1995. The Isparta Angle: its importance in the neotectonics of the Eastern Mediterranean Region, *Proceedings of International Earth Science Colloquium on the Aegean Region*, İzmir, Turkey, 9-14 October, 3–18.

Beauducel, F., Briole, P. and Froger, J.-L., 2000. Volcano wide fringes in ERS synthetic aperture radar interferograms of Etna, *Journal of Geophysical Research*, **105**, 16391-16402.

Bekler, F. N., Kekovalı, K., Kalafat, D. and Pınar, A., 2003. January 27, 2003 Pülümür (Turkey) Earthquake, Kandilli Observatory and Earthquake Research Institute – Seismology Division, İstanbul.

Ben-Zion, Y., Rice, J. R. and Dmowska, R., 1993. Interaction of the San Andreas fault creeping segment with adjacent great rupture zones and earthquake recurrence at Parkfield, *J. Geophys. Res*, **98**, 2135–2144.

Benetatos, C., Kiratzi, A., Ganas, A., Ziazia, M., Plessa, A. and Drakatos, G., 2006. Strike-slip motions in the Gulf of Sigacik (western Turkey): properties of the 17 October 2005 earthquake seismic sequence, *Tectonophysics*, **426**, 263-279.

Bernard, P., Briole, P., Meyer, B., Caen, H. L., Gomez-Gonzalez, J.-M., Tiberi, C., Cattin, R., Hatzfeld, D., Lachet, C., Lebrun, B., Deschamps, A., Courboulex, F., Larroque, C., Rigo, A., Massonnet, D., Papadimitriou, P., Kassaras, J., Diagourtas, D., Makropoulos, K. and Veis, G., 1997. The Ms=6.2, June 15, 1995 Aigion earthquake (Greece): Evidence for low normal faulting in the Corinth rift, *Journal of Seismology*, **1**, 131-150.

Bezzeghoud, M. and Buforn, E., 1999. Source parameters of the 1992 Melilla (Spain, Mw=4.8), 1994 Al Hoceima (Morocco, Mw=5.8), and 1994 Mascara (Algeria, M-w=5.7) earthquakes and seismotectonic implications, *Bulletin of the Seismological Society of America*, **89**, 359-372.

Bilham, R., Suszek, N. and Pinkney, S., 2004. California creepmeters, *Seismological Research Letters*, **75**, 481-492.

Bodin, P., Bilham, R., Behr, J., Gomberg, J. and Hudnut, K. W., 1994. Slip triggered on southern California faults by the 1992 Joshua Tree, Landers, and

Big Bear earthquakes, *Bulletin of the Seismological Society of America*, **84**, 806-816.

Bokelmann, G. H. R. and Kovach, R. L., 2003. Long-term creep-rate changes and their causes, *Geophys. Res. Lett*, **30**, 1445.

Boray, A., Şaroğlu, F. and Emre, Ö., 1985. Isparta Büklümünün kuzey kesiminde Doğu-Batı daralma için bazı veriler, *Jeoloji Mühendisliği*, 9-20.

Bozkurt, E., 2001. Neotectonics of Turkey; a synthesis, *Geodinamica Acta*, **14**, 3-30.

Brahim, L. A., Tadili, B., Nakhcha, C., Mouayn, I., Ramdani, M., Limouri, M., El Qadi, A., Alaoui, F. S. and Benhalima, M., 2004. Using active faults and seismicity for the strong motion modeling in the eastern Rif (northern Morocco), *Pure and Applied Geophysics,* **161**, 1081-1091.

Buforn, E., Bezzeghoud, M., Fresno, C. d., Borges, J. F., Madariaga, R. and Udías, A., 2005. Study of the fracture process of Al Hoceima earthquake (24/02/2004, Mw= 6.2) from regional and teleseismic data, *Geophysical Research Abstracts*, **7**, 05301.

Buforn, E., Bezzeghoud, M., Udias, A. and Pro, C., 2004. Seismic sources on the Iberia-African plate boundary and their tectonic implications, *Pure and Applied Geophysics*, **161**, 623-646.

Burford, R. O. and Harsh, P. W., 1980. Slip on the San-Andreas-Fault in Central California from Alignment Array Surveys, *Bulletin of the Seismological Society of America*, **70**, 1233-1261.

Bürgmann, R., Ayhan, M. E., Fielding, E. J., Wright, T. J., McClusky, S., Aktug, B., Demir, C., Lenk, O. and Turkezer, A., 2002. Deformation during the 12 November 1999 Duzce, Turkey, earthquake, from GPS and InSAR data, *Bulletin of the Seismological Society of America*, **92**, 161-171.

Bürgmann, R., Fielding, E. and Sukhatme, J., 1998. Slip along the Hayward fault, California, estimated from space-based synthetic aperture radar interferometry, *Geology,* **26**, 559-562.

Bürgmann, R., Rosen, P. A. and Fielding, E. J., 2000. Synthetic Aperture Radar interferometry to measure Earth's surface topography and its deformation, *Annual Review of Earth and Planetary Sciences*, **28**, 169-209.

Bürgmann, R., Schmidt, D., Nadeau, R. M., d'Alessio, M., Fielding, E., Manaker, D., McEvilly, T. V. and Murray, M. H., 2000. Earthquake potential along the northern Hayward fault, California, *Science*, **289**, 1178-1182.

Byerlee, J., 1978. Friction of rocks, *Pure and Applied Geophysics,* **116**, 615-626.

Calvert, A., Gomez, F., Seber, D., Barazangi, M., Jabour, N., Ibenbrahim, A. and Demnati, A., 1997. An integrated geophysical investigation of recent seismicity in the Al-Hoceima region of north Morocco, *Bulletin of the Seismological Society of America*, **87**, 637-651.

Comninou, M. A. and Dunders, J., 1975. The angular dislocation in a half space, *J. Elasticity*, **5**, 203-216.

Çakır, Z., 2003. Analysis of the crustal deformation caused by the 1999 İzmit and Düzce earthquakes using synthetic aperture radar interferometry, *PhD Thesis*, ITU Geological Engineering, Istanbul, Turkey.

Çakır, Z., Akoglu, A. M., Belabbes, S., Ergintav, S. and Meghraoui, M., 2005. Creeping along the Ismetpasa section of the North Anatolian fault (Western Turkey): Rate and extent from InSAR, *Earth and Planetary Science Letters,* **238**, 225-234.

Çakır, Z., Barka, A. A., Chabalier, J. B. d., Armijo, R. and Meyer, B., 2003. Kinematics of the November 12, 1999 (Mw=7.2) Düzce earthquake deduced from SAR interferometry, *Turkish Journal of Earth Sciences*, **12**, 105-118.

Çakır, Z., de Chabalier, J. B., Armijo, R., Meyer, B., Barka, A. and Peltzer, G., 2003. Coseismic and early post-seismic slip associated with the 1999 Izmit earthquake (Turkey), from SAR interferometry and tectonic field observations, *Geophysical Journal International*, **155**, 93-110.

Çakır, Z., Meghraoui, M., Akoglu, A. M., Jabour, N., Belabbes, S. and Ait-Brahim, L., 2006. Surface deformation associated with the M-w 6.4, 24 February 2004 Al Hoceima, Morocco, earthquake deduced from InSAR: Implications for the active tectonics along North Africa, *Bulletin of the Seismological Society of America*, **96**, 59-68.

Das, S. and Scholz, C. H., 1981. Off-fault aftershock clusters caused by shear-stress increase, *Bulletin of the Seismological Society of America*, **71**, 1669-1675.

Delacourt, C., Briole, P. and Achache, J., 1998. Tropospheric corrections of SAR interferograms with strong topography. Application to Etna, *Geophysical Research Letters*, **25**, 2849-2852.

DeMets, C., Gordon, R. G., Argus, D. F. and Stein, S., 1990. Current plate motions, *Geophysical Journal International*, **101**, 425-478.

Deniz, R., Aksoy, A., Yalin, D., Seeger, H., Franke, P., Hirsch, O. and Bautsch, P., 1993. Determination of crustal movements in Turkey by terrestrial geodetic methods, *Journal of Geodynamics*, **18**, 13-22.

Doğan, A., Kondo, H., Emre, Ö., Awata, Y., Özalp, S., Tokay, F. and Yıldırım, C., 2002. Stable creeping and distant triggered slips by the 1999 Izmit Earthquake along the Ismetpasa section, North Anatolian Fault Zone, Turkey, *EOS Trans. AGU Fall Meeting, Supplement*, **83**, S11B-1156.

Donnellan, A. and Lyzenga, G. A., 1998. GPS observations of fault afterslip and upper crustal deformation following the Northridge earthquake, *Journal of Geophysical Research-Solid Earth*, **103**, 21285-21297.

Dorbath, L., Hahou, Y., Delouis, B., Dorbath, C., Woerd, J. V. D., Badrane, S., Frogneux, M., Haessler, H., Jacques, E., Menzhi, M. and Tapponnier, P., 2005. Études sismologiques sur le séisme D'al Hoceima: Localisation, et mécanisme du choc principal et des répliques, contraintes et structure de la zone epicentrale, *Colloque Intenational Seisme d'Al Hoceima: bilan et perspectives*, Al Hoceima, Morocco, 24-26 February 2005.

El Alami, S. O., Tadili, B., Cherkaoui, T. E., Medina, F., Ramdani, M., Ait-Brahim, L. and Harnafi, M., 1998. The Al Hoceima earthquake of May 26, 1994 and its aftershocks: a seismotectonic study, *Annali di Geofisica*, **41**, 519-537.

Emre, Ö., Duman, T. Y., Doğan, A. and Özalp, S., 2000. 6 Haziran Orta Çankırı Depremi Değerlendirme Raporu, MTA, **10323,** Ankara.

Emre, Ö., Duman, T. Y., Doğan, A., Özalp, S., Tokay, F. and Kuşçu, İ., 2003. Surface faulting associated with the Sultandağı earthquake (Mw 6.5) of 3 February 2002, southwestern Turkey, *Seismological Research Letters*, **74**, 382-392.

Eyidoğan, H., Utku, Z., Güçlü, U. and Değirmenci, E., 1991. *Türkiye Büyük Depremleri Makro-sismik Rehberi (1900-1988)*, İstanbul Teknik Üniversitesi Maden Fakültesi Jeofizik Mühendisliği Bölümü, İstanbul.

Farr, T. G., 2004. Personal Communication

Farr, T. G., Rosen, P. A., Caro, E., Crippen, R., Duren, R., Hensley, S., Kobrick, M., Paller, M., Rodriguez, E., Roth, L., Seal, D., Shaffer, S., Shimada, J., Umland, J., Werner, M., Oskin, M., Burbank, D. and Alsdorf, D., 2007. The shuttle radar topography mission, *Reviews of Geophysics*, **45**.

Fialko, Y., Sandwell, D., Simons, M. and Rosen, P., 2005. Three-dimensional deformation caused by the Bam, Iran, earthquake and the origin of shallow slip deficit, *Nature*, **435**, 295-299.

Flerit, F., Armijo, R., King, G. C. P., Meyer, B. and Barka, A., 2003. Slip partitioning in the Sea of Marmara pull-apart determined from GPS velocity vectors, *Geophysical Journal International*, **154**, 1-7.

Freed, A. M., Ali, S. T. and Bürgmann, R., 2007. Evolution of stress in Southern California for the past 200 years from coseismic, postseismic and interseismic stress changes, *Geophysical Journal International*, **169**, 1164-1179.

Frizon de Lamotte, D., 1987. Un exemple de collage synmétamorphe: la déformation miocène des Temsamane (Rif externe, Maroc), *Bulletin de la Société géologique de France*, **3**, 337-344.

Fuenzalida, H., Dorbath, L., Cisternas, A., Eyidoğan, H., Barka, A., Rivera, L., Haessler, H., Philip, H., Lyberis, N., 1997. Mechanism of the 1992 Erzincan earthquake and its aftershocks, tectonics of the Erzincan Basin and decoupling on the North Anatolian Fault, *Geophysical Journal International*, **129**, 1-28.

Funning, G. J., Parsons, B., Wright, T. J., Jackson, J. A. and Fielding, E. J., 2005. Surface displacements and source parameters of the 2003 Bam (Iran) earthquake from Envisat advanced synthetic aperture radar imagery, *J. Geophys. Res*, **110**.

Gabriel, A. K., Goldstein, R. M. and Zebker, H. A., 1989. Mapping small elevation changes over large areas: differential radar interferometry, *Journal of Geophysical Research*, **94**, 9183-9191.

Goldstein, R. M. and Werner, C. L., 1998. Radar interferogram filtering for geophysical applications, *Geophysical Research Letters*, **25**, 4035-4038.

Graham, L. C., 1974. Synthetic interferometer radar for topographic mapping, *Proceedings of the IEEE*, **62**, 763-768.

Grimison, N. L. and Chen, W. P., 1986. The Azores-Gibraltar plate boundary - focal mechanisms, depths of earthquakes, and their tectonic implications, *Journal of Geophysical Research-Solid Earth and Planets*, **91**, 2029-2047.

Hanssen, R. F., 2001. *Radar Interferometry: Data Interpretation and Error Analysis*, Kluwer Academic Publishers, Dordrecht.

Harris, R. A., 1998. Introduction to special section: Stress triggers, stress shadows, and implications for seismic hazard, *Journal of Geophysical Research-Solid Earth*, **103**, 24347-24358.

Hatzfeld, D., Caillot, V., Cherkaoui, T. E., Jebli, H. and Medina, F., 1993. Microearthquake seismicity and fault plane solutions around the Nekor strike-slip-fault, Morocco, *Earth and Planetary Science Letters*, **120**, 31-41.

Hubert-Ferrari, A., Armijo, R., King, G., Meyer, B. and Barka, A., 2002. Morphology, displacement, and slip rates along the North Anatolian Fault, Turkey, *Journal of Geophysical Research-Solid Earth*, **107**.

Hubert-Ferrari, A., Barka, A., Jacques, E., Nalbant, S. S., Meyer, B., Armijo, R., Tapponnier, P. and King, G. C. P., 2000. Seismic hazard in the Marmara Sea region following the 17 August 1999 Izmit earthquake, *Nature*, **404**, 269-273.

Jabour, N., Kasmi, M., Menzhi, M., A.Birouk, Hni, L., Hahou, Y., Timoulali, Y. and Badrane, S., 2004. The February 24th, 2004 Al Hoceima earthquake, *Eur.-Mediter. Seismol. Cent. Newsletter*, 7-10.

Jackson, J. A., Gagnepain, J., Houseman, G., King, G. C. P., Papadimitriou, P., Soufleris, C. and Virieux, J., 1982. Seismicity, normal faulting, and the geomorphological development of the Gulf of Corinth (Greece) - the Corinth earthquakes of February and March 1981, *Earth and Planetary Science Letters*, **57**, 377-397.

Johanson, I. A. and Burgmann, R., 2005. Creep and quakes on the northern transition zone of the San Andreas fault from GPS and InSAR data, *Geophysical Research Letters*, **32**.

Jònsson, S., Zebker, H., Segall, P. and Amelung, F., 2002. Fault slip distribution of the 1999 Hector Mine, California, earthquake, estimated from satellite radar and GPS measurements, *Bulletin of the Seismological Society of America*, **92**, 1377-1389.

Kampes, B. M., Hanssen, R. F. and Perski, Z., 2003. Radar Interferometry with Public Domain Tools, *Third International Workshop on ERS SAR Interferometry, `FRINGE03'*, Frascati, Italy, 1-5 Dec 2003, 6 pp.

Ketin, I., 1948. Ueber die tektonisch-mechanischen Folgerungen aus den grossen anatolischen Erdbeben des letzten Dezenniums, *Geologische Rundschau*, **36**, 77-83.

King, G. C. P., Stein, R. S. and Lin, J., 1994. Static stress changes and the triggering of earthquakes, *Bulletin of the Seismological Society of America*, **84**, 935-953.

Koçyiğit, A. and Özacar, A., 2003. Extensional neotectonic regime through the NE edge of the outer Isparta angle, SW Turkey: new field and seismic data, *Turkish Journal of Earth Sciences*, **12**, 67-90.

Koçyiğit, A., Rojay, B., Cühan, B. and Özacar, A., 2001. The June 6, 2000, Orta (Çankırı, Turkey) earthquake: sourced from a new antithetic sinistral strike-slip structure of the North Anatolian Fault system, the Dodurga Fault Zone, *Turkish Journal of Earth Sciences*, **10**, 69-82.

Kozacı, Ö., Dolan, J., Finkel, R. and Hartleb, R., 2007. Late Holocene slip rate for the North Anatolian fault, Turkey, from cosmogenic Cl-36 geochronology: Implications for the constancy of fault loading and strain release rates, *Geology*, **35**, 867-870.

Lienkaemper, J. J., Galehouse, J. S. and Simpson, R. W., 1997. Creep response of the Hayward fault to stress changes caused by the Loma Prieta earthquake, *Science*, **276**, 2014.

Lienkaemper, J. J. and Williams, P. L., 1999. Evidence for surface rupture in 1868 on the Hayward fault in north Oakland and major rupturing in prehistoric earthquakes, *Geophysical Research Letters*, **26**, 1949-1952.

Lin, J. and Stein, R. S., 2004. Stress triggering in thrust and subduction earthquakes and stress interaction between the southern San Andreas and nearby thrust and strike-slip faults, *J. Geophys. Res*, **109**, B02303.

Love, A., 1985. In memory of Carl A. Wiley, *Antennas and Propagation Society Newsletter, IEEE*, **27**, 17-18.

Lyons, S. and Sandwell, D., 2002. Fault creep along the southern San Andreas from InSAR, permanent scatterers, and stacking, *Journal of Geophysical Research*, **108**, 24 pp.

MacDonald, H. C., 1969. Geologic Evaluation of Radar Imagery from Eastern Panama and Northwestern Colombia, *Ph.D. Dissertation*, Kansas

Maerten, F., Resor, P., Pollard, D. and Maerten, L., 2005. Inverting for slip on three-dimensional fault surfaces using angular dislocations, *Bulletin of the Seismological Society of America*, **95**, 1654-1665.

Malservisi, R., Gans, C. and Furlong, K. P., 2003. Numerical modeling of strike-slip creeping faults and implications for the Hayward fault, California, *Tectonophysics*, **361**, 121-137.

Massonnet, D. and Feigl, K. L., 1998. Radar interferometry and its application to changes in the Earth's surface, *Reviews of Geophysics*, **36**, 441-500.

Massonnet, D., Rossi, M., Carmona, C., Adagna, F., Peltzer, G., Feigl, K. and Rabaute, T., 1993. The displacement field of the Landers earthquake mapped by radar interferometry, *Nature*, **364**, 138-142.

McClusky, S., Balassanian, S., Barka, A., Demir, C., Ergintav, S., Georgiev, I., Gurkan, O., Hamburger, M., Hurst, K., Kahle, H., Kastens, K., Kekelidze, G., King, R., Kotzev, V., Lenk, O., Mahmoud, S., Mishin, A., Nadariya, M., Ouzounis, A., Paradissis, D., Peter, Y., Prilepin, M., Reilinger, R., Sanli, I., Seeger, H., Tealeb, A., Toksoz, M. N. and Veis, G., 2000. Global Positioning System constraints on plate kinematics and dynamics in the eastern Mediterranean and Caucasus, *Journal of Geophysical Research-Solid Earth*, **105**, 5695-5719.

McClusky, S., Reilinger, R., Mahmoud, S., Ben Sari, D. and Tealeb, A., 2003. GPS constraints on Africa (Nubia) and Arabia plate motions, *Geophysical Journal International*, **155**, 126-138.

McKenzie, D., 1972. Active Tectonic of the Mediterranean Region, *The Geophysical Journal of the Royal Astronomical Society*, **30**, 109-185.

Medina, F., 1995. Present-day state of stress in northern Morocco from focal mechanism analysis, *Journal of Structural Geology*, **17**, 1035-1046.

Meghraoui, M., Morel, J. L., Andrieux, J. and Dahmani, M., 1996. Tectonique plio-quaternaire de la chaine tello-rifaine et de la mer d'Alboran; une zone complexe de convergence continent-continent, *Bulletin de la Société géologique de France*, **167**, 141-157.

Milkereit, C., Grosser, H., Wang, R., Wetzel, H. U., Woith, H., Karakisa, S., Zunbul, S. and Zschau, J., 2004. Implications of the 2003 Bingöl earthquake for the interaction between the North and East Anatolian faults, *Bulletin of the Seismological Society of America*, **94**, 2400-2406.

Morel, J. L. and Meghraoui, M., 1996. Goringe-Alboran-Tell tectonic zone: A transpression system along the Africa-Eurasia plate boundary, *Geology*, **24**, 755-758.

Nadeau, R. M. and McEvilly, T. V., 1999. Fault slip rates at depth from recurrence intervals of repeating microearthquakes, *Science*, **285**, 718.

Nalbant, S. S., 1996. Depremlerin oluşturduğu deformasyon ve gerilme alanlarının modellenmesi, *Doktora Tezi*, Jeofizik Mühendisliği Yer Fiziği Programı, İstanbul

Nalbant, S. S., McCloskey, J. and Steacy, S., 2005. Lessons on the calculation of static stress loading from the 2003 Bingol, Turkey earthquake, *Earth and Planetary Science Letters*, **235**, 632-640.

Nalbant, S. S., McCloskey, J., Steacy, S. and Barka, A. A., 2002. Stress accumulation and increased seismic risk in eastern Turkey, *Earth and Planetary Science Letters*, **195**, 291-298.

Nocquet, J. M. and Calais, E., 2004. Geodetic measurements of crustal deformation in the western Mediterranean and Europe, *Pure and Applied Geophysics*, **161**, 661-681.

Okada, Y., 1985. Surface deformation due to shear and tensile faults in a half-space, *Bulletin of the Seismological Society of America*, **75**, 1135-1154.

Okada, Y., 1992. Internal deformation due to shear and tensile faults in a half-space, *Bulletin of the Seismological Society of America*, **82**, 1018-1040.

Onn, F., 2006. Modeling water vapor using GPS with application to mitigating InSAR atmospheric distortions, *PhD Thesis*, Electrical Engineering, Stanford, CA

Özalaybey, S., Ergin, M., Aktar, M., Tapırdamaz, C., Biçmen, F. and Yörük, A., 2002. The 1999 Izmit Earthquake Sequence in Turkey: Seismological and Tectonic Aspects, *Bulletin of the Seismological Society of America*, **92**, 376-386.

Özalp, S., Doğan, A. and Emre, Ö., 2005. 6 Haziran 2005 Karlıova Depremi'nin Değerlendirilmesi, MTA, Ankara.

Parsons, T., Toda, S., Stein, R. S., Barka, A. and Dieterich, J. H., 2000. Heightened odds of large earthquakes near Istanbul: an interaction-based probability calculation, *Science*, **288**, 661-665.

Pinar, N., 1953. Etude géologique et macrosismique du tremblement de terre de Kursunlu (Anatolie septentrionale) du 13 aout 1951, *Rev. Fac. Sci. Univ. Istanbul, Series A*, **18**, 131-141.

Ramdani, M., Tadili, B. and Mrabet, T. E., 1989. The present state of knowledge on historical seismicity of Morocco, *Proceedings of the symposium on calibration of historical earthquakes in Europe and recent developments in intensity interpretation, European Seismological Commission*, Instituto Geográfico Nacional, Madrid, 257-279.

Reilinger, R., McClusky, S., Vernant, P., Lawrence, S., Ergintav, S., Cakmak, R., Ozener, H., Kadirov, F., Guliev, I., Stepanyan, R., Nadariya, M., Hahubia, G., Mahmoud, S., Sakr, K., ArRajehi, A., Paradissis, D., Al-Aydrus, A., Prilepin, M., Guseva, T., Evren, E., Dmitrotsa, A., Filikov, S. V., Gomez, F., Al-Ghazzi, R. and Karam, G., 2006. GPS constraints on continental deformation in the Africa-Arabia-Eurasia continental collision zone and implications for the dynamics of plate interactions, *Journal of Geophysical Research-Solid Earth*, **111**.

Resor, P. G., Pollard, D. D., Wright, T. J. and Beroza, G. C., 2005. Integrating high-precision aftershock locations and geodetic observations to model coseismic deformation associated with the 1995 Kozani-Grevena earthquake, Greece, *Journal of Geophysical Research-Solid Earth*, **110**.

Roeloffs, E. A., 2001. Creep rate changes at Parkfield, California 1966-1999: seasonal, precipitation induced, and tectonic, *Journal of Geophysical Research*, **106**, 16525-16547.

Rosen, P., Hensley, S., Joughin, I. R., Li, F. K., Madsen, S., Rodriguez, E. and Goldstein, R., 2000. Synthetic Aperture Radar Interferometry, *Proceedings of the IEEE*, **88**, 333-382.

Rosen, P., Werner, C., Fielding, E., Hensley, S., Buckley, S. and Vincent, P., 1998. Aseismic creep along the San Andreas fault northwest of Parkfield, CA measured by radar interferometry, *Geophysical Research Letters*, **25**, 825-828.

Rosen, P. A., Hensley, S., Peltzer, G. and Simons, M., 2004. Updated Repeat Orbit Interferometry package released, *Eos Trans. AGU*, **85**, 47.

Rubin, A. M., Gillard, D. and Got, J.-L., 1999. Streaks of microearthquakes along creeping faults, *Nature*, **400**, 635-641.

Savage, J. C. and Lisowski, M., 1993. Inferred depth of creep on the Hayward fault, central California, *J. Geophys. Res*, **98**, 787–793.

Scharroo, R. and Visser, P., 1998. Precise orbit determination and gravity field improvement for the ERS satellites, *Journal of Geophysical Research*, **103**, 8113-8127.

Schmidt, D. A., Burgmann, R., Nadeau, R. M. and d'Alessio, M., 2005. Distribution of aseismic slip rate on the Hayward fault inferred from seismic and geodetic data, *Journal of Geophysical Research-Solid Earth*, **110**.

Simpson, R. W., Lienkaemper, J. J. and Galehouse, J. S., 2001. Variations in creep rate along the Hayward Fault, California, interpreted as changes in depth of creep, *Geophys. Res. Lett*, **28**, 2269–2272.

Simpson, R. W. and Reasenberg, P. A., 1994. Earthquake-induced static stress changes on central California faults, *The Loma Prieta, California, earthquake of October 17, 1989-Tectonic processes and models*, U.S. Geological Survey Professional Paper 1550-F.

Steacy, S., Gomberg, J. and Cocco, M., 2005. Introduction to special section: Stress transfer, earthquake triggering, and time-dependent seismic hazard, *Journal of Geophysical Research-Solid Earth,* **110**.

Stein, R. S., Barka, A. A. and Dieterich, J. H., 1997. Progressive failure on the North Anatolian fault since 1939 by earthquake stress triggering, *Geophysical Journal International*, **128**, 594-604.

Stein, R. S. and Lisowski, M., 1983. The 1979 Homestead Valley earthquake sequence, California - control of aftershocks and postseismic deformation, *Journal of Geophysical Research,* **88**, 6477-6490.

Steinbrugge, K. V., Zacher, E. G., Tocher, D., Whitten, C. A. and Claire, C. N., 1960. Creep on the San Andreas fault, *Bulletin of the Seismological Society of America,* **50**, 389-415.

Stich, D., Mancilla, F. D., Baumont, D. and Morales, J., 2005. Source analysis of the Mw 6.3 2004 Al Hoceima earthquake (Morocco) using regional apparent source time functions, *Journal of Geophysical Research-Solid Earth,* **110**.

Şaroglu, F., Emre, Ö. and Boray, A., 1987. Türkiye'nin Diri Fayları ve Depremsellikleri, MTA Raporu, **8174,** Ankara, Türkiye.

Şaroğlu, F., Emre, Ö. and Kuşçu, İ., 1992. Active Fault Map of Turkey, General Directorate of Mineral Research and Exploration (MTA).

Şengör, A. M. C., Görür, N. and Şaroğlu, F., 1985. Strike-slip faulting and related basin formation in zones of tectonic escape: Turkey as a case study. In *Strike-slip Deformation, Basin Formation, and Sedimentation, Soc. Econ. Paleontol. Spec. Publ.*, pp. 227-264.

Şengör, A. M. C., Tüysüz, O., İmren, C., Sakınç, M., Eyidoğan, H., Gorur, N., Le Pichon, X. and Rangin, C., 2005. The North Anatolian Fault: a new look, *Annual Review of Earth and Planetary Sciences*, **33**, 37-112.

Talebian, M., Biggs, J., Bolourchi, M., Copley, A., Ghassemi, A., Ghorashi, M., Hollingsworth, J., Jackson, J., Nissen, E., Oveisi, B., Parsons, B., Priestley, K. and Saiidi, A., 2006. The Dahuiyeh (Zarand) earthquake of 2005 February 22 in central Iran: reactivation of an intramountain reverse fault, *Geophysical Journal International*, **164**, 137-148.

Talebian, M., Fielding, E. J., Funning, G. J., Ghorashi, M., Jackson, J., Nazari, H., Parsons, B., Priestley, K., Rosen, P. A., Walker, R. and Wright, T. J., 2004. The 2003 Bam (Iran) earthquake: Rupture of a blind strike-slip fault, *Geophysical Research Letters*, **31**, doi:10.1029/2004GL020058.

Taymaz, T., Wright, T. J., Yolsal, S., Tan, O., Fielding, E. and Seyitoğlu, G., 2007. Source characteristics of the 6 June 2000 Orta Çankırı (central Turkey) earthquake: a synthesis of seismological, geological and geodetic (InSAR) observations, and internal deformation of the Anatolian plate. In *The Geodynamics of the Aegean and Anatolia 1*, Geological Society London Special Publications, pp. 259-290.

Teyssier, C., Tikoff, B. and Markley, M., 1995. Oblique plate motion and continental tectonics, *Geology*, **23**, 447-450.

Thatcher, W., 1979. Systematic inversion of geodetic data in central California, *Journal of Geophysical Research*, **84**, 2283-2295.

Thomas, A. L., 1993. Poly3D : a three-dimensional, polygonal element, displacement discontinuity boundary element computer program with applications to fractures, faults, and cavities in the Earth's crust, *M.S. Thesis*, Stanford University. Dept. of Geology., Stanford, California

Toda, S., Stein, R. S., Richards-Dinger, K. and Bozkurt, S. B., 2005. Forecasting the evolution of seismicity in southern California: animations built on earthquake stress transfer, *Journal of Geophysical Research-Solid Earth*, **110**.

Toksoz, M. N., Shakal, A. F. and Michael, A. J., 1979. Space-time migration of earthquakes along the North-Anatolian fault zone and seismic gaps, *Pure and Applied Geophysics*, **117**, 1258-1270.

Turkelli, N., Sandvol, E., Zor, E., Gok, R., Bekler, T., Al-Lazki, A., Karabulut, H., Kuleli, S., Eken, T., Gurbuz, C., Bayraktutan, S., Seber, D. and Barazangi, M., 2003. Seismogenic zones in Eastern Turkey, *Geophysical Research Letters*, **30**.

Udias, A., Buforn, E. and de Gauna, J. R., 1989. *Catalogue of Focal Mechanisms of European Earthquakes*, Dept. de Geofísica, Universidad Complutense de Madrid, Madrid.

Utkucu, M., Alptekin, O. and Pinar, A., 2003. A detailed source study of the Orta (Cankiri) earthquake of June 6, 2000 (Ms=6.1): An intraplate earthquake in central Anatolia, *Journal of Seismology*, **7**, 193-202.

Wallace, R. E., 1968. Earthquake of August 19, 1966, Varto area, eastern Turkey, *Bulletin of the Seismological Society of America*, **58**, 11-45.

Wells, D. L. and Coppersmith, K. J., 1994. New empirical relationships among magnitude, rupture length, rupture width, rupture area, and surface displacement, *Bulletin of the Seismological Society of America*, **84**, 974-1002.

Westaway, R., 1999. The mechanical feasibility of low-angle normal faulting, *Tectonophysics*, **308**, 407-443.

Westaway, R. and Arger, J., 2001. Kinematics of the Malatya-Ovacık fault zone, *Geodinamica Acta*, **14**, 103-131.

Wiley, C. A., 1985. Synthetic Aperture Radars, *Aerospace and Electronic Systems, IEEE Transactions on*, **AES-21**, 440-443.

Wright, T., Parsons, B. and Fielding, E., 2001. Measurement of interseismic strain accumulation across the North Anatolian Fault by satellite radar interferometry, *Geophysical Research Letters*, **28**, 2117-2120.

Wright, T. J., Parsons, B. E. and Lu, Z., 2004. Towards mapping surface deformation in three dimensions using InSAR, *Geophysical Research Letters*, **31**, 5 pp.

Zebker, H. A., 2000. Studying the Earth with interferometric radar, *Computing in Science and Engineering*, **2**, 52-60.

Zisk, S. H., 1972. A new Earth-based radar technique for the measurement of Lunar topography, *Moon*, **4**, 296-306.

Curriculum Vitae

A. M. Akoğlu was born in Ankara in 1978. He obtained his Bachelor's degree from the Geophysical Engineering department of İTÜ in 1999. After getting his MSc degree in Geodynamics from the Eurasian Institute of Earth Sciences in 2001 he was accepted to the PhD program in the same institute.